MICROCOPY RESOLUTION TEST CHART

NATIONAL BUREAU OF STANDARDS-1963-A

AD A129313

FRACTURE MECHANICS OF

TRANSVERSE CRACKS AND EDGE DELAMINATION

IN GRAPHITE-EPOXY COMPOSITE LAMINATES

A.S.D. Wang
Drexel University, Phila. Pa. 19104

and

Frank W. Crossman
Lockheed Palo Alto Research Lab,
Palo Alto, Ca. 94304

Drexel University

College of Engineering
Department of
Mechanical Engineering
and Mechanics
Philadelphia, PA 19104

(215) 895-2352-52

DTIC
ELECTE
JUN 1 3 1983
A

83 06 10 074

FRACTURE MECHANICS OF

TRANSVERSE CRACKS AND EDGE DELAMINATION

IN GRAPHITE-EPOXY COMPOSITE LAMINATES

A.S.D. Wang
Drexel University, Phila. Pa. 19104

and

Frank W. Crossman
Lockheed Palo Alto Research Lab.
Palo Alto, Ca. 94304

March, 1982

Final Technical Report

AIR FORCE OFFICE OF SCIENTIFIC RESEARCH

DTIC
ELECTE
JUN 1 3 1983

A

REPORT DOCUMENTATION PAGE		READ INSTRUCTIONS BEFORE COMPLETING FORM
1. REPORT NUMBER AFOSR-TR- 83 - 0452	**2. GOVT ACCESSION NO.** AD-A129313	**3. RECIPIENT'S CATALOG NUMBER**
4. TITLE (and Subtitle) FRACTURE MECHANICS OF TRANSVERSE CRACKS AND EDGE DELAMINATION IN GRAPHITE-EPOXY COMPOSITE LAMINATES		**5. TYPE OF REPORT & PERIOD COVERED** Interim Report 1 Sep 79 - 30 Sep 81
		6. PERFORMING ORG. REPORT NUMBER
7. AUTHOR(s) A S D WANG and F W CROSSMAN		**8. CONTRACT OR GRANT NUMBER(s)** F49620-79-C-0206
9. PERFORMING ORGANIZATION NAME AND ADDRESS DREXEL UNIVERSITY, PHILA, PA 19104 AND LOCKHEED PALO ALTO RESEARCH LAB, PALO ALTO, CA		**10. PROGRAM ELEMENT, PROJECT, TASK AREA & WORK UNIT NUMBERS** 2307/B2 61102F
11. CONTROLLING OFFICE NAME AND ADDRESS AIR FORCE OFFICE OF SCIENTIFIC RESEARCH/NA BOLLING AFB, DC 20332		**12. REPORT DATE** March 1982
		13. NUMBER OF PAGES 160
14. MONITORING AGENCY NAME & ADDRESS(if different from Controlling Office)		**15. SECURITY CLASS. (of this report)** UNCLASSIFIED
		15a. DECLASSIFICATION/DOWNGRADING SCHEDULE

16. DISTRIBUTION STATEMENT (of this Report)

Approved for public release; distribution unlimited.

17. DISTRIBUTION STATEMENT (of the abstract entered in Block 20, if different from Report)

18. SUPPLEMENTARY NOTES

19. KEY WORDS (Continue on reverse side if necessary and identify by block number)

FRACTURE MECHANICS	FINITE ELEMENT SIMULATION	INITIATION AND GROWTH
TRANSVERSE CRACKS	EXPERIMENTAL CORRELATIONS	GROWTH STABILITY
EDGE DELAMINATIONS	LAYER THICKNESS EFFECTS	
ENERGY RELEASE RATE	MIXED MODE CRACKS	

20. ABSTRACT (Continue on reverse side if necessary and identify by block number)

The fracture mechanics of matrix-dominated cracks—multiple transverse cracks and edge delamination—has been presented in this report. Analytical models are developed which describe the initiation, growth and the growth stability of these two types of cracking mechanisms. A finite element crack-closure method is used to simulate the crack growth numerically; and an extensive experimental case study is conducted to correlate with the analytical models.

DD FORM 1473 EDITION OF 1 NOV 65 IS OBSOLETE

Foreword

This is the final technical report for the research program
supported by Air Force Office of Scientific Research through
Contract No. F 49620-79-C-0206 to Drexel University.

This report contains all the research results obtained during
the program period from 1, September 1979 to 30, September 1981.

Dr. A.S.D. Wang of Drexel University was the principal
investigator; he was assisted by George E. Law, Jr., a graduate
student of Mechanical Engineering Department, Drexel University.
Partial work was conducted at Lockheed Palo Alto Research Laboratory
through a sub-contract. Dr. Frank W. Crossman was the principal
investigator for that portion of the program; he was also assisted
by John Warren, a senior scientist at Lockheed.

The authors wish to acknowledge gratefully the generous support
from the Air Force Office of Scientific Research.

TABLE OF CONTENTS

TABLE OF CONTENTS

I. INTRODUCTION

Fracture failure in multi-layer epoxy-based composite laminates seldom begins with breaking of the load-carrying reinforcing fibers. Rather, small cracks in the matrix-phase of the material appear first, usually at a low stress level. Transverse cracks and free-edge delaminations are among the most often observed sub-laminate fracture modes in, e.g., glass-epoxy and graphite-epoxy composite laminates. Although these matrix-dominated crackings do not generally cause catastrophic laminate failure, these are capable of propagating into large proportions under sustained loading. Thus, the growth behavior of the sub-laminate cracks has been the subject of intensive research in recent years.

From a fracture analysis point of view, the growth mechanisms of sub-laminate crackings may be described at two different dimensional levels. The first approach is at the micromechanics level. At this level, quantities of dimension comparable to the fiber diameter must be considered. Thus, the analysis would distinguish the exact physical configurations in the fiber-matrix microstructure; and as far as fracture mechanisms are concerned, the analysis would also include the effects of micro-defects, such as voids, fiber-matrix disbonds, etc. Since the latter may distribute randomly throughout the material, any fracture analysis method based on micromechanics must also address the statistical characteristics of the material micro-defects.

Owing to the extreme complexity in the microstructures of any given fibrous composite, fracture analysis of sub-laminate cracks based on micromechanics is almost impossible if not impractical. Nevertheless, the approach has been applied extensively to study failure mechanisms of unidirectional fibrous composites, where fiber failure is predominant.

1

At a much larger dimensional level, a phenomenological fracture analysis may be performed. In this approach, each of the material layers in the laminate is idealized as a homogeneous anisotropic medium, where the fiber-matrix distinction disappears. The physical properties of the individually idealized layers are represented by some average values from that of the fiber and the matrix phases. Consequently, all of the micro-defects in the idealized layer become indistinguishable; and their resultant macroscopic effect on failure may be regarded as some inherent material property.

Generally, a crack of dimension much larger than the fiber diameter will be recognized at the macroscopic level, such as a transverse crack in a layer, or a delamination crack in a layer-interface. At this level of analysis, methods of the classical fracture mechanics may be used, where the effective properties of the material layers are required in order to perform the necessary stress analysis. In fact, it is at this level, material characterizations of various composite material systems are conducted in practice.

Research on the sub-laminate fracture growth in laminates has been mostly experimental. And serious analytical studies of the various growth mechanisms from either a microscopic approach or a macroscopic approach have been very limited (see, e.g., the review on fracture analysis of composites given recently in a treatise by Cherepanov [1]).

In what follows, a more detailed discussion will be given to the two types of sub-laminate crackings, which have been the focus of considerable recent interest. Specifically we shall discuss the growth behavior of transverse cracks and free edge delamination in graphite-epoxy composite laminates.

2

Transverse cracking is generally associated with the in-plane tensile stress which is normal to the fibers in a given material layer. Consider, for instance, the [0/90]$_s$ laminate under uniaxial tension as shown in Fig. 1.1. Multiple transverse cracks are shown to occur in the 90°-layer. Assume that the 90°-layer has a uniform tensile strength, then multiple cracks would appear simultaneously at a regular spacing when some critical stress is reached transverse to the fibers. The crack spacing is determined by the shear stress transfer zone on the 90/0 interface where the transverse crack terminates. Thus, first intuition would suggest that the critical stress in the 90°-layer at the onset of multiple cracking must be the tensile strength of the 90°-layer. The latter is, of course, a material property of the 90°-layer.
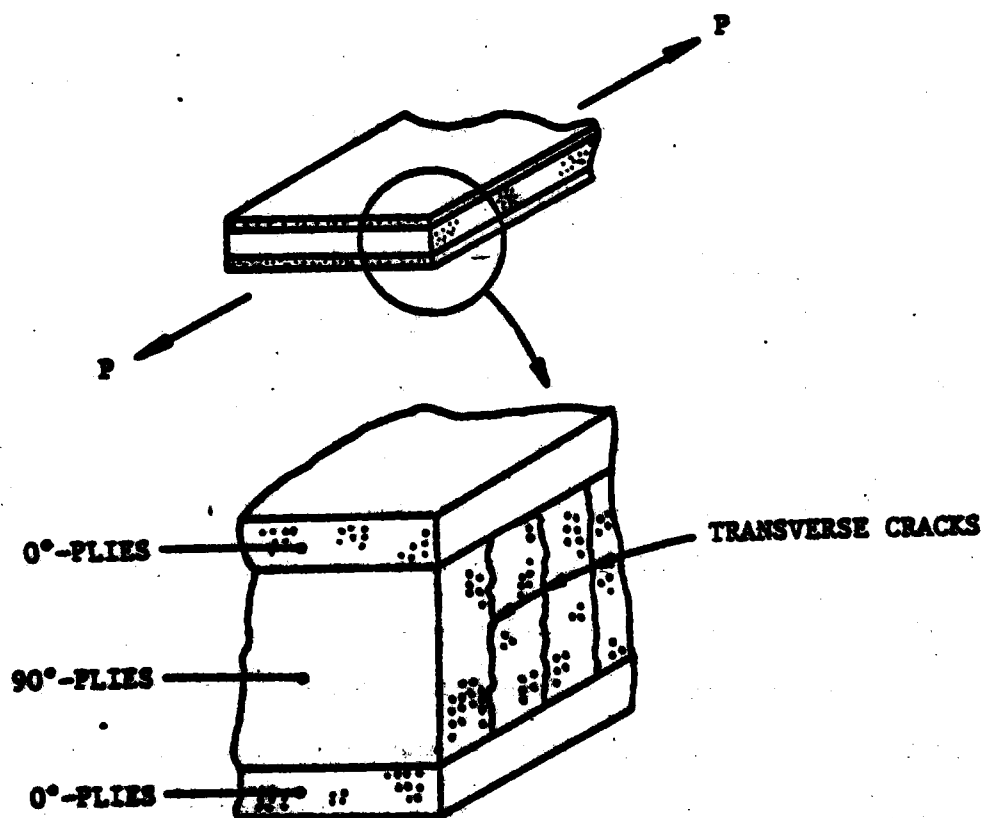
Figure 1.' Schematics of Multiple Transverse Cracks

3

Actually, experiments have indicated that the tensile stress in the 90°-layer at onset of transverse cracking varies greatly with the thickness of the 90°-layer itself. The general trend is that the critical tensile stress in 90°-layer increases as the actual thickness of the 90°-layer decreases. This layer-thickness effect was first documented experimentally by Bader, et al. [2], who tested laminates made of glass-epoxy and graphite-epoxy composites.

Bader, et al. [2] attributed the layer-thickness effect on transverse cracking to the constraining actions from the adjacent 0°-layers. The presence of the 0°-layers not only arrests the crack, but also restrains it from forming in the first place. Depending on the thickness of the 90°-layer, the quantity which creates transverse cracks is associated with the amount of strain energy stored in the 90°-layer.

The exact kinematics in the transverse cracking formation are not clear. A closer examination of the cracking process indicates that the crack generally follows the fiber-matrix interface, when viewed in the plane. For example, Fig. 1.2 shows an x-ray plane-view of a $[\pm 25/90_2]_s$ graphite-epoxy laminate. It is seen that all the transverse cracks span the entire width of the test specimen. Similarly, a photo-micrograph in the thickness view, is shown in Fig. 1.3 for the same laminate. Here, the transverse cracks span across the thickness of the 90°-layer and terminate at the 90/25 interfaces. These photographs do not reveal the actual growth path of the transverse cracks. Rather, it tends to suggest a sudden formation of a large plane crack, confined by the thickness of the 90°-layer and the width of the specimen. The dynamic nature in the crack formation requires further verification, however.

direction
of loading
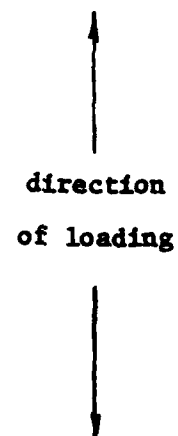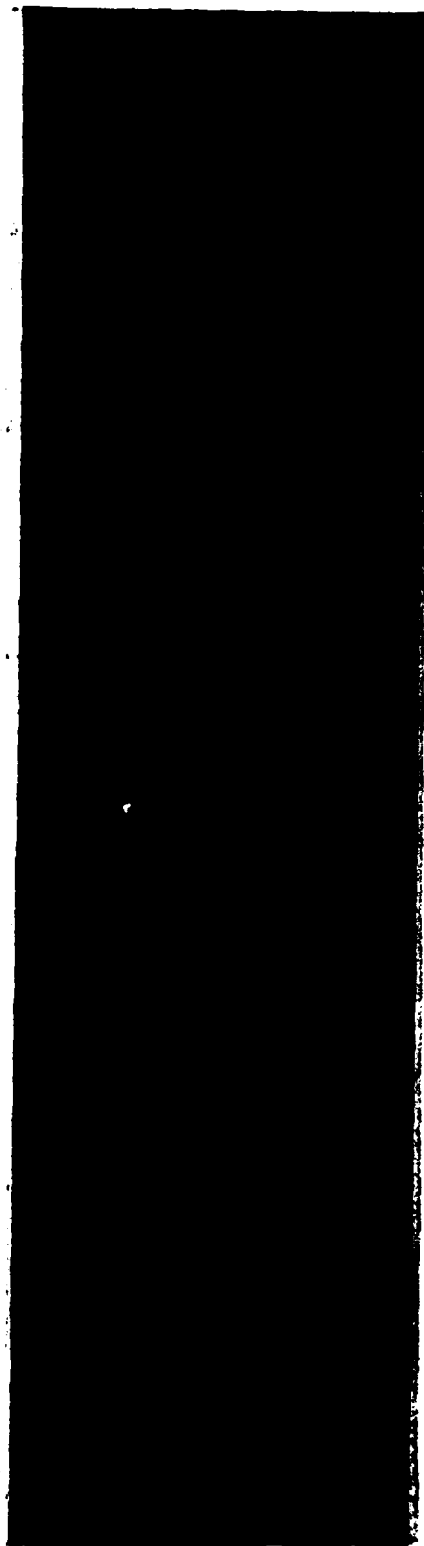
Figure 1.2   A Plane View X-Radiograph of Transverse Cracks
in $[\pm 25/90_2]_s$ Laminates

+25

-25

90

90

90

90

-25

+25
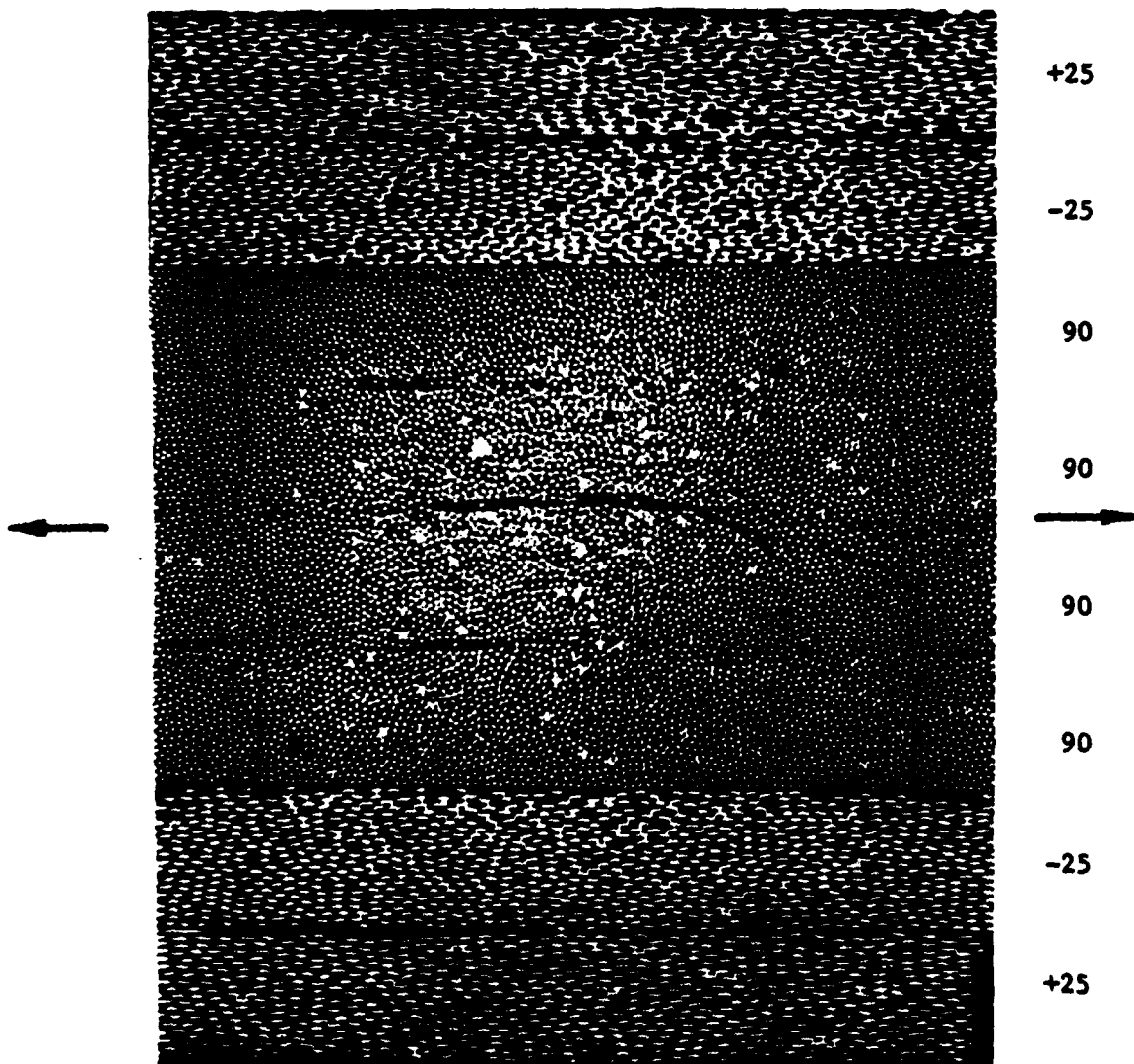
Figure 1.3 A Thickness View Photomicrograph Showing Transverse Cracks
in 90°-layer of a $(\pm 25/90_2)_s$

Examination of the transverse crack surface by scanning electronic microscope reveals a generally rough failure surface scattered with tiny epoxy debris and some broken fibers. Clearly, the cracking path is not entirely confined in the matrix phase of the composite.

Let us now turn to the problem of free edge delamination which is another frequently observed sub-laminate fracture mode in epoxy-based laminates. Fig. 1.4 illustrates schematically a free edge delamination crack in a straight-edge specimen under uniaxial tension. It shows again a plane crack which forms along the free edge of the laminate and propagates inward along an interface of two adjacent layers.

The driving force for the free edge delamination crack stems from the interlaminar stresses that exist near the free edge region of the laminate. These stresses are generally singular in nature with high stress gradient. As the cracking forms and propagates inward, the singular interlaminar stress field moves also with the crack-tip. The process is apparently stable as is evidenced by numerous experiments. On the other hand, there is no crack-arresting mechanisms in the process; and the crack can therefore propagate indefinitely until the laminate is separated through the cracking interface. At this point, failure of the laminate is resulted.
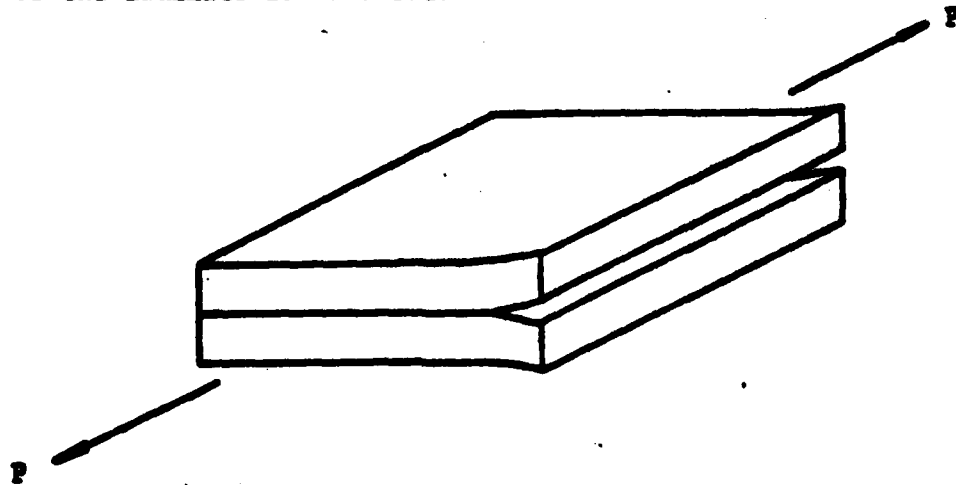
Figure 1.4 Schematics of Free Edge Delamination

7

Fig. 1.5 shows the x-ray plane-view pictures of a [±45/0/90]$_s$ graphite-epoxy laminate undergoing free-edge delamination at three different loading stages, where a stable crack growth is indicated. The interface in which the crack is supposed to be contained should be the mid-plane of the laminate. However, a side-view micrograph of the same laminate taken at the loading stage (b) is shown in Fig. 1.6. It is seen here that the edge crack is actually formed within the 90°-layer, but it zig-zags along the length of the specimen. Apparently, the crack is not always confined in any one given layer interface.

(a)   (b)   (c)
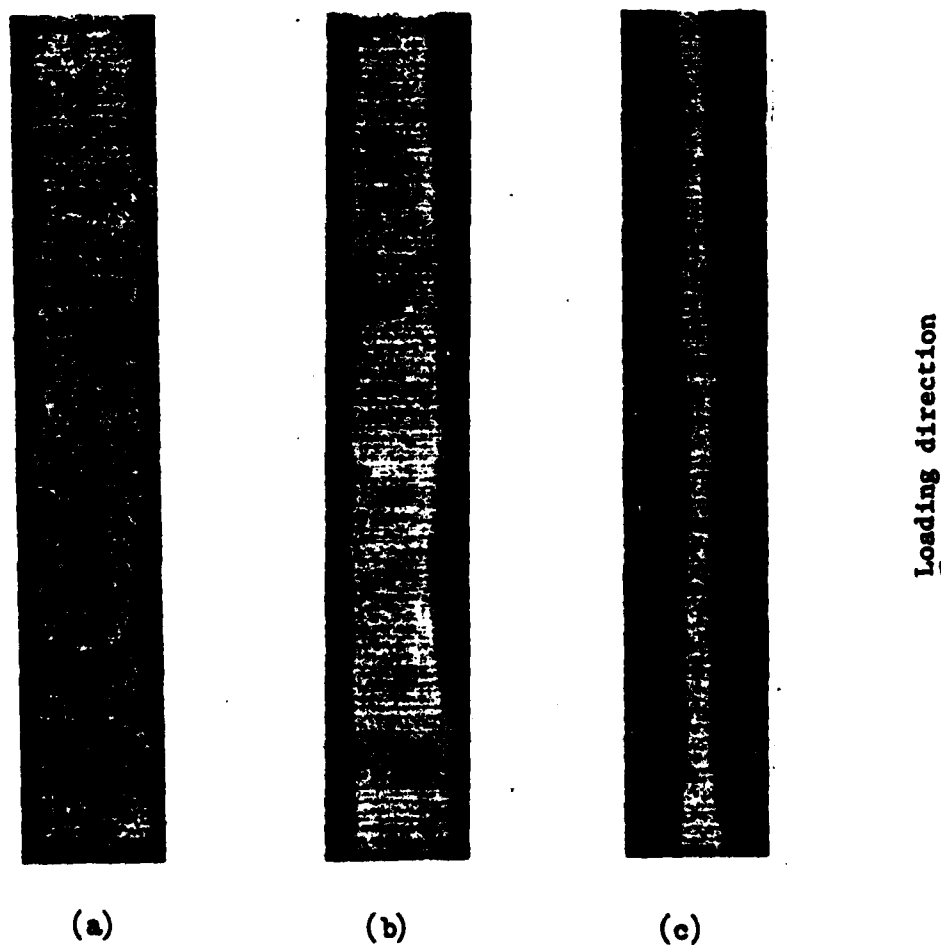
Figure 1.5   X-ray Pictures of a [±45/0/90]$_s$ Graphite-Epoxy
             Laminate under Going Delamination in the Mid-Plane

8
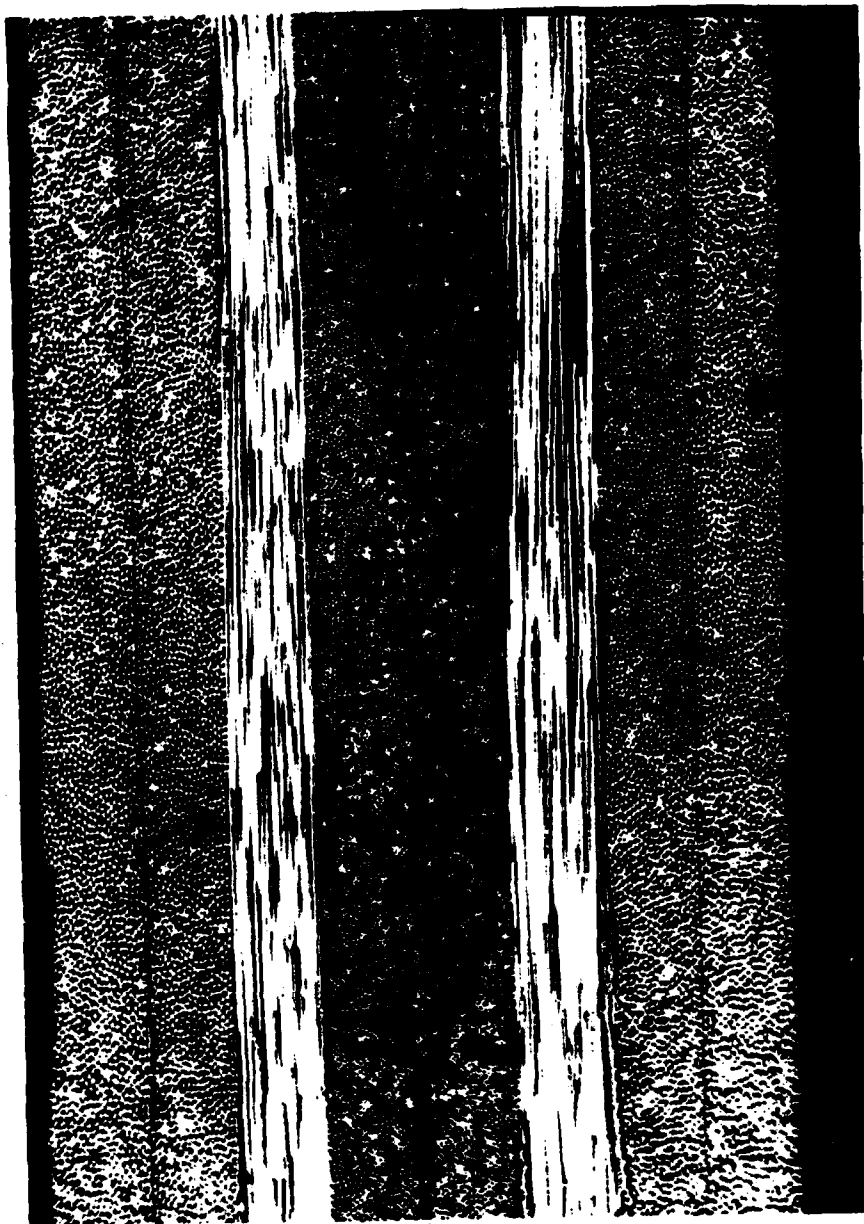
Figure 1.5 Micrograph Showing Free Edge Delamination in the 90 layer of a Graphite-Epoxy $(\pm 45/0/90)_s$ Laminate

Another side-view micrograph of this laminate taken at the loading stage (c) is shown in Fig. 1.6. Of particular interest is the formation of other delamination cracks in the $\pm 45°$-interfaces and the 0/45 interfaces. These cracks are generally in shear-dominant modes. Clearly, the growth process of free edge delamination is much more complicated than the transverse cracking process that has been discussed earlier.

Analytical investigations of the free edge delamination problem have been mainly efforts for calculating the boundary layer interlaminar stresses. Almost without any exception, all the calculation methods were based on the effective property assumption, that the material layers in the laminate are individually homogeneous (but anisotropic) media. Within this assumption, material and geometrical discontinuities exist only across the layer interfaces.

Even at this dimensional level, the elasticity boundary-value problem is quite complicated; only numerical solutions for the free edge stress field have so far been obtained [3-6]*.

The knowledge of the free edge stresses has provided qualitative correlations with some delamination experiments. For example, in a series of strength tests, Bjeletich, et al. reported the average tensile strength of six families of quasi-isotropic laminates by alternating the stacking sequence of the 0°, 90°, and $\pm 45°$ layers [9]. An edge stress analysis identified correctly that the laminate of $[0/90/\pm 45]_s$ developed a compressive σ_z stress along the free edge. Consequently, the laminate suffered no delamination until final failure.

---

* Recently, Wang and Choi [7] have determined the elasticity solution for the singularity of the edge stresses. Other efforts in computing the free edge stresses are discussed more extensively in a survey paper by Salamon [8].

10
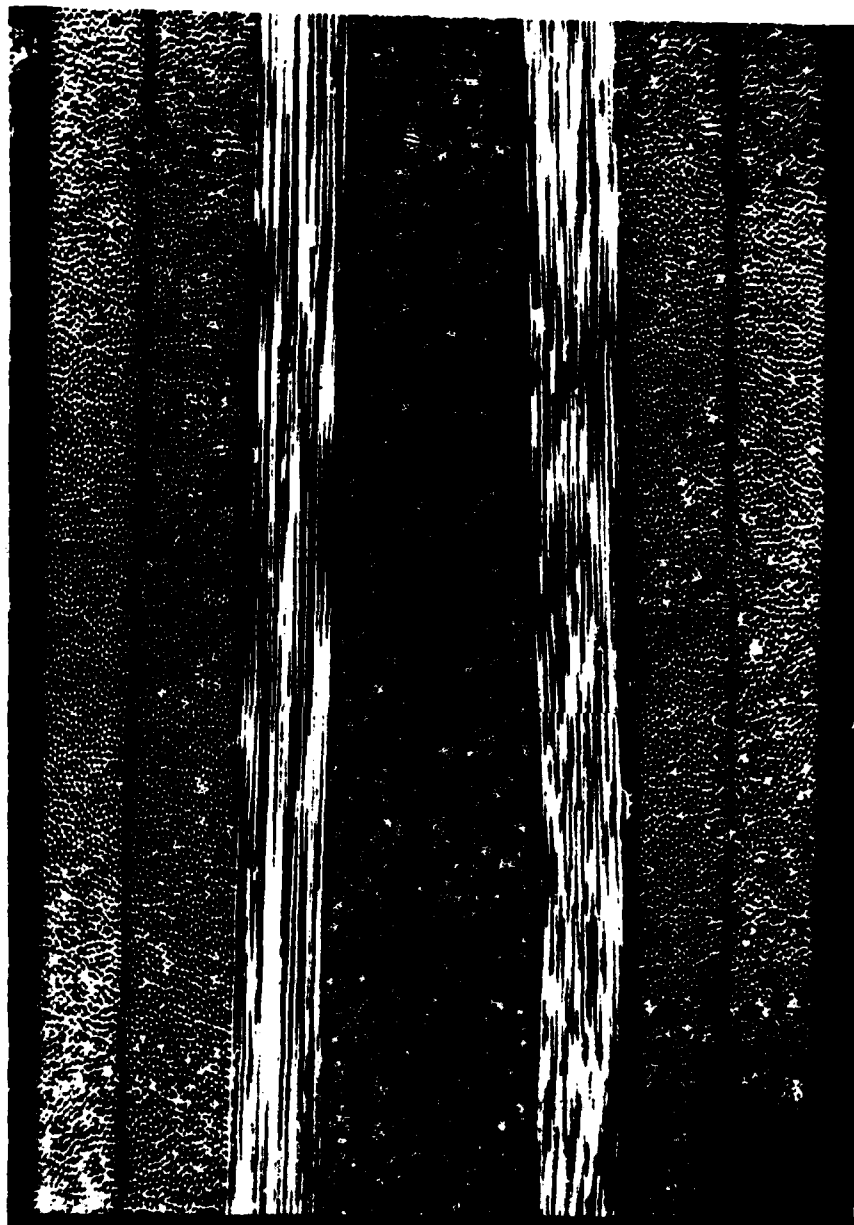
Figure 1.6 Micrograph Showing Delamination Cracks at Several Interfaces at Late Stage of Loading of a Graphite-Epoxy $[\pm45/0/90]_s$ Laminate

11

On the other hand, the laminate of $[\pm45/0/90]_s$ construction developed a tensile σ_z stress along the free edge boundary, which caused prematured delamination; and, the growth of the delamination resulted in a lowered laminate tensile strength.

In a series of tests using graphite-epoxy laminates, Rodini, et al. [10] found that the critical stress at the onset of edge delamination in a $[\pm45_n/0_n/90_n]_s$, n = 1,2,3 family varied greatly with the value of n. The critical stress decreases at the rate of about $\sqrt{n}$. In addition, the location and the mode of crack also varied with n. Clearly, the actual thickness of the material layers in the laminate influences the mechanisms of delamination. Yet, a free edge stress analysis for the laminates would yield identical edge stress field for all values of n. Thus, a stress analysis alone cannot explain the initiation and growth events in the delamination process.

The layer-thickness effect on edge delamination is, coincidentally, similar in nature with that found in the transverse cracking processes. In both cases it requires a rigorous physical and mathematical explanation.

All of this points to the need for a fracture analysis of the problems. In particular, the critical conditions under which a crack initiates and propagates must be defined. And the growth behavior as a function of loading also needs a closer examination.

As discussed earlier, transverse cracks and delamination are sub-laminate cracks, which may be analyzed at two different dimensional levels. At the microscopic level, the basic assumption is that in each material layer there is a distribution of micro-defects. And, a similar micro-defects distribution may also exist on the layer interfaces. Thus, increasing the thickness of the material layer increases the probability of crack initiation and growth.

12

This reasoning can certainly explain, albeit qualitatively, the observed layer-thickness effect on transverse cracking [2] and edge delamination [10]. But the analysis must include the interrelationships between the stress fields, the defects, defect interactions and their coalescence mechanisms at the microscopic level. This approach, however, is practically unattainable.

The alternative is to perform a fracture analysis at the macroscopic level, where a stress analysis based on layer-elasticity may be coupled with the classical fracture mechanics. Within this context, one must perform a number of fundamental preparations in order to construct a physically realistic fracture model. In particular, some conceptual and technical questions must be resolved first.

As in any analytical model construction, idealization and simplication are made in order to reduce mathematical complexity. In the case of free-edge delamination, for instance, one may idealize the crack growth as a self-similar, or co-planar crack contained in an interface between two layers. The growth is one-dimensional and the crack front is represented by a point. Similarly, transverse cracking may also be idealized as a self-similar crack along the matrix-fiber interface in the $90°$-layer. In either case, the crack surface is assumed flat and smooth. In reality, of course, the crack surface is ragged and warped depending on the exact nature of the crack, even when viewed at the macroscopic level. But, the idealization may be tolerated in the overall modeling, if the material property (e.g., the critical energy release rate, G_c or K_c) is measured as a bulk quantity, and the size of crack is large. This kind of idealization is, on one hand, a mathematical necessity; and on the other hand, it must be adjudicated by physical experiment.

The above consideration brings upon another conceptual question, which is how G_c or K_c should be physically determined. Although transverse cracks and edge delamination may all be regarded as matrix-dominant cracks, their individual resistance against crack growth when measured macroscopically could differ considerably. Consider, for example, the two different crack actions in a unidirectional laminate as shown in Fig. 1.8. Case (a) illustrates a mode-I delamination action between 0°/0° layers, and case (b) depicts a mode-I crack action between 90°/90° layers. The two crack actions may produce distinctive crack surfaces at the microscopic level, and thus give different values for G_c which is measured at the macroscopic level.

In a series of tests, conducted recently at Texas A & M University [11,12], different values for the critical energy release rate, G_c, were found for a unidirectional composite, depending on how the crack is propagated. In particular, for the AS-3502 composite system, G_c measured under 0°/0° delamination action, case (a) Fig. 1.8, was about 0.8-0.9 lb/in; while G_c, under 90°/90° cracking action, case (b), Fig. 1.8, was found to be 1.2-1.35 lb/in. G_c for the neat resin (without reinforcement) had a value of only 0.4 lb/in. The differences all stem from the individual characteristics of the crack surfaces.

This clearly raises the question of whether G_c can be regarded as a general material property for the class of the so-called matrix-dominated cracks. The difficulty comes, obviously, from the fact that G_c is measured without regard to the microscopic details of the cracking surfaces.

Closely related to the question of G_c, there is also some concern about a possible non-linear yielding that occurs in the vicinity of the crack-tip, especially under shearing crack actions. In a recent experiment by Vanderkley [13], it was shown that the total energy release rate measured under mixed-mode ($G_{I,II}$) crack action is much larger than under a pure mode-I action.
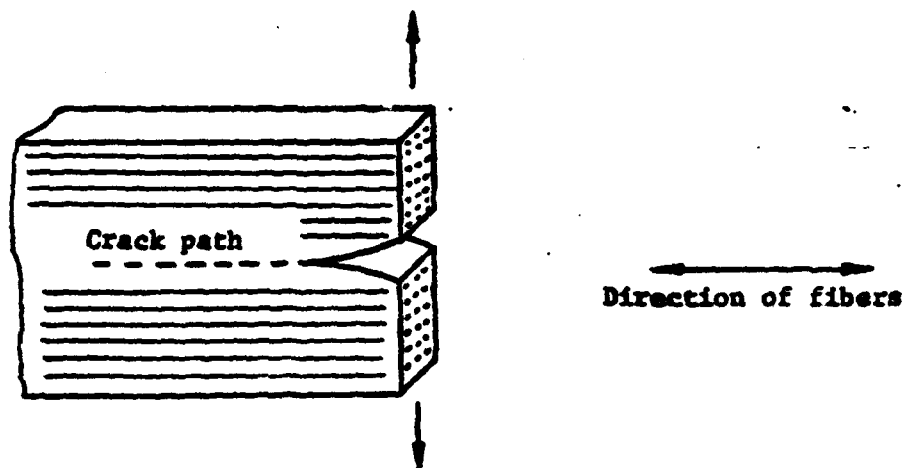
(a) 0°/0° Delamination Action, Mode-I
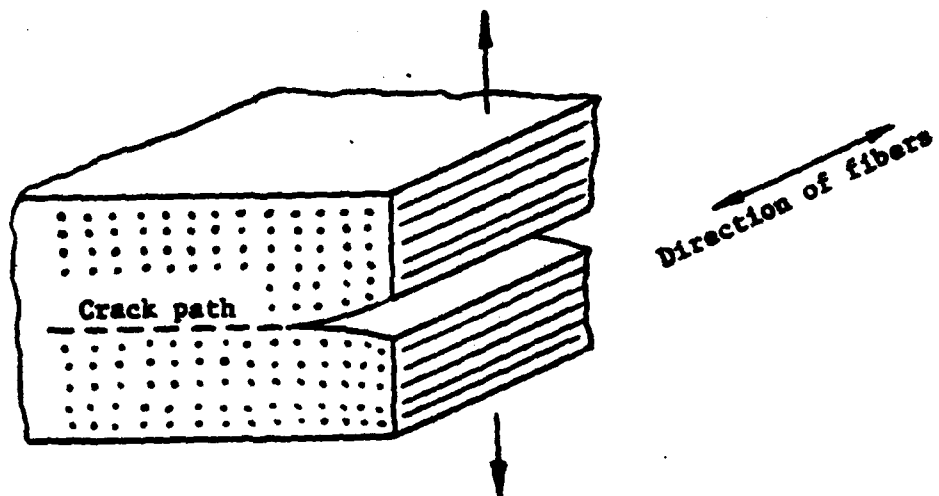
(b) Transverse Cracking Action(90°/90°), Mode-I

Figure 1.8 Schematics of Two Different Cracking Actions
in Unidirectional Laminate

15

This suggests that energy dissipation in the mixed-mode cracking may contain some amount of inelastic deformation energy. In view of the fact that the epoxy matrix generally exhibits a considerable inelasticity under shearing deformation, the measured value of G_c under mixed-mode crack action may depend on the amount of shearing action.

Clearly, all these questions require in-depth investigation before a reliable fracture model can be formulated.

It is therefore the purpose of this research to conduct a detailed and comprehensive examination into the growth mechanisms of transverse cracking and free edge delamination. The main objective is to formulate a predictive fracture model which is capable of describing the basic behavior in the two types of sub-laminate crack processes. To this end, the macroscopic approach based on layer-elasticity is taken, and the physical concepts of the classical fracture mechanics will be employed. In order to resolve some of the fundamental questions associated with this approach, an extensive experimental study is also conducted, with results correlated with the fracture analysis.

Section II details the fracture model development. A review of the basic methods in classical fracture mechanics is included. And, the special method of the crack-closure integral is singled out for adaptation in a finite element computational scheme. In this section, the crack initiation, growth and growth stability criteria for transverse cracking and free edge delamination are proposed.

Section III contains the results and other data documented in the experimental case study. It includes the macroscopically measured material properties, crack events in the $[0/90_n]_s$, n = 1,2,3,4 family, crack events in the $[\pm 25/90_n]_s$, n = 1/2,1,2,3,4,6,8 family, and the crack events in the $[\pm 45_n]_s$,

16

n = 2,3 family. In particular, in the $[\pm 25/90_n]_s$ family, both transverse cracking and edge delamination occur either independently or interactively, depending on the value of n. Other peculiar aspects in the crack events are summarized and discussed.

Numerical modeling based on the methods developed in Section II are conducted for the laminates tested in Section III. Thus, a complete correlation between the analysis and experiment is presented in Section IV. This includes the modeling of the transverse cracking, free edge delamination and their interactions effect.

A concluding discussion on the gains as well as shortcomings in the fracture model is given in Section V.

II. DEVELOPMENT OF FRACTURE MODELS

In the previous section, we have discussed some aspects of the physical process of transverse cracks and edge delamination in epoxy-based laminates. It is found that the fracture events cannot be explained from the standpoint of the concept of strength as a constant material property. Actually, there is a broad range of failure processes for which the concept of strength is not applicable. This fact is particularly well known for brittle failures. The essence of the classical fracture mechanics is not to apply the strength concept, but base the theory on the actual process of fracture. It is founded on the work of Griffith [14], published originally in 1920.

2.1 The Griffith's Energy Release Rate Concept

Griffith's original work [14] is concerned with a thin, brittle plate which is uniformly stretched in one direction by σ, Fig. 2.1. The plate has a through-crack of length 2a, orientated transverse to the direction of the applied stress σ. The length of the crack is assumed small compared to the dimension of the plate; $a \ll L$; $a \ll W$. Griffith introduced the surface energy of the brittle material and formulated the criterion according to which the existing crack begins to propagate unstably. He postulated that an increase in the crack size causes a decrease in the stored strain energy near the crack-tip; and the loss of the strain energy is converted entirely into surface energy. The latter is the result of an increase in the free surface area due to the crack extension.

Let U and U_0 be the total strain energy of the plate with and without the crack, respectively. And, let $\Delta U = U_0 - U$ be the loss of strain energy of the plate due to the presence of the crack. Then, for the existing crack of size 2a, the Griffith criterion states that the crack begins to propagate when

18
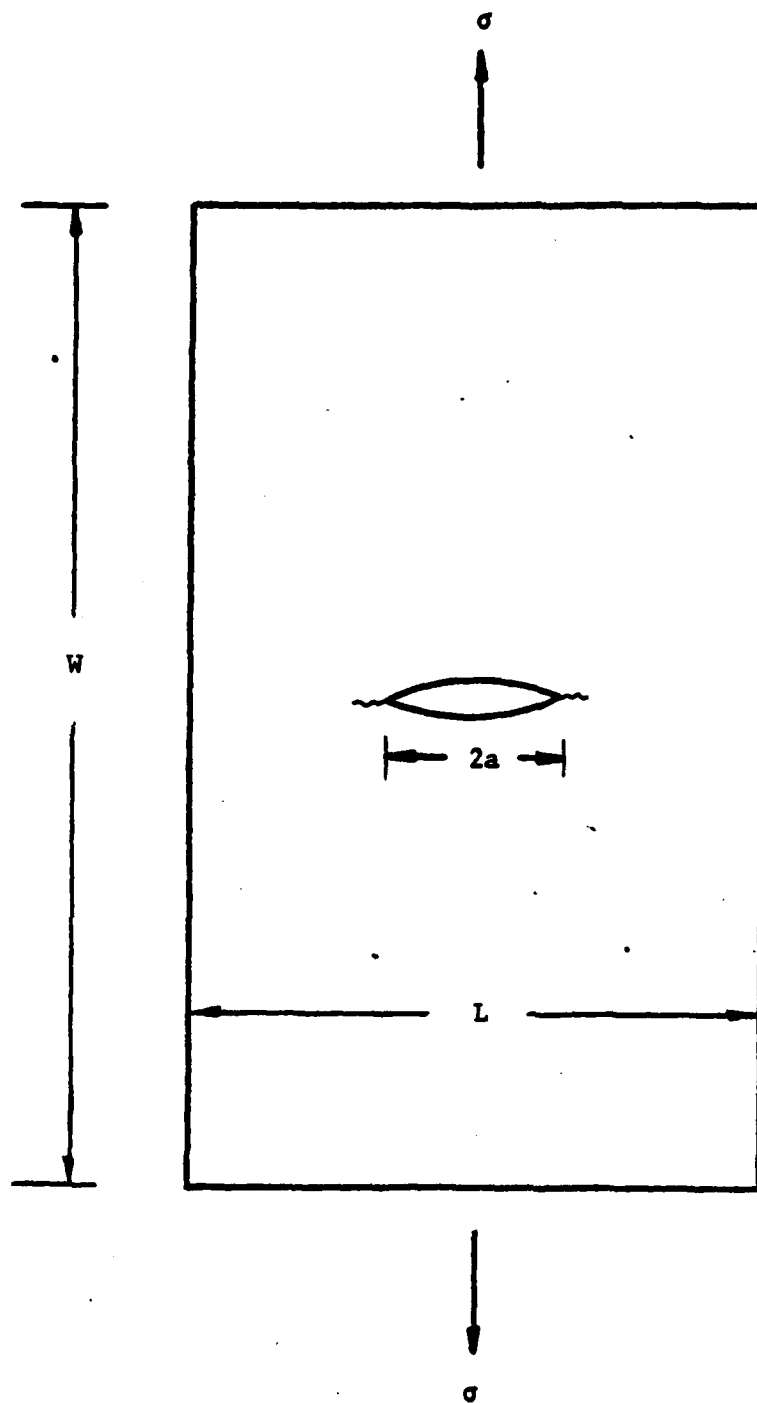
Figure 2.1 Griffith's Crack Problem. L >> a, W >> a.

19

$$\frac{\partial}{\partial a} (\Delta U) da \geq (4\gamma) da \qquad (2.1)$$

where γ is the material surface energy of a unit of free surface.

For the Griffith problem (plane stress), ΔU is given by

$$\Delta U = \frac{\pi}{2} \frac{a^2 \sigma^2}{E} \qquad (2.2)$$

Upon substitution into (2.1), the following dependence of the critical stress on crack size is obtained:

$$\sigma_{cr} = \left(\frac{2E\gamma}{\pi a}\right)^{1/2} \qquad (2.3)$$

According to Eq. (2.3), the crack of original length 2a remains unchanged until the applied stress σ reaches the value given by (2.3); at this instant a dynamic process of crack growth begins.

The Griffith equation (2.3) brings upon two important practical questions. The first is that using (2.3), $\sigma_{cr} \to \infty$ as $a \to 0$. Of course, no real material can sustain an infinite stress. In fact, given a plate having no crack at all, one finds only a finite strength for the plate. This contradiction is circumvented by introducing the concept of inherent material flaws, that are assumed to exist naturally within the plate. The real physical identity of the flaws is lost within the frame-work of the "continuum assumption" from which stresses, strain energy, etc. are calculated. In reality, the flaws exist, perhaps, at the dimensional level of the grain-boundary, or the molecular structure of the material. The macroscopic effect of these microflaws is then represented by assuming a macroscopic crack of size a_0, from which the no-crack strength of the plate can be calculated from (2.3). Clearly, the existence of a_0 at the macroscopic level can only be viewed as a necessary postulation.

Another question is related to the definition of γ, the free surface energy. Actually, it represents the irreversible work required to create a unit free surface area. For brittle material such as glass, crack growth as defined by (2.3) has been shown to be quite valid. For most other structural materials, the crack-tip region usually exhibit some degree of ductile deformation. Early studies by Irwin [15], Orowan [16] and others led to the concept of the so-called "quasi-brittle fracture." According to this concept, Eq. (2.3) is also correct for most materials under conditions of quasi-brittle fracture, if the quantity γ is replaced by the irreversible energy dissipated in the surface region of the crack per unit area of free surface. This last quantity depends on the ductility or inelasticity of the material near the crack-tip; and it is usually found to be orders of magnitude larger than the theoretically calculated value of the material's free surface energy γ.

The foregoing discussions become practically more important when we try to describe crack-like failures in composite materials. The fundamental assumptions in the Griffith theory must be propertly re-interpretated in order for it to apply to the fracture problems of composites.

As has been discussed in Section I, practical stress analysis for multi-layer laminates can be performed only at the level of layer-elasticity. That is the individual layer is idealized as a homogeneous medium in much the same manner as the "continuum" assumption in the theory of elasticity. Consequently, when we analyze a crack-like failure in this idealized material, the same concern arises in identifying properly the quantity a_0 and the quantity γ if the Griffith theory is to be employed. As before, these quantities must be considered a material property and are measured at the dimensional level where the stress analysis is performed. As far as composite materials are concerned,

21

the size of a_0 can be very large, depending on the size and the distribution of the microflaws. Similarly the quantity γ has to be the averaged value over a large crack surface area.

In this sense, the Griffith equation (2.3) can be generalized to treat the types of crack growth problems which are found in layered composites.

Now, consider the quantity ΔU in (2.1). Since U_0 does not depend on a, the Griffith criterion may be rewritten as

$$\frac{\partial U}{\partial a} \geq \frac{\partial S}{\partial a} \qquad (2.4)$$

where S is the total surface energy of the solid in the context of the afore-mentioned "quasi-brittle" fracture.

The quantity $\partial U/\partial a$ depends on the stress field near the crack-tip, which in turn depends on the geometry of the crack. It represents the driving force in propagating the crack and is commonly referred to as the available strain release rate, $G(a)$, a function of crack size a. The quantity $\partial S/\partial a$ depends on the imcrostructure of the crack surface and it represents the resistance of the material against the crack propagation. For material of uniform property, $\partial S/\partial a$ is independent of a. It is commonly called the critical energy release rate G_c, which is identified as 2γ.

Thus, the Griffith criterion (2.4) becomes,

$$G(a) \geq G_c \qquad (2.5)$$

Accordingly, the development of the classical fracture mechanics rests upon the calculation of $G(a)$ analytically, and the measurement of G_c physically. In view of the mathematical complexity in the singular stress field near the crack-tip and the practical uncertainties involved in the material behavior at failure, both tasks have not been a simple matter.

2.2 Irwin's Crack-Closure Integral

For plane problems in elastic homogeneous solids, the strain and displacement variables are independent of one of the Cartesian coordinates, say z. In this general case, the singular stress field near the crack tip can be represented by analytical functions in the theory of complex variables [17]. Generally, stress field solutions are obtained for three particular modes of crack action. These three modes, illustrated in Fig. 2.2, are known respectively as mode I or opening mode, mode II or sliding mode and mode III or tearing mode. For isotropic material, the distribution of stresses near the tip of an arbitrary brittle crack undergoing pure mode I extension is given by [18].

$$\sigma_x = \frac{K_I}{\sqrt{2\pi r}} \cos \frac{\theta}{2} (1 - \sin \frac{\theta}{2} \sin \frac{3\theta}{2}$$

$$\sigma_y = \frac{K_I}{\sqrt{2\pi r}} \cos \frac{\theta}{2} (1 + \sin \frac{\theta}{2} \sin \frac{3}{2} \theta$$

$$\sigma_z = \nu(\sigma_x + \sigma_y) \qquad\qquad (2.6)$$

$$\tau_{xy} = \frac{K_I}{\sqrt{2\pi r}} \sin \frac{\theta}{2} \cos \frac{\theta}{2} \cos \frac{3\theta}{2}$$

$$\tau_{xz} = \tau_{yz} = 0 .$$

23
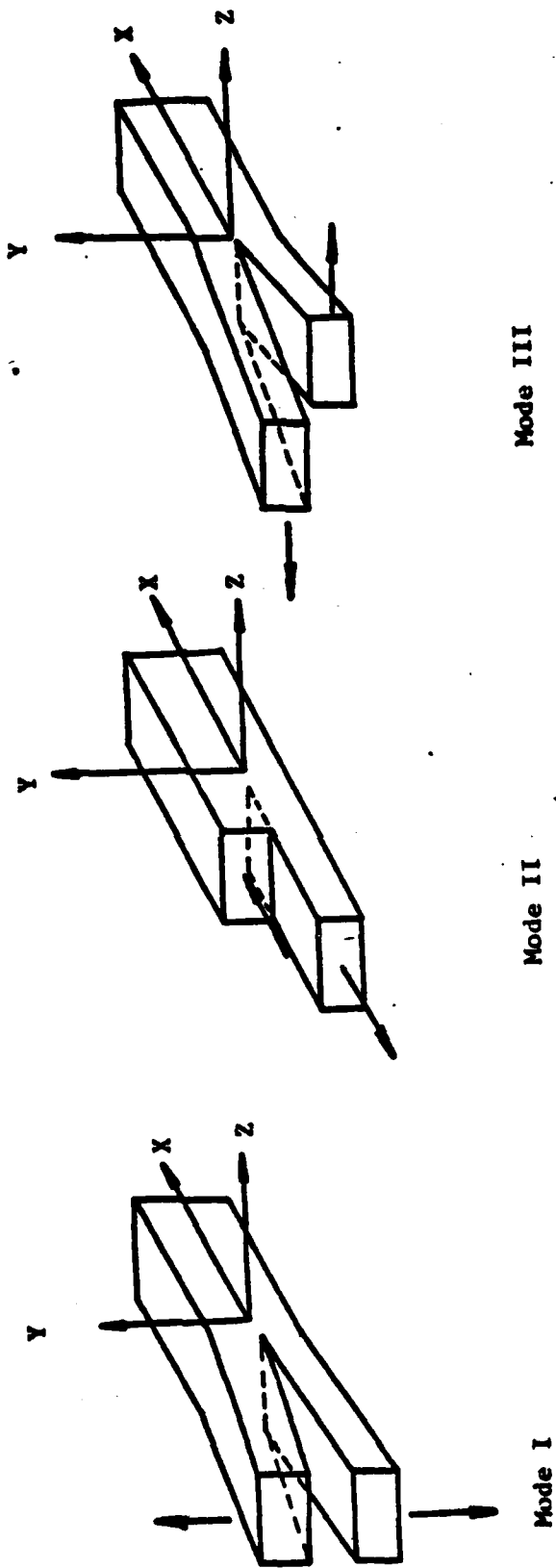
Figure 2.2   The Three Crack Extension Modes.

24

And the crack-tip stress field of a mode II crack is

$$\sigma_x = - \frac{K_{II}}{\sqrt{2\pi r}} \sin \frac{\theta}{2} \left(2 + \cos \frac{\theta}{2} \cos \frac{3}{2} \theta\right)$$

$$\sigma_y = \frac{K_{II}}{\sqrt{2\pi r}} \sin \frac{\theta}{2} \cos \frac{\theta}{2} \cos \frac{3}{2} \theta$$

$$\sigma_z = \nu(\sigma_x + \sigma_y) \tag{2.7}$$

$$\tau_{xy} = \frac{K_{II}}{\sqrt{2\pi r}} \cos \frac{\theta}{2} \left(1 - \sin \frac{\theta}{2} \sin \frac{3}{2} \theta\right)$$

$$\tau_{yz} = \tau_{xz} = 0.$$

And the crack-tip stress field of a mode III crack is

$$\tau_{xz} = - \frac{K_{III}}{\sqrt{2\pi r}} \sin \frac{\theta}{2}$$

$$\tau_{yz} = \frac{K_{III}}{\sqrt{2\pi r}} \cos \frac{\theta}{2} \tag{2.8}$$

$$\sigma_x = \sigma_y = \sigma_z = \tau_{xy} = 0.$$

The real parameters K_I, K_{II} and K_{III} are known as the stress intensity factors, which depend generally on the shape of the body, loading, location and size of the crack.

Knowing the crack-tip stress field and the functional dependence of the stress intensity factors on the crack size a, the corresponding value of the available energy release rate G(a) can be calculated.

$$G(a) = \frac{1-\nu^2}{E} K_I^2 \quad \text{(plane strain)} \tag{2.9}$$

or

$$G(a) = \frac{1}{E} K_I^2 \quad \text{(plane stress)} \tag{2.10}$$

25

In the general case of mixed-mode crack action, the energy release rate is given by

$$G(a) = \frac{1-\nu^2}{E} (K_I^2 + K_{II}^2) + \frac{1+\nu}{E} K_{III}^2. \qquad (2.11)$$

Thus, by applying the Griffith criterion (2.5), we relate G_c as follows:

$$G_c = \frac{1-\nu^2}{E} (K_{Ic}^2 + K_{IIc}^2) + \frac{1+\nu}{E} K_{IIIc}^2. \qquad (2.12)$$

In particular, for pure mode I crack extension,

$$G_{Ic} = \frac{1-\nu^2}{E} K_{Ic}^2 \quad \text{(plane strain).} \qquad (2.13)$$

And similarly,

$$G_{IIc} = \frac{1-\nu^2}{E} K_{IIc}^2 \qquad (2.14)$$

$$G_{IIIc} = \frac{1+\nu}{E} K_{IIIc}^2. \qquad (2.15)$$

From the original statement of Griffith, we can identify only $G_c = G_{Ic} = 2\gamma$. For mixed-mode cracks, experience has shown that the value of G_c depends on the ratios of K_I/K_{II} and K_I/K_{III}. In fact, in most brittle materials, G_{Ic} is much less than G_c found under mixed-mode actions.

Thus, traditionally some semi-empirical crack growth criteria are used, depending on the particular situation. These criteria are in the general form of

$$f(K_{Ic}, K_{IIc}, K_{IIIc}) = 0. \qquad (2.16)$$

Note that in a criterion such as (2.16), the quantities K_c's and G_c's are interchangeable through the one-to-one relations (2.13) to (2.15).

Relations between K and G for orthotropic homogeneous media with the crack orientated along one of the major axes can also be obtained [19]. But,

for layered media such as composite laminates, an explicit relationship between K and G is usually not available. Moreover, in a generally aniso-tropic solid, the mode I, mode II and mode III crack actions are mutually coupled.

Even with isotropic media, the evaluation of the stress intensity factors may become difficult if not untractable. Irwin [20] showed that the elastic strain energy released during an incremental crack extension can be equated to the work done in closing the incremental crack. In what is known as the crack-closure representation, the method provides for a direct determination of G's from the crack-tip stresses and displacements.

Let Δa represent an infinitesimal crack extension from the initial size of a as shown in Figure 2.3. Let $\Delta \bar{u}$ be the relative displacements between the mating crack surfaces along Δa when the crack is open as in Figure 2.3b. Let $\bar{\sigma}$ be the surface stress distribution along Δa when the crack is closed as in Figure 2.3c. Then the work done to close the crack extension is given by

$$\Delta W = 1/2 \int_0^{\Delta a} \bar{\sigma} \cdot \Delta \bar{u} \; da \qquad (2.17)$$

Thus, by means of Irwin's crack closure equivalence, the available energy release rate G, for a crack of size a, is expressed by the integral,

$$G(a) = \lim_{\Delta a \to 0} \frac{1}{2\Delta a} \int_0^{\Delta a} \bar{\sigma} \cdot \Delta \bar{u} \; da \qquad (2.18)$$

Substituting the components of the surface stresses $\bar{\sigma}$ and the relative dis-placements $\Delta \bar{u}$ into equation (2.18) yields G in component form as
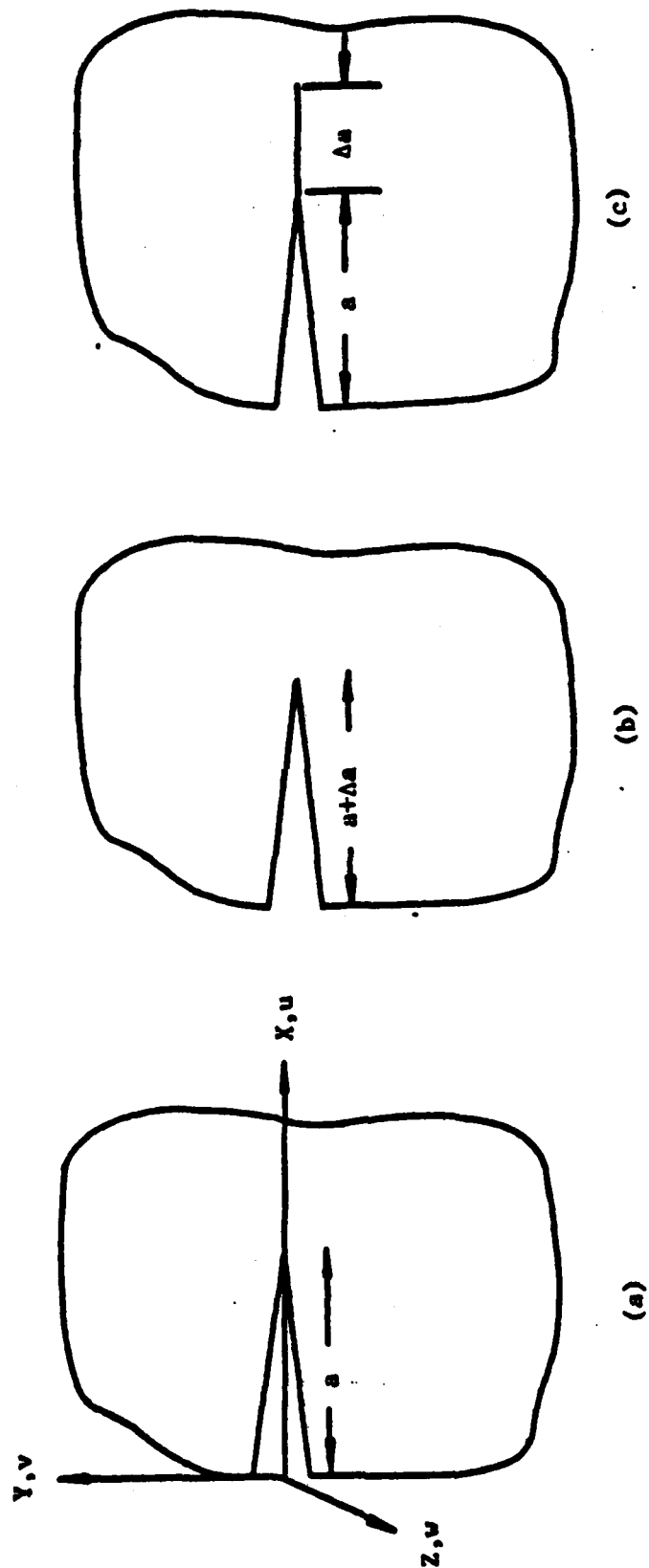
Figure 2.3   Schematic of Crack Closure Technique

28

$$G_I = \lim_{\Delta a \to 0} \frac{1}{2\Delta a} \int_0^{\Delta a} \sigma_y \, \Delta v \, da$$

$$G_{II} = \lim_{\Delta a \to 0} \frac{1}{2\Delta a} \int_0^{\Delta a} \tau_{xy} \, \Delta u \, da \qquad (2.19)$$

$$G_{III} = \lim_{\Delta a \to 0} \frac{1}{2\Delta a} \int_0^{\Delta a} \tau_{yz} \, \Delta w \, da$$

where G_I, G_{II}, G_{III} denote the mode I, mode II and mode III components respectively; and the total energy release rate under generally mixed-mode crack action is,

$$G(a) = G_I + G_{II} + G_{III}. \qquad (2.20)$$

The crack-closure representation is particularly convenient for adaptation in numerical computation. Other methods such as the well known J-integral technique [21,22] are also used to evaluate $G(a)$. These, however, will not be detailed here, as they are not pertinent to our subsequent development.

2.3 Finite Element Representation

A numerical technique to calculate the strain energy release rate $G(a)$ has been presented by Rybicki and Kanninen [23]. Their approach involves a finite element solution of Irwin's crack closure integral given in (2.18). In the finite element representation, the continuous stress and displacement fields of the solid are approximated by the nodal forces and displacements, respectively. Fig. 2.4 illustrates the finite element representation of a crack tip region. Here, a crack of length a is shown with the crack tip at node c. The finite element solution determines the displacement components $(u,v,w)_c$ of the crack tip node c. An incremental crack extension Δa is introduced by replacing the crack tip node c with two separate nodes f and g as shown.

29
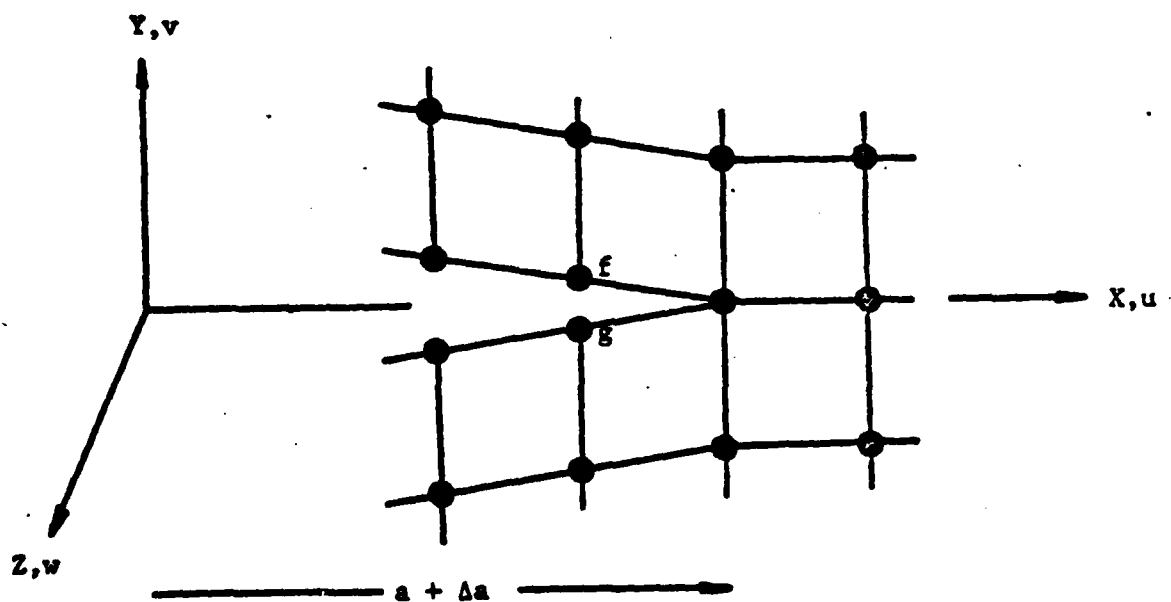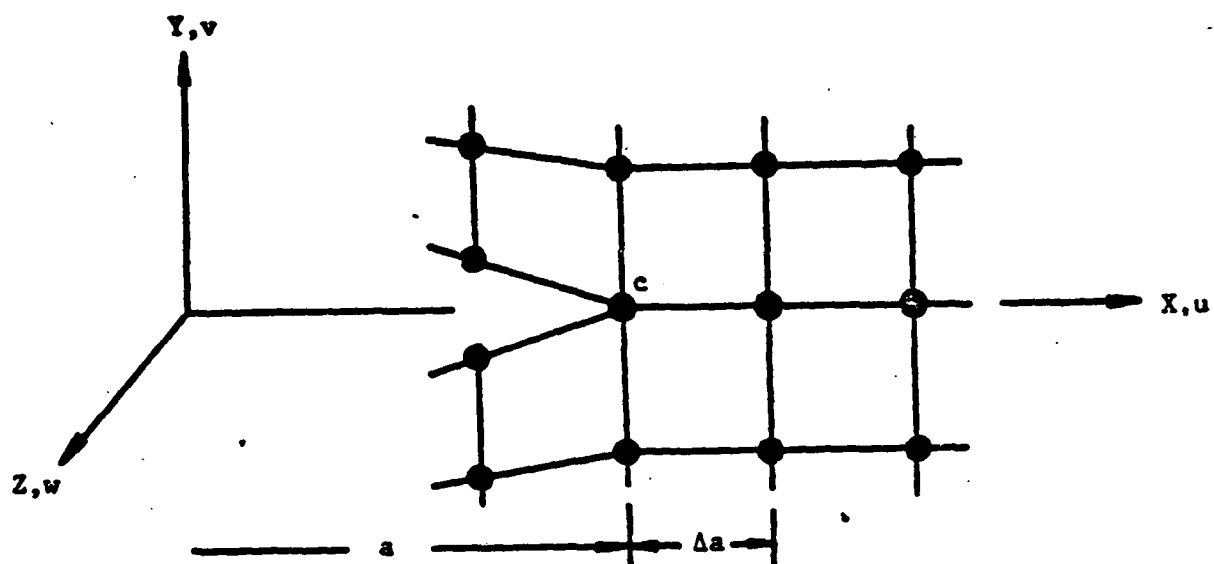
Figure 2.4   Finite Element Mesh at a Crack Tip Illustrating
            the Crack Closure Technique

30

With this new crack geometry taken into account, the finite element solution for the nodal displacements $(u,v,w)_f$ and $(u,v,w)_g$ are found for nodes f and g respectively. The crack extension is then closed by applying equal and opposite forces at nodes f and g such that their common displacements match the displacements found earlier for node c. Of course, these forces are actually the internal nodal forces which existed at node c before it is opened.

The work required to close the crack extension is approximated by

$$\Delta W \approx [F_x(u_f-u_g) + F_y(v_f-v_g) + F_z(w_f-w_g)]/2 \tag{2.21}$$

where F_x, F_y, F_z are the components of the nodal forces required to close nodes f and g together. Thus, the energy release rates for the three crack extension modes are approximated by

$$G_I \sim F_y(v_f-v_g)/2\Delta a$$

$$G_{II} \sim F_x(u_f-u_g)/2\Delta a \tag{2.22}$$

$$G_{III} \sim F_z(w_f-w_g)/2\Delta a$$

The method presented here does not require that the stresses be calculated because the stress and strain fields are approximated by the nodal forces and displacements in the finite element solution. Rybicki and Kanninen [23] applied conventional constant strain finite elements to the solution of three fracture problems: the double cantilever beam specimens; a finite strip containing a central crack; and a bolt fastened double lap joint containing radial cracks. They reported that a relatively coarse grid in the crack tip region was sufficient for a good comparison between their example problems and reference solutions.

31

Nevertheless, the adequacy of this kind of approximation remains a subject of great concern because the mathematical singular nature of the crack-tip is disregarded in the approximation. But, even within the exact definition of $G(a)$ such as by Irwin's integral (2.18), the quantity $\bar{\sigma} \cdot \Delta\bar{u}$ at the crack-tip must be finite (σ is singular, Δu is zero). Thus, the approximation of $G(a)$ in (2.21) is logically acceptable. The only question is the degree of accuracy. The latter is ultimately related to the manner under which the material properties are determined.

In this report, the numerical technique described above is applied to calculate the strain energy release rate as a function of crack length for the transverse cracking and delamination fracture processes in composite laminates. The formulation of the actual finite elements appropriate in these calculations are presented in Section IV. The detials of the fracture initiation and growth criteria, however, will be presented next.

2.4 Initiation and Growth Criteria

In this study, we investigate two types of sub-laminate cracks. Namely, the 90°-cracking and the free edge delamination. In order to set up a crack initiation and growth criterion for each of the two types of cracking, we assume that micro-flaws exist along the fiber-matrix interface, and the ply-to-ply interfaces. These flaws are generally of a size in the order of the fiber diameter, whose crack propagation mechanisms is in the realm of micro-mechanics. Here, we postulate only that these micro-flaws propagate and coalesce into a macroscopic proportion under a certain critical far field loading condition; the initiation process is dynamical at the instance of formation. The size of the crack at the macro-scale depends on the micro-structure of the material (perhaps also on a host of other material processing factors, such as the curing process, post-cure handling, etc). This initial macrocrack

is called here the initial "flaw" whose size is denoted by a_0. The value of a_0 is generally unknown and can be random in nature. It is regarded here, however, as a known macroscopic material property along with other properties such as the stiffness constant, G_c, etc. of the basic material.

As has been discussed previously, both the transverse cracking and free edge delamination processes may be modeled as one-dimensional self-similar crack propagation. Thus, the energy release rate $G(a)$ in each case can be calculated by the numerical finite element technique.

The Griffith criterion of (2.5), when applied to predict the initiation of the sub-laminate cracks, is replaced by the general statement,

$$G(a_0) \geq G_c. \tag{2.23}$$

And, the stability of growth following initiation is governed by the conditions,

$$G(a + \Delta a) < G_c \qquad \text{stable growth} \tag{2.24}$$

$$G(a + \Delta a) > G_c \qquad \text{unstable growth} \tag{2.25}$$

$$G(a + \Delta a) \sim G_c \qquad \text{neutral growth} \tag{2.26}$$

where a $(> a_0)$ is the size of an existing crack for which the growth stability is to be determined. We must note here that the definition of a_0 is in accordance with the original Griffith problem. It is a property of the basic material system.

(a) Transverse Cracking Model

The crack growth geometry for a single transverse crack is illustrated in Fig. 2.5. Under the idealized cracking geometry, as shown in Fig. 2.5(a), assume that the thickness of the 90°-layer $2b > 2a_0$. The crack growth path from the initial size of $2a_0$ is assumed to initiate in the middle of the 90°-layer. The growth geometry is then represented by the finite element model

33

σ_x

90°-Plies

Face-Plies
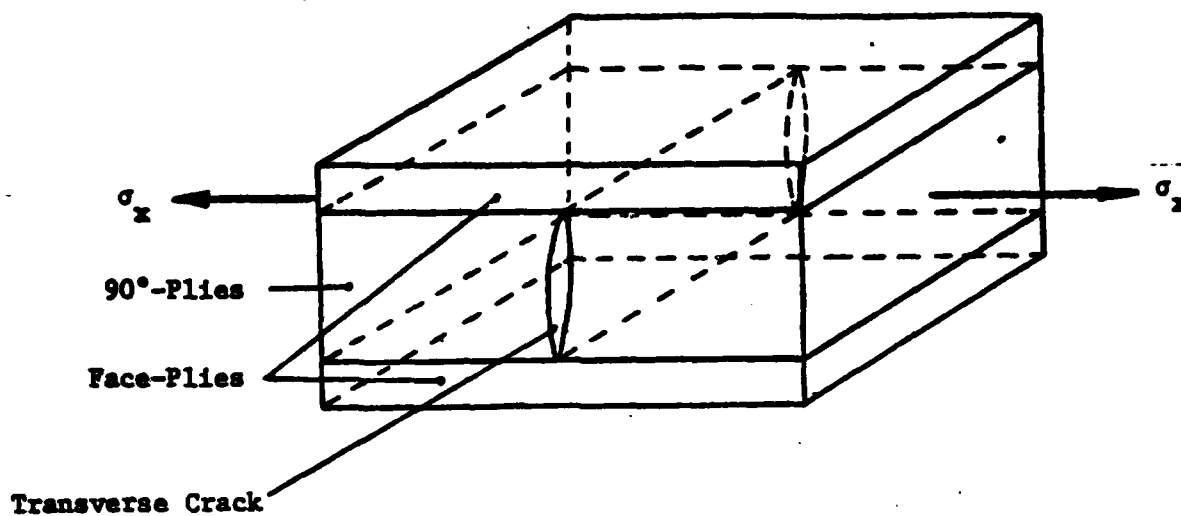
Transverse Crack

(a)   Single Transverse Crack Geometry

z,w

Face Plies

Δa

nt

a

90_n

x,u

L

δ
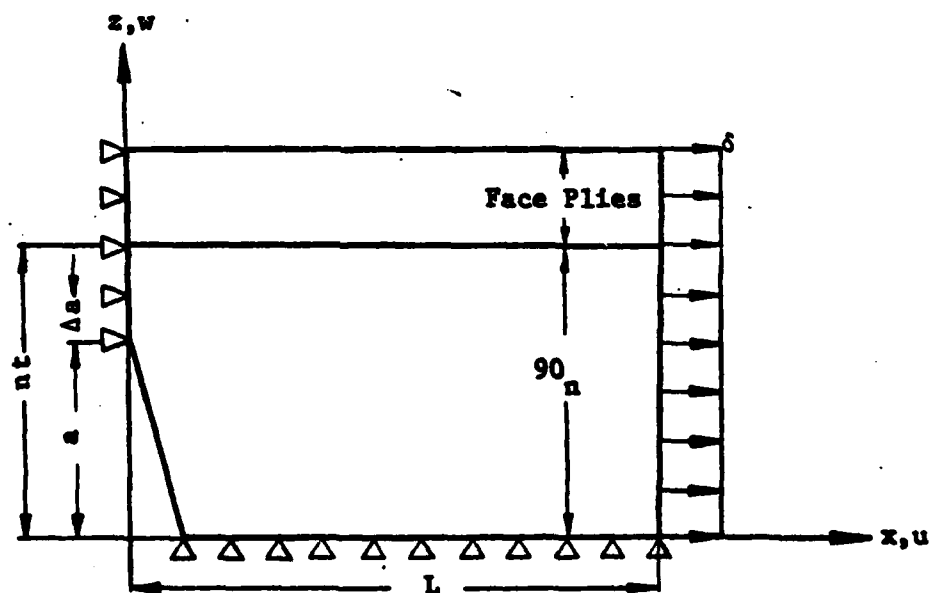
(b) Single Transverse Crack Finite Element Model

Figure 2.5   Cracking Geometry and Finite Element Representation
of a Transverse Crack.

as shown in Fig. 2.5(b). Thus, the solution domain is the 2-dimensional x-z plane, resulting in a generalized plane strain deformation field.

Fig. 2.6 shows a typical finite element mesh for the growth of a transverse crack in the upper half of the laminate. If the laminate is subjected to a uniaxial tension represented by a far field uniform displacement δ, the energy release rate function $G(a)$ may be calculated and expressed by

$$G(a) = [C_e(a)\bar{e}_x^2]t, \qquad (2.27)$$

where t is a characteristic length (e.g., thickness of a ply) and $\bar{e}_x$ is the far field laminate strain induced by δ. The coefficient function $C_e(a)$ is calculated by imposing $\bar{e}_x = 1$. Note that $C_e(a)$ is independent of the loading δ.

Fig. 2.7 shows the general behavior of $C_e(a)$ for the crack in the laminate whose 90°-layer thickness is larger than $2a_0$. Note that the crack size 2a is limited by the thickness of the 90°-layer, 2b. The strain energy release rate increases initially with the increase of cracking size; as the crack approaches the ply interface, the energy release rate begins to decrease; the rate of decrease depends on the relative rigidity of the outside layer. Generally, the maximum of $G(a)$ is located at $a_m < b$.

Similarly, if the laminate is subjected to a uniform temperature drop of Δt, and if tensile stress in the 90°-layer is also induced, then the calculated energy release rate function for the transverse crack is expressed by

$$G(a) = [C_T(a)\Delta T^2]t. \qquad (2.28)$$

35
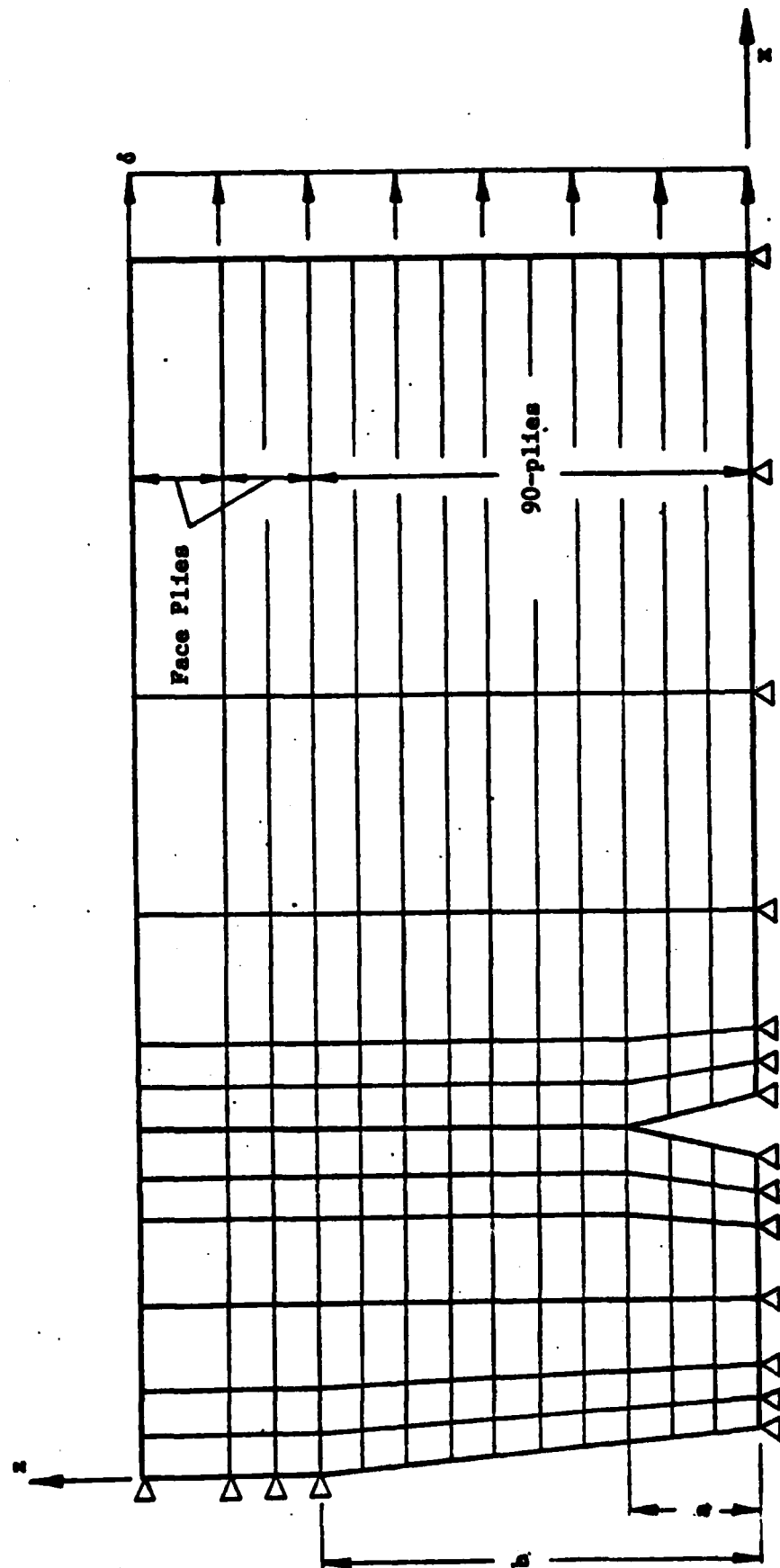
Figure 2.6   Typical Finite Element Mesh for Transverse Cracks.

36

Typical behavior of $C_T(e)$ for a transverse crack is similar to that of $C_e(a)$ as shown in Fig. 2.7. And, $C_T(a)$ has a maximum value also at the same $a_m < b$. The entire $C_T(a)$ curve is generated numerically by imposing $\Delta T = -1$.

In practice, all epoxy-based laminates are subjected to some thermal residual loading when cured. The effects of the residual stresses on transverse cracking can be evaluated by simply assuming a uniform temperature change.

$$\Delta T = T - T_0 \qquad (2.29)$$

where T_0 is usually the curing temperature, or the temperature at which the laminate is free of residual stresses.

Thus, when the laminate is loaded by uniaxial tension, denoted by the far-field strain $\bar{e}_x$, a combined loading condition must be considered. In this case, the total energy release rate $G(a)$ is expressed in the form

$$G(a) = [C_e(a)\bar{e}_x^2 + C_{eT}(a)\bar{e}_x \Delta T + C_T(a)\Delta T^2]t \qquad (2.30)$$

where

$$C_{eT}(a) = 2[C_e(a) \cdot C_T(a)]^{1/2} \qquad (2.31)$$

The growth of transverse cracking is primarily in mode-I, or the opening mode. Accordingly, onset of a transverse crack in the 90°-layer whose 90°-layer thickness is larger than $2a_0$ is defined when

$$G(a_0) = G_{Ic}, \quad \text{if } b > a_0 \qquad (2.32)$$

With the definition (2.32) for crack initiation, Eq. (2.30) becomes a quadratic equation in $\bar{e}_x$, if ΔT is given. The positive root of $\bar{e}_x$ defines the critical applied laminate stress at onset of the crack,

$$(\bar{\sigma}_x)_{cr} = \bar{E}_x(\bar{e}_x)_{cr} \qquad (2.33)$$

where $\bar{E}_x$ is the laminate stiffness in the loading direction.

37
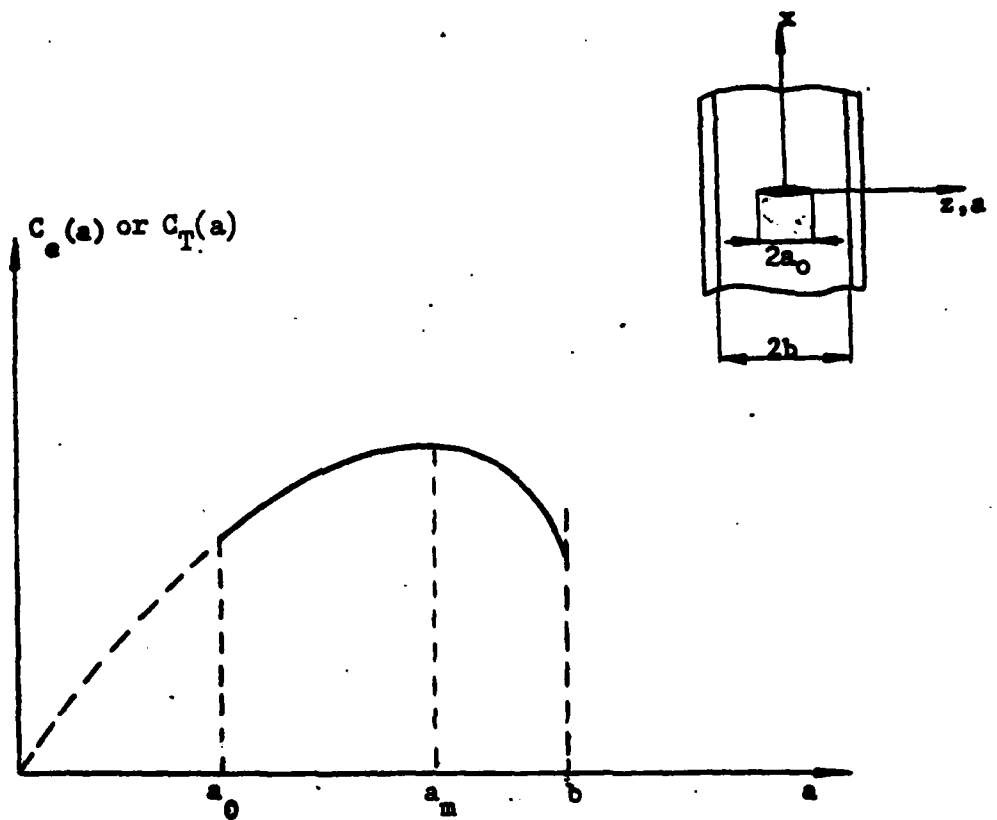
Figure 2.7 Typical $C_e(a)$ and $C_T(a)$ Curve for Transverse Crack

38

Excess Strain Energy Released by
Unstable Crack Propagation

CRACK LENGTH a
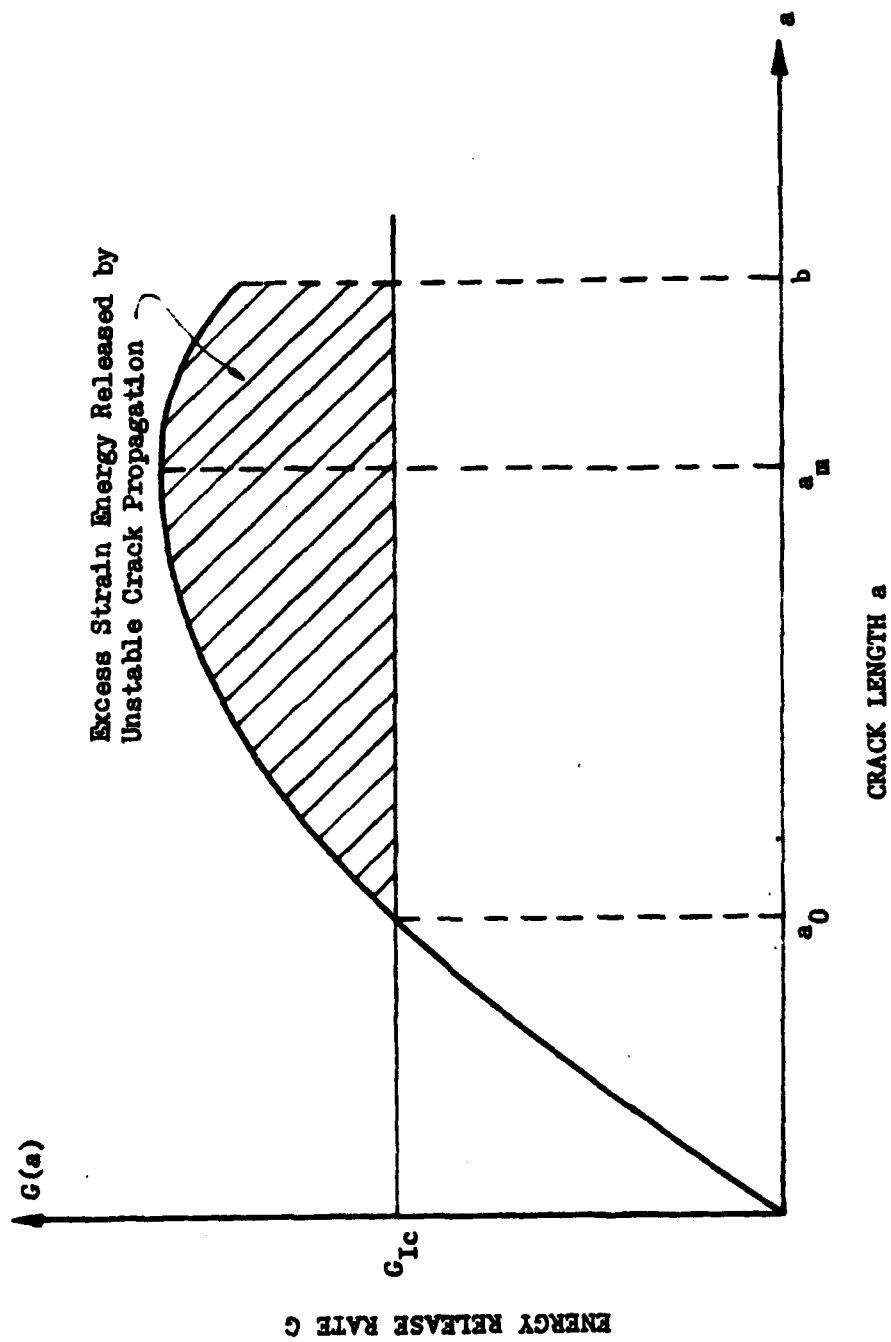
Figure 2.8 Criterion for Onset of a Transverse Crack in 90°-Layer
with Thickness b > a_0.

Fig. 2.8 illustrates the criterion for the onset of transverse crack graphically. It is seen that $G(a_0)$ at the applied laminate stress given by (2.33) has a value equal to G_{Ic}. Once the crack is formed, the available $G(a) > G_{Ic}$ for all $a > a_0$. Hence, the growth is unstable, or is dynamical. The crack is, of course, eventually arrested by the outside constraining layers. During this unstable crack growth, excess energy is released, represented by the shaded area in Fig. 2.8. The effect of the excess energy on the laminate will be discussed later in this report.

In cases where the thickness of the $90°$-layer is small, such as the [0/90/0] laminate, then, b = one-half the $90°$-ply thickness. Since a_0 is a property of the basic material determined within the premise of original Griffith problem, while b can be made arbitrarily small, it is possible that $b < a_0$. In this case, the avilable energy release rate is limited by b, Fig. 2.9. In fact, the maximum available G is at $a = a_m < b$. Hence, the onset of transverse crack is defined by

$$G(a_m) = G_{Ic}, \quad \text{if } b < a_0. \tag{2.34}$$

Eq. (2.34) determines essentially the smallest possible load for a transverse crack.
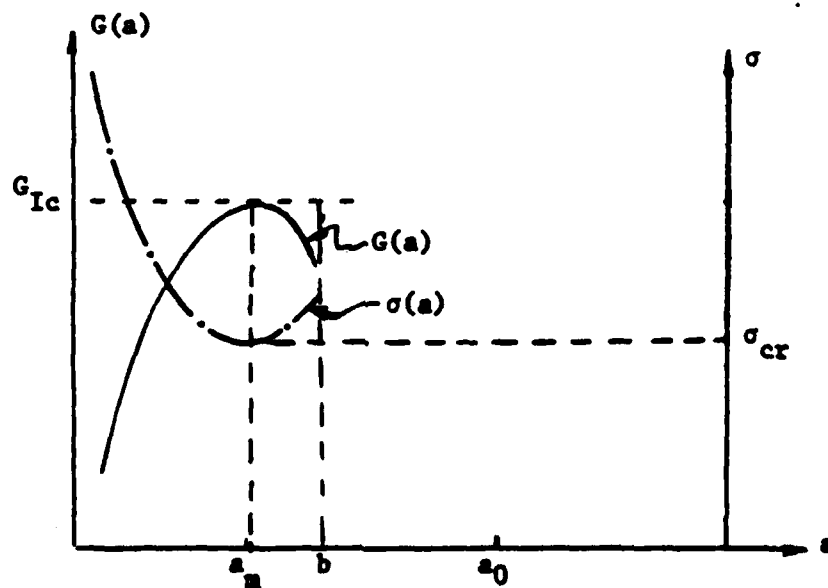
Figure 2.9   Criterion for Onset of a Transverse Crack in $90°$-layer with Thickness $b < a_0$.

It is seen that the crack is started at the size of $a = a_m$; and the growth is stable because the available $G(a) < G_{Ic}$ as a grows larger than a_m. A slightly higher load is then required to propagate the crack to the interface.

The foregoing discussion is concerned with the critical condition under which a transverse crack is formed. If the macroscopic properties of the laminate are ideally uniform throughout, then theoretically, multiple transverse cracks in the 90°-layer will appear simultaneously at a regular spacing. The latter is sometimes referred to as the characteristic spacing [24].

The characteristic spacing of multiple transverse cracks has been explained by the so-called shear-lag [25]. It is simply that an interlaminar shear stress τ_{zx} (refer to coordinates in Fig. 2.5) is developed along the interface where a transverse crack is terminated. This shear stress is highly concentrated near the root of the crack and it decays rapidly at a distance away from the crack root. Fig. 2.10 shows, for example, the shear stress τ_{zx} acting along the
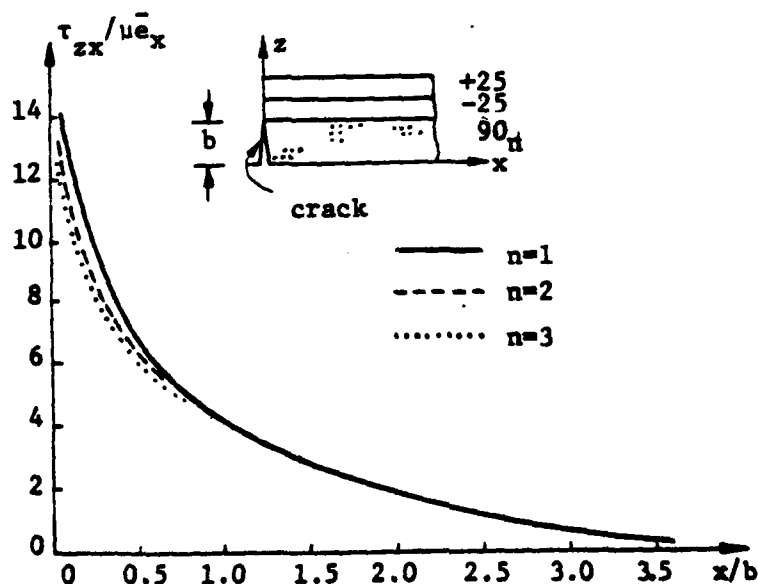
Figure 2.10 Interlaminar Shear Stress on -25/90 Interface. x is measured from the root of the crack.

41

-25/90 interface of a graphite-epoxy $[\pm 25/90_n]_s$, $n = 1,2,3$.

From Fig. 2.10, it is seen that the shear stress is singular at the crack root, and it diminishes completely at a distance of about 4b away from the crack root. As the interlaminar shear stress diminishes, the tensile stress σ_x in the 90°-layer increases; it reaches the far-field value outside the shear-lag zone. A second transverse crack can form only outside this zone. Hence, the so-called characteristic spacing between two neighboring cracks should be equal or greater than the size of the shear-lag zone. In the case of the example illustrated in Fig. 2.10, the characteristic spacing S is 4 times the thickness of the 90°-layer (S = 8b). Or, the characteristic crack density (cracks per unit length) is N = 1/S.

Indeed, if we place the second crack outside the shear-lag zone, see Fig. 2.6, and generate the energy release rate curve G(a), an identical curve will be obtained as that for the first crack. On the other hand, if we place the second crack inside the shear-lag zone, the energy release rate curve would be smaller than that for the first crack [26].

In reality, the idealized multiple cracking process does not occur. Rather, if the first crack forms at some critical far-field load, $\bar{\sigma}_{cr}$, then the second crack would form at a different location (not necessarily at the characteristic spacing) under a slightly higher load, and so forth. Hence, the density of the cracks is generally rising with the applied load, such as illustrated in Fig. 2.11. Moreover, no characteristic crack density can be defined. And, often, the event of multiple crack formation is interrupted by other sub-laminate cracking event at higher load, such as edge delamination, or other interface crackings.

Assuming the formation of each transverse crack is the result of an

42

initial macro-flaw in the 90°-layer, it may thus be appropriate to postulate
that a random distribution of the initial macro-flaw exists in the 90°-layer.
But, this aspect pertains to the statistical nature of material property, not
the mechanism of crack formation. Therefore, we shall defer the subject to a
later study.
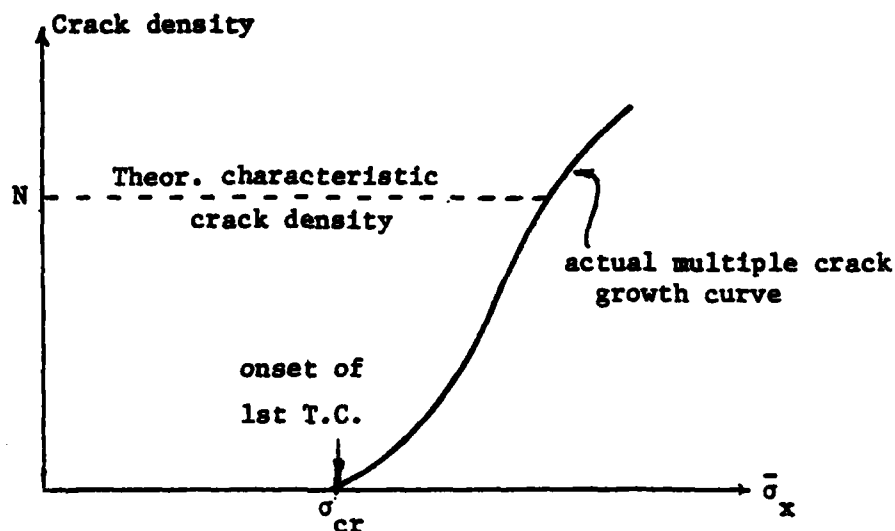
Figure 2.11 Transverse Crack Density vs. Applied Load
N is the Theoretical Characteristic Density

(b) Free Edge Delamination Model

The cracking geometry of free edge delamination in a symmetrical laminate
is illustrated in Figs. 2.12 and 2.13. Fig. 2.12 shows a mid-plane delamina-
tion and the corresponding finite element modeling scheme; and Fig. 2.13
shows a delamination along an interface other than the mid-plane of the lami-
nate. Owing to the symmetry of the laminate, the cracking action in the former
case is essentially of mode I, while in the latter case the crack action is
generally mixed, including modes I, II and III.

43
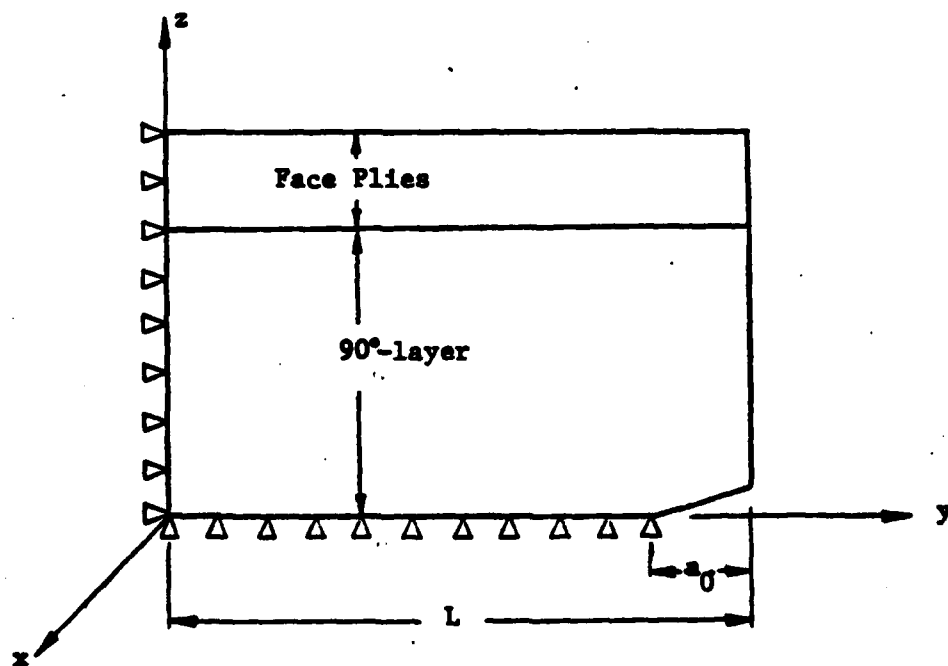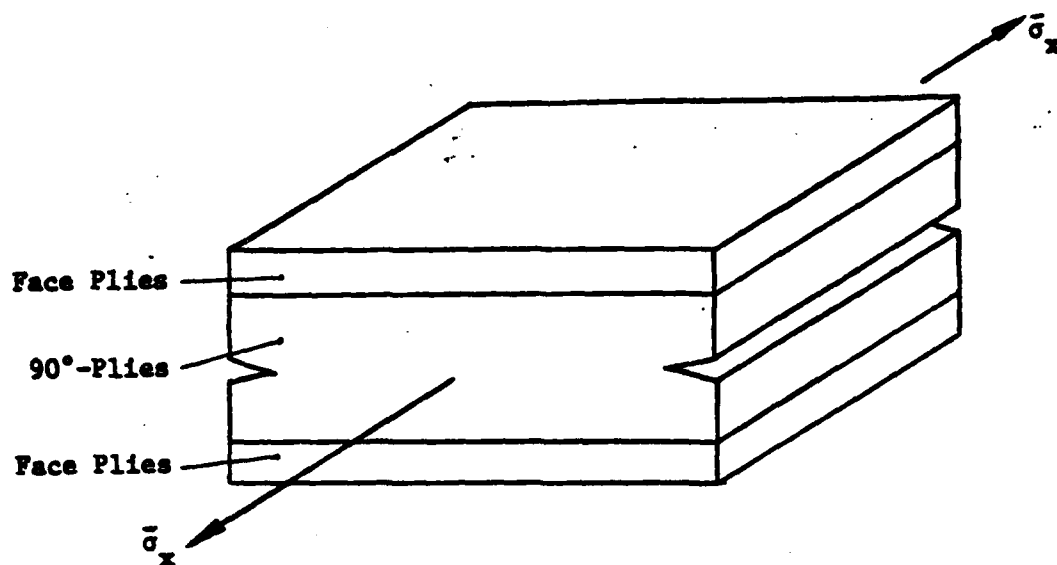
Figure 2.12 Cracking Geometry and Finite Element Representation
of Mid-plane Edge Delamination.
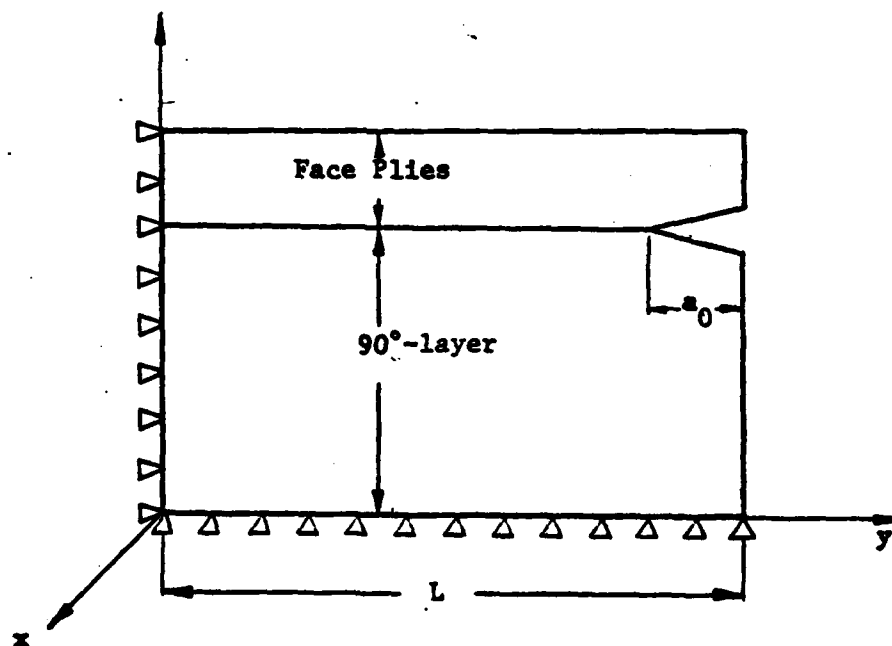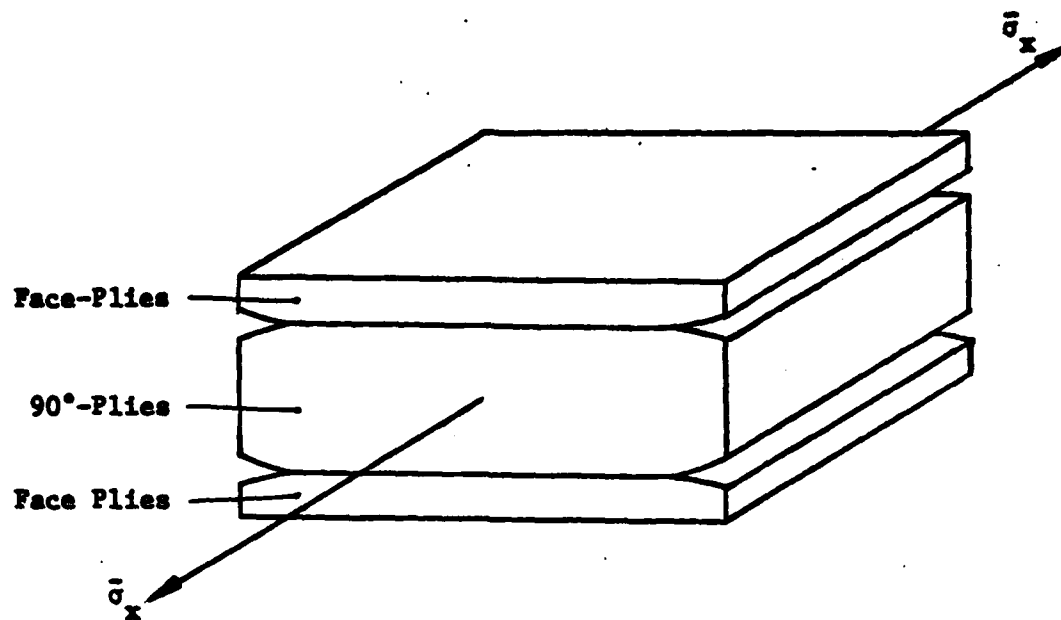
Figure 13 Cracking Geometry and Finite Element Representation
of An Off-mid-plane Interface Delamination.

In both cases, the crack is assumed to form along the prescribed interface, and to propagate in self-similar manner toward the interior of the laminate. Hence, the solution domain is the 2-dimensional y-z plane, being a generalized plane strain deformation field.

Fig. 2.14 shows a typical finite element mesh for the growth model of an edge crack along a given layer interface. It is assumed that an initial macroflaw of size a_0 exists near the free edge and it can be propagated once the applied far-field laminate stress $\bar{\sigma}_x$ reaches a certain critical value.

In order to determine this critical condition, the energy release rate curve G(a) is first generated numerically by the finite element procedure. Since a laminate has more than one interface, it is not generally possible to pin point exactly which interface is going to delaminate under the applied load. Normally, a free edge interlaminar stress analysis is conducted first, before any edge delamination calculation. The details of the interlaminar stress field can provide some indication as to on which one of the interfaces an edge crack is likely to occur. Then, a calculation of G(a) for crack propagation along the selected interface is performed next. In case there are more than one possible interfaces which are likely to delaminate, then the G(a) curves for each of these possible cracks have to be generated.

As has been discussed earlier, mid-plane delamination is primarily of mode I, or opening mode, in a symmetric laminate; while an off-mid-plane delamination is generally a mixed-mode crack. Between the two different modes of delamination, the crack growth criteria may also be different. Depending on the microscopic details of the cracking surfaces, the critical energy release rates G_c for mid-plane cracking and for off-mid-plane cracking may actually be
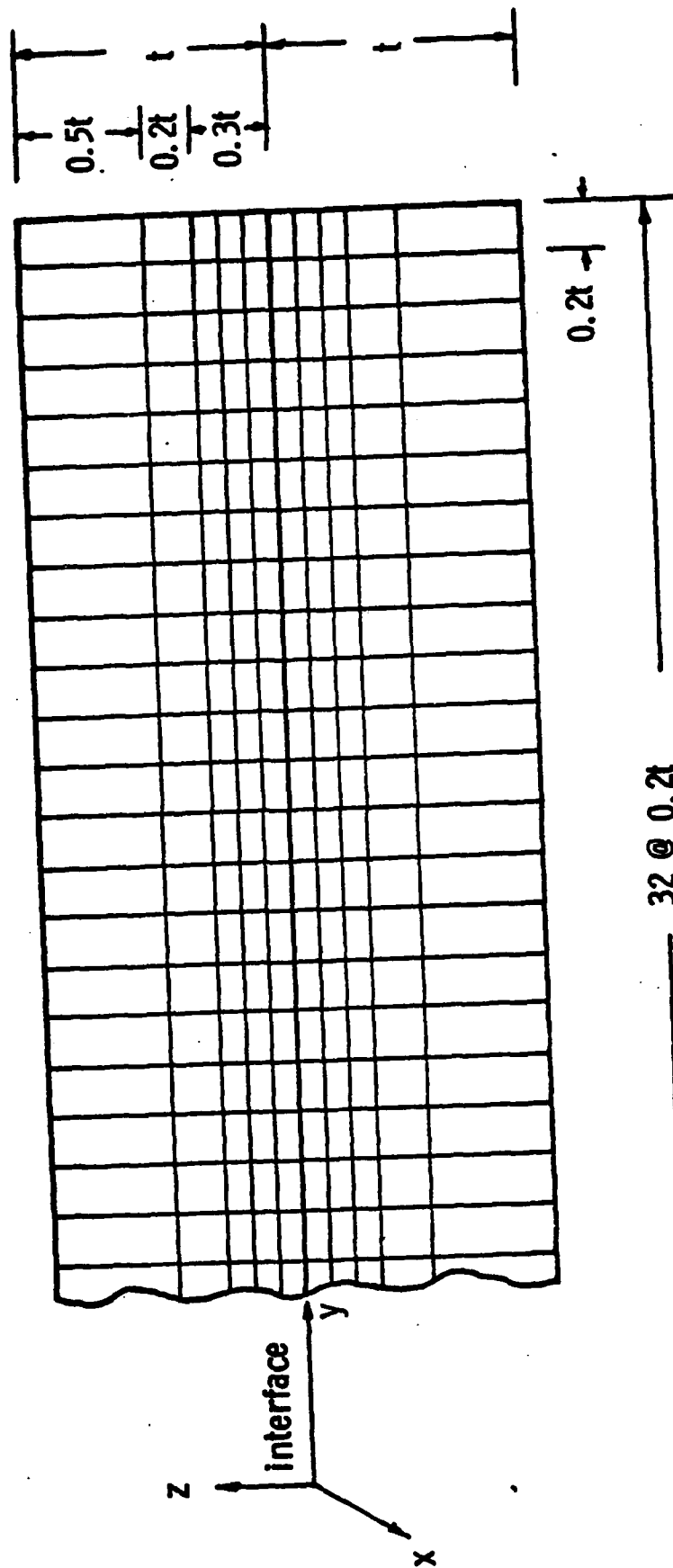
Figure 2.14 Typical Finite Element Mesh for Free Edge Delamination

distinct.   And this has been shown experimentally for some unidirectional

graphite-epoxy [13].   Hence, a trial calculation is usually required to

determine just which interface is the most energetically possible for an edge

delamination.

Fig. 2.15 shows a typical G(a) curve for a delamination growth along

either the mid-plane, or an interface other than the mid-plane. The general

behavior of G(a) is that it will increase rapidly to reach a maximum value

at $a = a_m$. After this point, the value of G becomes essentially a constant,

independent of the crack size a (assuming the width of the laminate is large
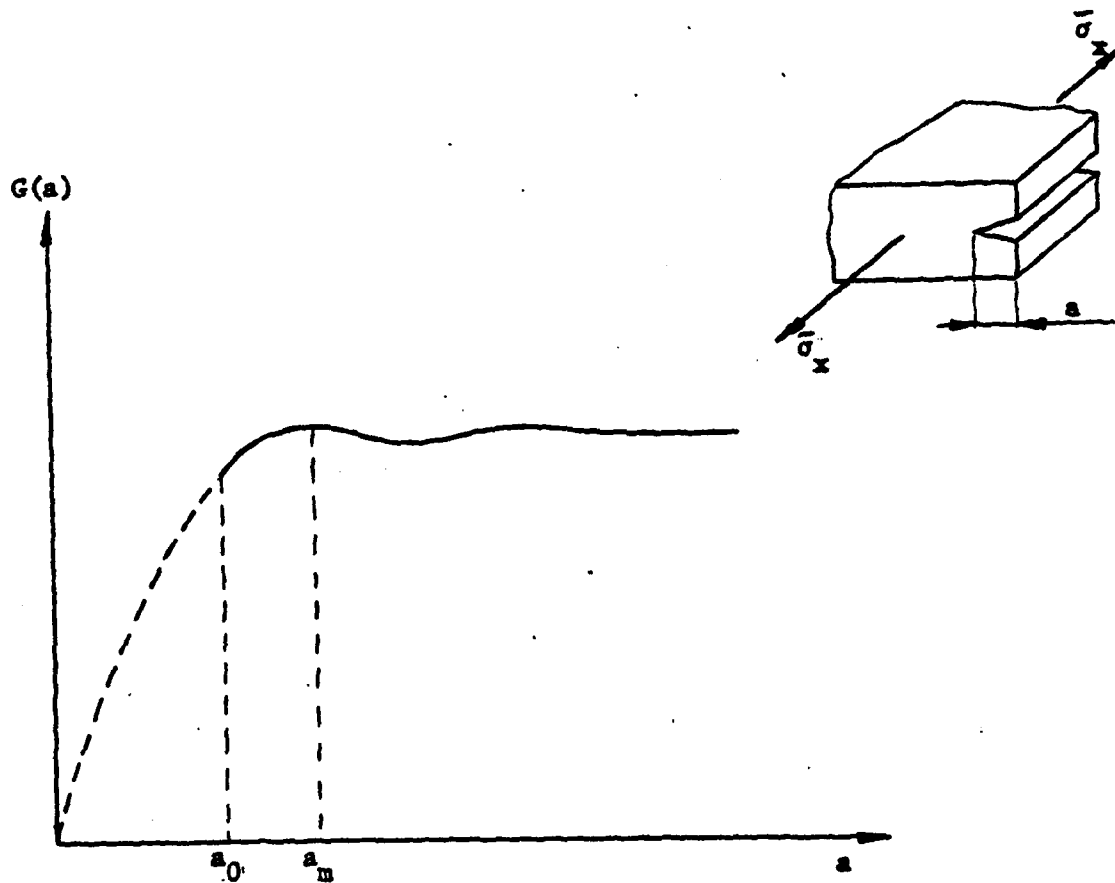
Figure 2.15   Typical G(a) for Edge Delamination.

compared to the crack size a). The value of a_m at which G attains its maximum, depends on a number of geometrical factors. The most notable factor is the layer thickness of the two adjacent layers on whose interface the delamination propagates. For example, if G(a) represents the total energy release rate curve for a mid-plane delamination for the laminates $[\pm 45_n/0_n/90_n]_s$, n = 1,2,3, then the maximum of G would occur at about $a_m = nt$, t being the thickness of one ply. Since G increases with a before $a \to a_m$, the available maximum G in the case of n = 1, for instance, is much smaller than the available maximum G in the case of n = 2.

This thickness dependence nature of G_{max} on layer thickness is not exactly the same as the previously discussed transverse cracking problems. But, the reason for the existance of a maximum is also due to the constraining effect from the layer structure of the laminate.

As in the transverse cracking problems, G(a) curve of an edge delamination growth can also be expressed in terms of the applied thermal and mechanical loads:

$$G(a) = [C_e(a)\bar{e}_x{}^2 + C_{eT}\bar{e}_x \Delta T + C_T(a)\Delta T^2]t \qquad (2.35)$$

where the coefficient functions C_e, C_T and C_{eT} are defined identically as those expressed in Eqs. (2.27), (2.28) and (2.31), respectively.

If the computed G(a) is for a mid-plane delamination growth, then the onset of delamination is defined when

$$G(a_0) = G_{Ic}, \quad \text{if} \quad a_0 < a_m \qquad (2.36)$$

or

$$G(a_m) = G_{Ic}, \quad \text{if} \quad a_0 > a_m. \qquad (2.37)$$

49

The physical reason for the difference between (2.36) and (2.37) is the same as in the transverse cracking problems discussed earlier.

If the computed G(a) is for an off-mid-plane delamination growth, then G(a) so computed is consisted of three modal parts, as is expressed generally in Eq. (2.20). A general criterion for the onset of such a mixed-mode crack can thus be similarly given as

$$G(a_0) = G_{(I,II,III)c}, \quad \text{if } a_0 < a_m \qquad (2.38)$$

or

$$G(a_m) = G_{(I,II,III)c}, \quad \text{if } a_0 > a_m \qquad (2.39)$$

In actual problems, experiment is required to decide whether or not G_{Ic} is equal to $G_{(I,II,III)c}$; or whether or not $G_{(I,II,III)c}$ depends on the ratios of G_I/G_{II} and G_I/G_{III}, etc.

Whichever final growth criterion is used, the growth stability of delamination is theoretically stable if $a_0 < a_m$; and it is neutral if $a_0 > a_m$. In reality, however, the growth is generally stable. This is because (1) the interface flaw size a_0 is not uniform along the specimen; the weakest location always starts delamination first; and (2) the actual width of the specimen is finite, say 1 inch wide; as the delamination growth becomes larger relative to the width, the structural stiffness of the specimen is reduced; and so is the available energy release rate G under the same load.

This last aspect on growth stability will be discussed again in Sections III and IV where we shall examine the relevant experimental results as they are correlated with their computed counterparts.

III. EXPERIMENTAL STUDY

3.1 Scope of Experiment

The main objective of the experiment is to conduct an extensive case-study, which will complement the development of the analytical fracture models. As has been discussed in the previous section, there are several physical and conceptual questions that must be resolved by experiment if the methods of classical fracture mechanics are to be used in the fracture analysis of sub-laminate failures. Thus, the experimental study will provide not only physical insights in model   development, but also guidance for an effective numerical computation. The experiment identifies the important material and geometrical parameters which influences the various fracture processes.

Accordingly, the experimental study consisted of the following major tasks:

(a) **Basic Material Characterization.** Since all the laminates tested were made by laminating unidirectional plies, the basic ply properties were characterized within the frame work of "ply elasticity," or the macroscopic "effective" moduli approach. Both the elastic compliances and the strength properties were determined by experiments.

In addition to the unidirectional ply properties, some basic laminates were also tested. Among them included $[0_8]$, $[90_8]$, $[\pm 25]_{2s}$, $[\pm 45_2]_s$ and $[\pm 45_3]_s$. These were tested for their laminate tensile modulus (E_x) and their laminate tensile strength (σ_u) only. No attempt was made to examine their failure mechanisms.

The proper values for the residual-stress-free temperature, T_0, has also been investigated experimentally.

51

These basic material data are required as input information in the numerical simulation of fracture growth.

(b) <u>Transverse Cracks in $[0/90_n/0]$ - Family</u>. This series of tests included laminates in the form $[0/90_n/0]$, n = 1,2,3,4 and $[0_2/90_{2n}/0_2]$, n = 1,2. Because of the relatively small edge normal stress σ_z, these laminate do not suffer edge delamination under uniaxial tension. Rather, only transverse cracks in the 90°-layer can be induced. Hence, this series of tests provides an ideal case study for the transverse cracking model developed earlier in Section II.

In addition, laminates of the form $[0_2/90_4/0_2]$ were tested under different temperature environments.

(c) <u>Transverse Cracks and Delaminations in $[\pm 25/90_n]_s$ - Family</u>. This series of tests included laminates in the form $[\pm 25/90_n]_s$, n = 1/2, 1,2, 3,4,6,8. The reason for selecting the ±25°-layer as the major load-carrying element is that it offers the optimal lamina constraint which induces free-edge delamination under uniaxial tension. Indeed, as will be shown by the experimental results, the laminates of n = 1/2 and 1 suffered free edge delamination without any transverse cracking; and, the delamination mode was primarily of mode-I. This, then provides an ideal case study for the delamination modeling. As for those laminates with n > 1, both transverse cracking and edge delamination were induced, resulting in complicated interacting effects. In particular, for cases of n > 3, other modes of fracture became predominant. Thus, this series of tests presented a multitude of interesting fracture growth processes.

In addition to the $[\pm 25/90_n]_s$ series, laminates of $[\pm 25_2/90_2]_s$ were also tested. This is to check whether or not the ultimate strength of the load carrying layer (the $\pm 25_2^\circ$-layer) would be affected by the layer-thickness effect. This can be accomplished by comparing it to the $[\pm 25/90]_s$ laminate, whose load-carrying ± 25-layer has only half the thickness.

(d) <u>Mixed Mode Fracture in Notched $[\theta_8]$ - Family</u>. A series of tests was conducted in $[\theta_8]$, $\theta = 0°$, $15°$, $30°$, $45°$, $60°$, $75°$ and $90°$. In each case the specimen had double side notches of 0.15" size. Under uniaxial tension, fracture failure was induced along the fiber direction. The fracture is of mixed-mode in general, and the ratio between mode-I and mode-II depends on the value of θ. Results of this test has provided some insights about the material resistance under various degrees of mixed-mode fracture.

3.2 Experimental Procedures

Throughout this study, all laminates tested were fabricated from Fiberite T300/934 prepreg tape. They were autoclave cured at 350°F (450°K) according to the manufacturer's specifications. Nominal fiber volume was determined in the range of $66 \pm 2\%$. The 12"x12" laminated panels were cut by diamond saw to a coupon length of 9" and width of 1". Fiberglass tabs of length 1.5" were bonded to each end of the coupon. Coupons were stored under normal room conditions (70~80°F and $60 \pm 5\%$ relative humidity) for a typical duration of 3 to 6 months before test.

All tests were conducted on an Instron Universal Tester under normal room conditions (except otherwise stated). Load was applied at a displacement-control rate of 0.01" per minute.

53

The experimental procedure for documenting damage sequence in the various laminates was as follows:

(1) The ultimate tensile strength (UTS) for each laminate in the series was determined by a minimum of four ramp tensile tests. These specimens were strain gaged to determine the tensile stiffness properties, including the laminate's Young's modulus and Poisson ratios.

(2) For each laminate type, a minimum of four specimens were step-loaded under axial tension. The initial step loading increment was approximately 10% UTS until damage in the form of transverse cracks and/or delamination was detected. Then the load increment was subsequently reduced to approximately 5% UTS until the ultimate laminate failure.

(3) After each step loading, the specimen was removed from the testing machine and was inspected for damage by means of DIB (di-iodobutane) enhanced x-radiography.

(4) In addition to x-ray examination, the free edges of each specimen were also optically examined using a microscope to observe the details of the damaged area.

(5) In many cases, tested specimens were selectively sectioned, polished and examined under SEM (Scanning Electronic Microscope). The SEM examination provides additional internal cracking details in the thickness sectional view of the laminates.

Figure 3.1 illustrates a typical x-ray sequence taken during the incremental testing process for a $[\pm 25/90_3]_s$ specimen. Here, the load-damage relationship of the specimen can be studied in detail by examining the series of x-radiographs. In this case, damage of any form was not detected up to

54

55% UTS   64% UTS   74% UTS   81% UTS   87% UTS

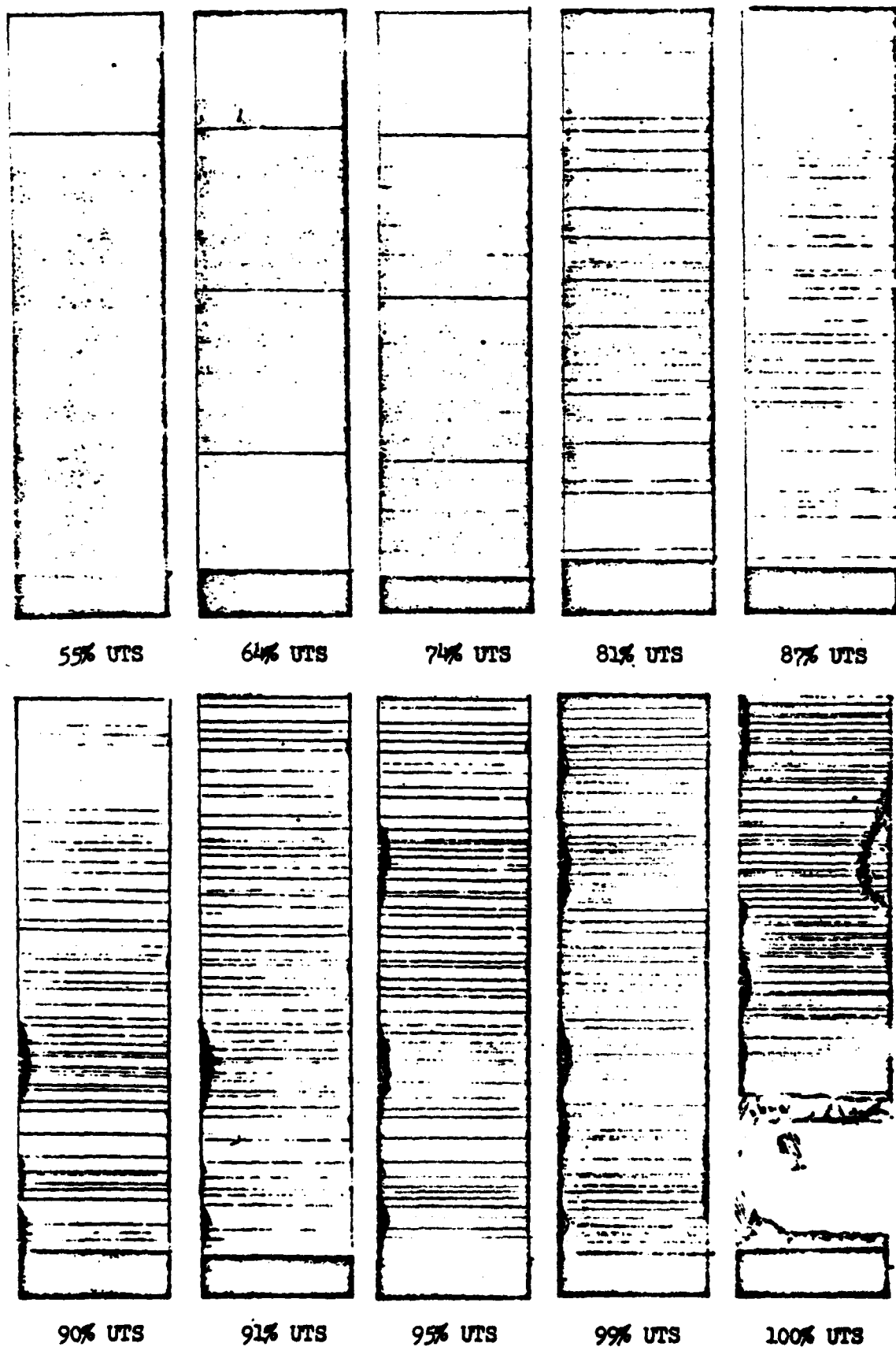90% UTS   91% UTS   95% UTS   99% UTS   100% UTS

Figure 3.1 X-radiographs Showing Transverse Cracking and Edge Delamination Growth Sequence Under Step-load For A $[\pm 25/90_3]_s$ Specimen.

a load of 50% the ultimate tensile strength (UTS). The first sign of damage was a transverse crack which appeared at 55% UTS, identified by the thin dark line perpendicular to the load direction in the x-ray picture. More cracks were seen to appear in the next several load increments.

At the load of 88% UTS, the first sign of edge delamination appeared in the form of a thumbnail shaped crack at the left side of the specimen. The area of delamination extended stably as the applied load was increased. From the x-ray pictures, it is seen that a higher density of transverse cracks exists in the delaminated area. And, by comparing the pictures at 99% UTS and 100% UTS, it is evident that the final failure was quite sudden and it did not seem to involve extensive delamination in this particular sample (the reason for this growth behavior will be explained later in this section).

Optical edge-view examination of the delaminated specimen showed that the delamination crack in this case followed primarily the -25°/90° interface.

Fig. 3.2 shows another sequence of x-radiographs (enlarged) taken for a $[\pm 25/90]_s$ specimen. It is seen here that edge delamination grew much more extensively before final failure. Furthermore, in this case, no transverse cracks were detected before delamination. And, when they appeared, they existed only in the delaminated area. The delamination crack was observed to zig-zag within the 90°-layer in an edge-view optical examination.

From the load-sequence x-ray pictures, either the transverse crack density or the percent of delamination may be plotted as a function of the applied load. For example, a relationship between the transverse crack density (number of transverse cracks per unit length, N) and the applied load σ can be obtained from the x-ray sequence shown in Figure 3.1. This relation is shown graphically in Figure 3.3. The load required to initiate transverse
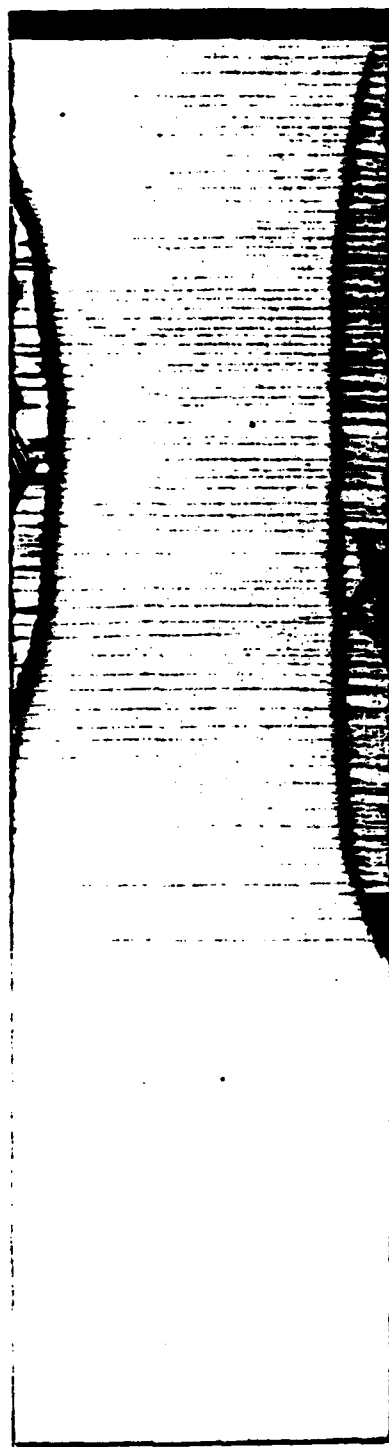
(a)   (b)

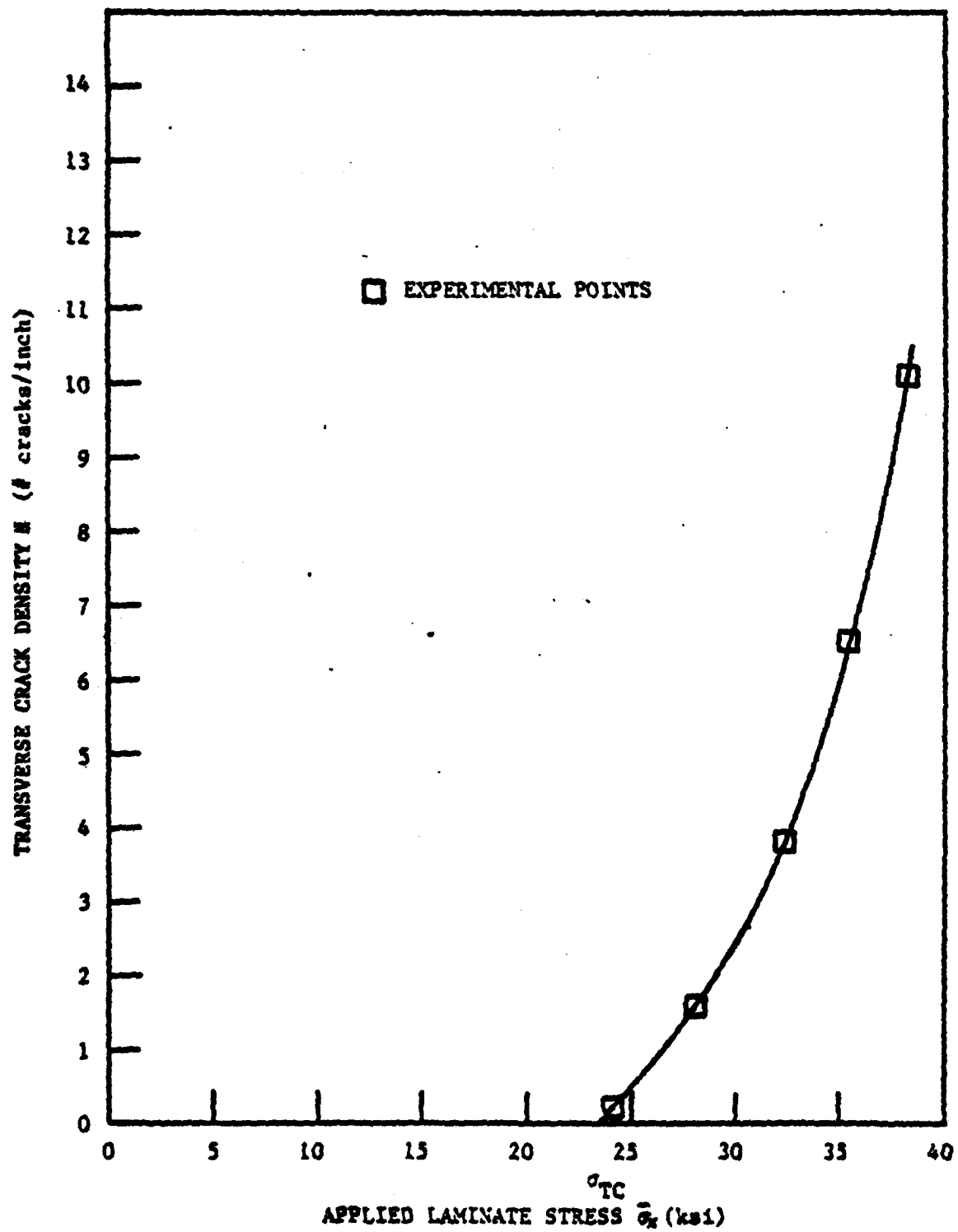Figure 3.2 X-radiographs of A $[\pm 25/90]_s$ Specimen Taken at (a) 96% UTS and (b) 100% UTS.

Figure 3.3.   Transverse Crack Density vs. Applied Tensile Stress
for a $[\pm 25/90_3]_s$ Specimen.

58

cracking σ_{TC} is determined by the σ-intercept of the curve as shown in the figure. As previously discussed, at the onset of free-edge delamination a higher density of transverse cracks is observed in the delaminated region of the laminate. This indicates that there is a certain interaction between the two cracking events. Thus, the measurement of the N-σ relationship is terminated at the onset of edge delamination.

The area of free-edge delamination can also be related to the applied load from these experimental results. The onset load for free-edge delamination may then be obtained in a manner similar to the method that determines the onset load for transverse-cracking as described above.

As has been mentioned earlier, a number of specimens were also sectioned for SEM examination. Typical transverse cracks in the 90°-layer can be seen in a thickness sectional view, such as shown in Fig. 1.3. Similarly, edge sectional view of the laminate gives the internal details of the edge crack, such as shown in Fig. 1.5.

3.3 Experimental Results.

For all the results reported in this section, each represents the averaged values from three or four (sometimes more than four) replicate specimens. Generally, data scatter is in the 5% (standard deviation) range for the compliance properties, 10% range for the strength properties. In this section, the statistical nature of the data scatter will not be discussed. However, whenever appropriate, the range of the data scatter will be indicated. Otherwise, only the averaged value will be used.

(a) Basic Ply and Laminate Properties

For the T300/934 graphite-epoxy composite material used in this study, a routine material property characterization test was conducted. Some

59

details of the characterization test are found in Ref. [9]. We shall mention
only that the unidirectional fiber reinforced system was considered macro-
scopically a homogeneous medium which possesses a monoclinic symmetry in its
principal material coordinates (L.T.z) [27]. The engineering stiffness con-
stants determined using 8-ply laminates and tested under nominal room con-
ditions are as follows:

$$
\begin{array}{lll}
E_L = 21.0 \text{ Msi} & E_T = 1.70 \text{ Msi} & E_Z = 1.70 \text{ Msi} \\
\nu_{LT} = 0.3 & \nu_{TZ} = 0.54 & \nu_{LZ} = 0.3 \\
G_{LT} = 0.94 \text{ Msi} & G_{TZ} = 0.5 \text{ Msi} & G_{LZ} = 0.94 \text{ Msi} \\
\alpha_L = 0.2 \text{ } \mu e/°F & \alpha_T = 16 \text{ } \mu e/°F & \alpha_Z = 16 \text{ } \mu e/°F
\end{array}
\tag{3.1}
$$

Each material ply when cured in a laminate has a nominal thickness,

$$
t = 0.0052" \ (0.0132 \text{ cm}) \tag{3.2}
$$

The strength property of the unidirectional system is given in Table
3.1. Since both the longitudinal and the transverse stress-strain relations
(under uniaxial tension and room conditions) are essentially linear, except
near failure, it is sometimes more convenient to use the ultimate strain e_u
to characterize the strength of the material. Note, however, that the
physically measured quantity is always the far field applied load; the term
ultimate strength σ_u or ultimate strain e_u ($= \sigma_u/E_x$) represents only an average
over the gross dimension of the test specimen.

Table 3.1 Test Data of Some Basic Laminates

Laminate	E_x, msi	σ_u, ksi	e_u, %
$[0_8]$	21.0(20 - 23.5)	250(231 - 270)	1.1(1.0 - 1.15)
$[90_8]$	1.70 (1.65 - 1.77)	6.4(6.0 - 7.0)	0.39(0.34 - 0.44)
$[\pm 25]_{2s}$	11.1(11 - 11.15)	75(70 - 78)	0.67(0.66 - 0.68)
$[\pm 45_2]_s$	3.3(3.26 - 3.41)	20(18.6 - 22)	0.61(0.56 - 0.67)
$[\pm 45_3]_s$	3.15(3.04 - 3.27)	18.1(17.5 - 19.5)	0.57(0.55 - 0.62)

Results from testing the $[\pm 25]_{2s}$, $[\pm 45_2]_s$ and $[\pm 45_3]_s$ laminates are also summarized in Table 3.1.

The longitudinal stress-strain relation of the $[\pm 25]_{2s}$ specimen maintained a perfect linearity up to failure. The specimen was severed in the mid-section of the specimen, involving predominantly fiber breakage, Fig. 3.4. It should be noted that the stacking sequence of the $[\pm 25]_{2s}$ specimen is actually $[25/-25/-25/25]_s$. It is to be distinguished from, say $[\pm 25_2]_s$ which is actually $[25_2/-25_2]_s$.   The failure behavior between the two can be drastically different.

The reason for the difference in the failure mechanisms of the $[\pm 25]_{2s}$ and $[\pm 25_2]_s$ laminates is due to the layer-thickness effect. This same effect is illustrated more vividly   by the strength results of the $[\pm 45_2]_s$ and the
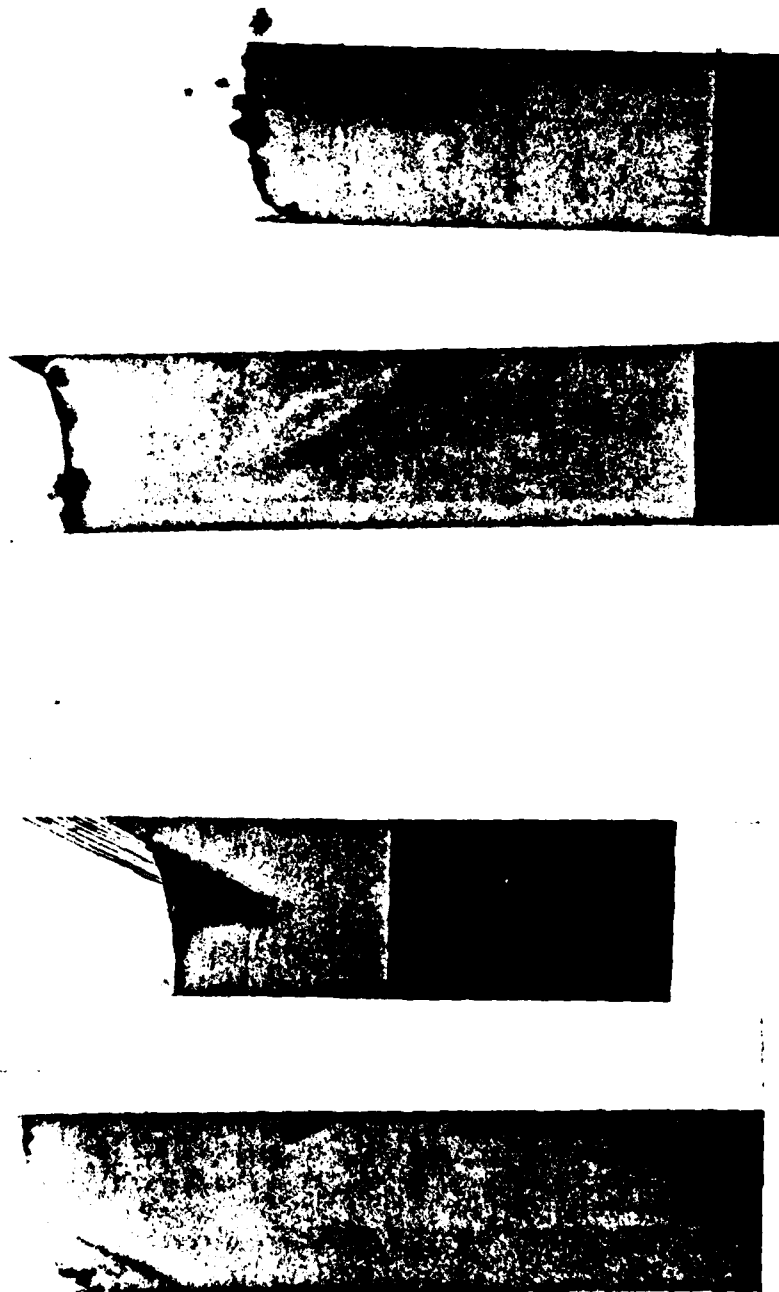
Figure 3.4 Failure Mode of Two $[\pm 25]_{2s}$ Specimens under Uniaxial Tension.

62

$[\pm45_3]_s$ laminates, see Table 3.1. It is noted that the average strength of the former is 20 ksi while the average strength of the latter is only 18 ksi, a reduction of 10% because of an increase in material layer thickness.

A closer examination of the failure process of the previous two laminates indicates that failure modes in both cases involved primarily matrix cracking, not fiber breakage. Fig. 3.5 shows the x-radiographs of a $[\pm45_3]_s$ laminate which is loaded near final failure. At about 98% UTS, a single surface 45°-crack is induced, Fig. 3.5(a), which is almost immediately followed by multiple -45°-cracks in the inner -45°-layer, Fig. 3.5(b). It may thus be concluded that the formation of the first major 45°-crack initiated the process of failure of the laminate. Clearly, the formation of the 45°-crack must be a fracture phenomenon, which depends, to some extent, on the thickness of the layer in which the crack is formed.

The final failure mechanisms in these basic laminates, however, will be investigated in a future study. They are outside the scope of the present report.

Finally, experiments on the residual-stress-free temperature yielded a value of T_0 ranging from 300°-325°F. In this experiment, an unsymmetric $[0_4/90_4]$ laminate was used. When cured at 350°F, the laminate configuration was flat. After cooling down to room temperature, the laminate curved into an arc as shown in Fig. 3.6. Thus, upon re-heating the laminate at a higher temperature, the curvature of the specimen decreases. By optically measuring the laminate cord height, h, at various test temperature, it is then

63
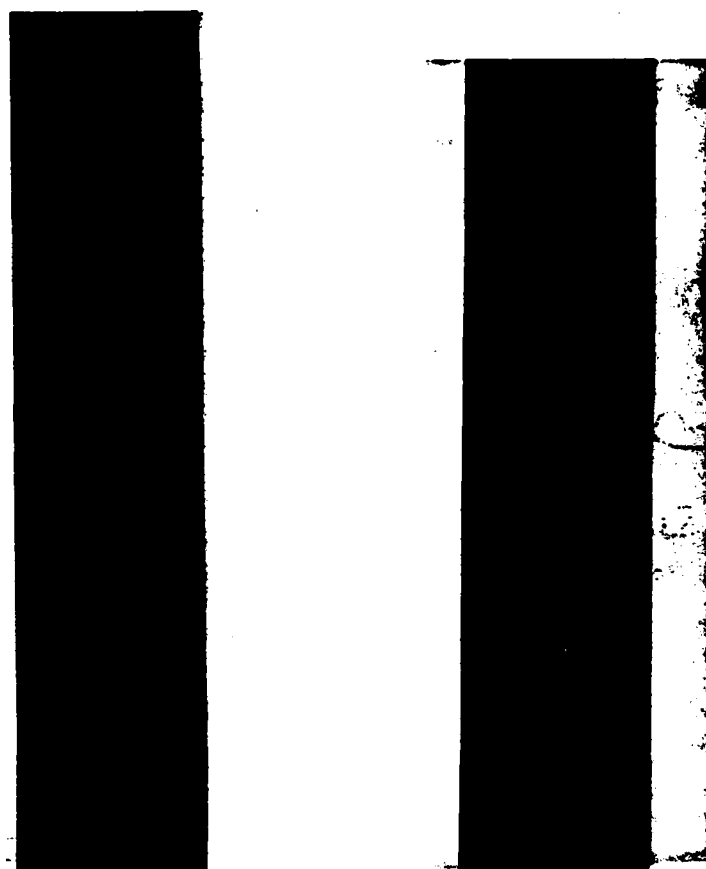
(a)   (b)

Figure 3.5 Failure Mode of a $[\pm 45_3]_s$ Specimen, (a) A Major
45°-Crack Formed at 98% UTS, (b) Multiple -45°-
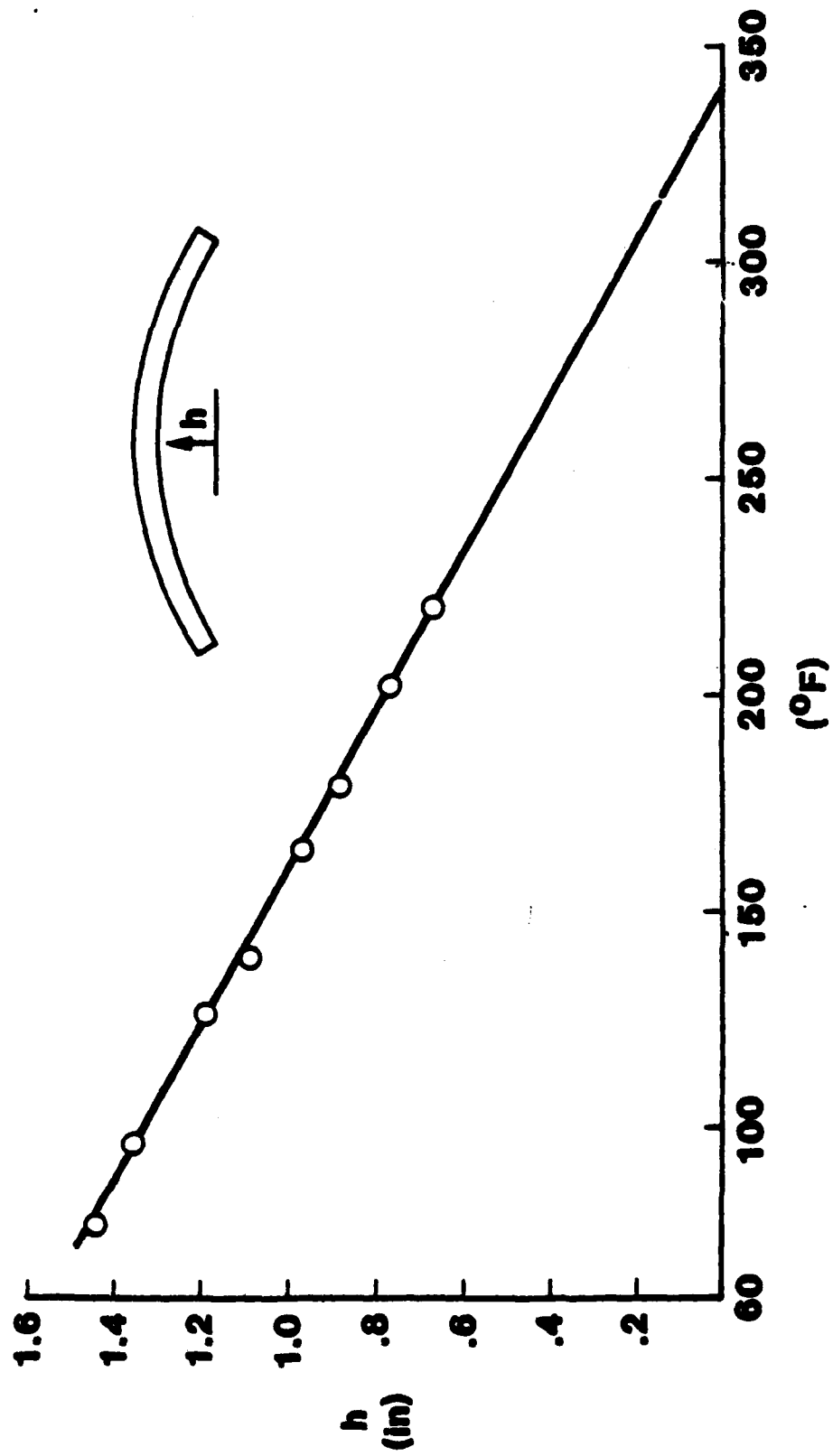Cracks Formed at 99% UTS.

Figure 3.6 Measured Cord Height h vs. Temperature in $[0_4/90_4]$ Laminates.

65

possible to determine experimentally the residual-stress-free temperature T_0.
Fig. 3.5 shows the measured cord height h versus temperature; the test was
conducted for a specimen immediately after curing. It is seen that a loss
of about $10°F$ is resulted due to some initial stress relaxation. Upon storage
in room conditions for 3-6 months, further relaxation due to time and moisture
absorption was encountered. This caused an additional decrease in the stress-
free temperature. For simplicity, and without causing significant discrepancy,
the stress-free temperature T_0 for all laminates tested in this report is
approximated by a constant value of,

$$T_0 = 300°F \qquad (3.3)$$

(b) Crack Growth in the $[0/90_n/0]$ - Family   In this family, the laminates
$[0/90_n/0]$, n = 1.2.3.4 and the laminates $[0_2/90_{2n}/0_2]$, n = 1,2 were tested
under room conditions. All, except the $[0/90/0]$ laminates, showed transverse
cracks under the uniaxial tensile load. In the case of the $[0/90/0]$ specimens,
no transverse cracking was observed until the specimens were severed at final
failure. Table 3.2 summarizes the test results, including the stiffness E_x,
onset stress for transverse cracking and the final failure stress of the
various laminates.

Plots of transverse crack density N versus the applied load σ were ob-
tained from the load-sequence x-radiographs of all specimens, except those of
$[0/90/0]$ lamination. These plots are shown in Fig. 3.7. It is seen that for
the cases of n = 2 and 3, N increases monotonically with σ until final failure;
there is no evidence of the existence of the so-called "characteristic" spacing
discussed earlier in Sections I and II. However, for the case of n = 4, a
slight leveling off of N is indicated. But, for this case, the theoretical

66

characteristic spacing is $S \sim 16\,t$, and the corresponding characteristic crack density would be $N = 1/S \sim 12$. From Fig. 3.7, the leveling off crack density is more than 25.

Table 3.2 Test Results of the $[0/90_n/0]$-Family

Laminate	E_x, msi	T.C. onset stress, ksi	Final failure stress, ksi
$[0/90/0]$	13.9	No visible cracks	144(126-158)
$[0/90_2/0]$	11.3	68(59.0-70.5)	108(85-122)
$[0/90_3/0]$	8.9	48(44-53)	86(84-88)
$[0/90_4/0]$	7.9	41(34-44)	76(73.5-80.5)
$[0_2/90_2/0_2]$	13.8	85(76-98)	162(140-180)
$[0_2/90_4/0_2]$	11.1	50(42-57)	114(106-117)

The results listed in Table 3.2 are graphically displayed in Fig. 3.8, and Fig. 3.9. In particular, compare the results shown in Fig. 3.9, and note the different transverse crack onset load between $[0/90/0]$ and $[0_2/90_2/0]$, and between $[0/90_2/0]$ and $[0_2/90_4/0_2]$. The effect of the 90°-layer thickness on the transverse crack formation is clearly illustrated. The final failure of the laminates is basically determined by the load-carrying 0°-layer; and the thickness of the 90°-layer does not seem to have any effect on final failure.
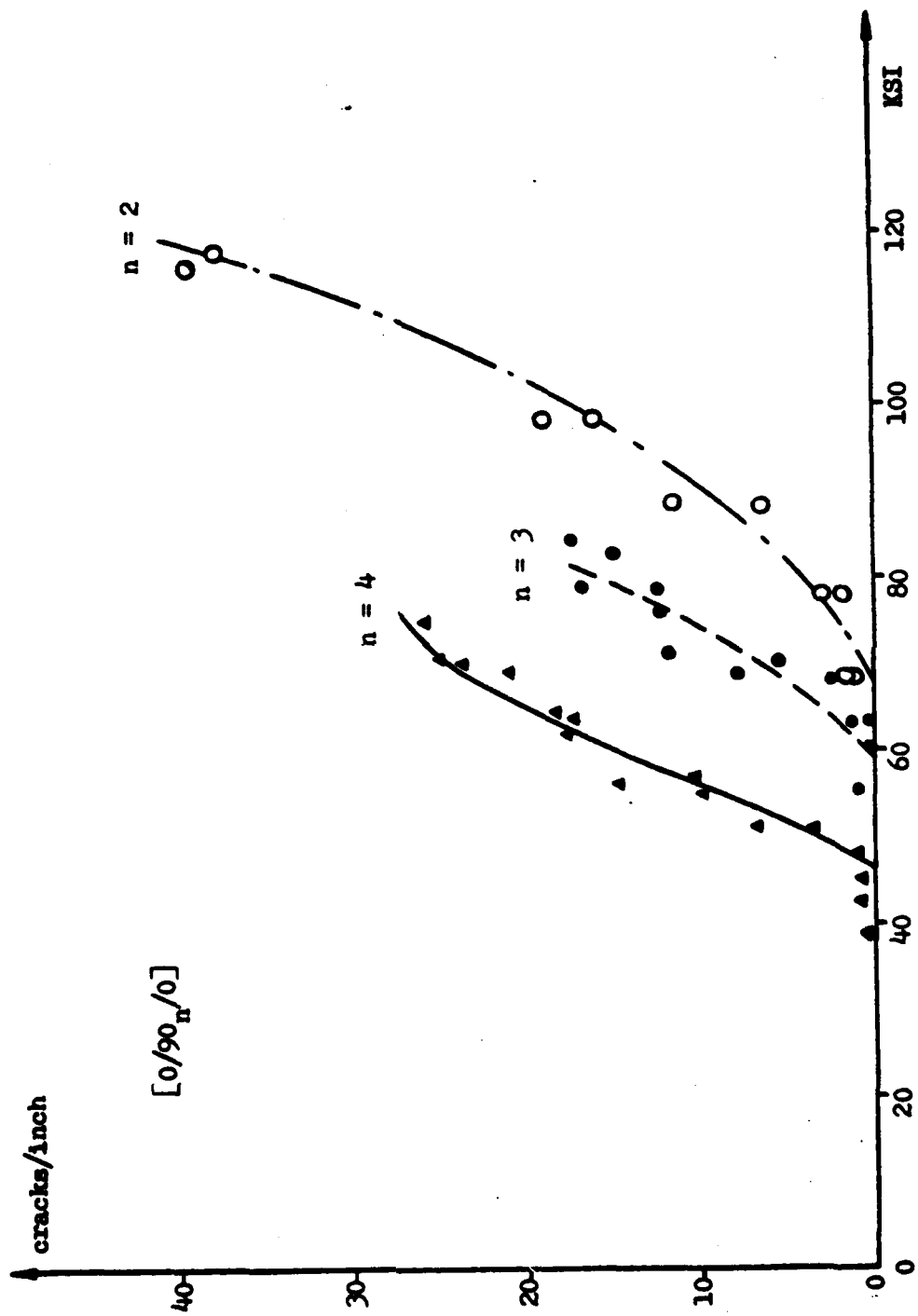
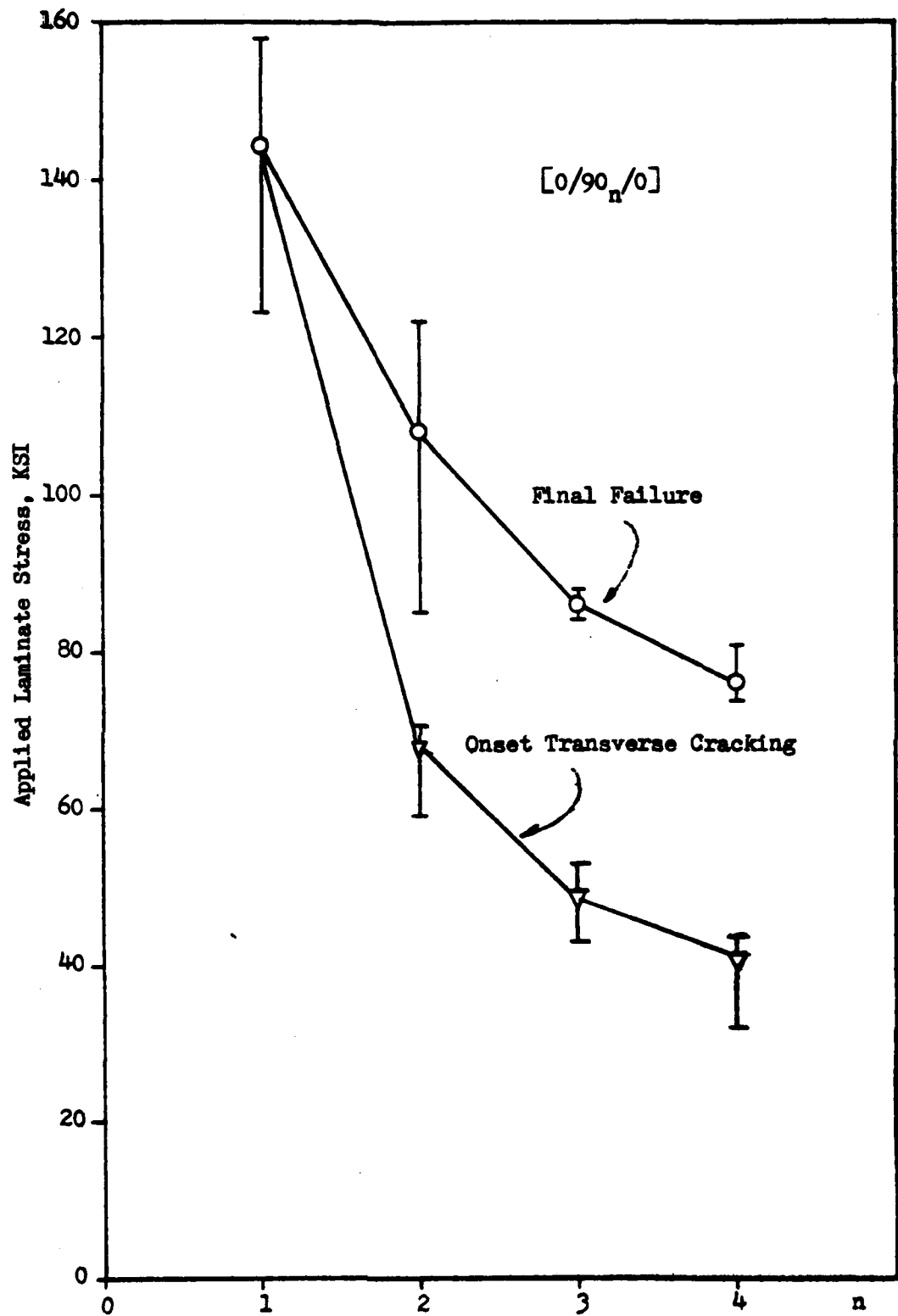Figure 3.7 Transverse Crack Density vs. Applied Tensile Stress for [0/90ₙ/0] Laminates.
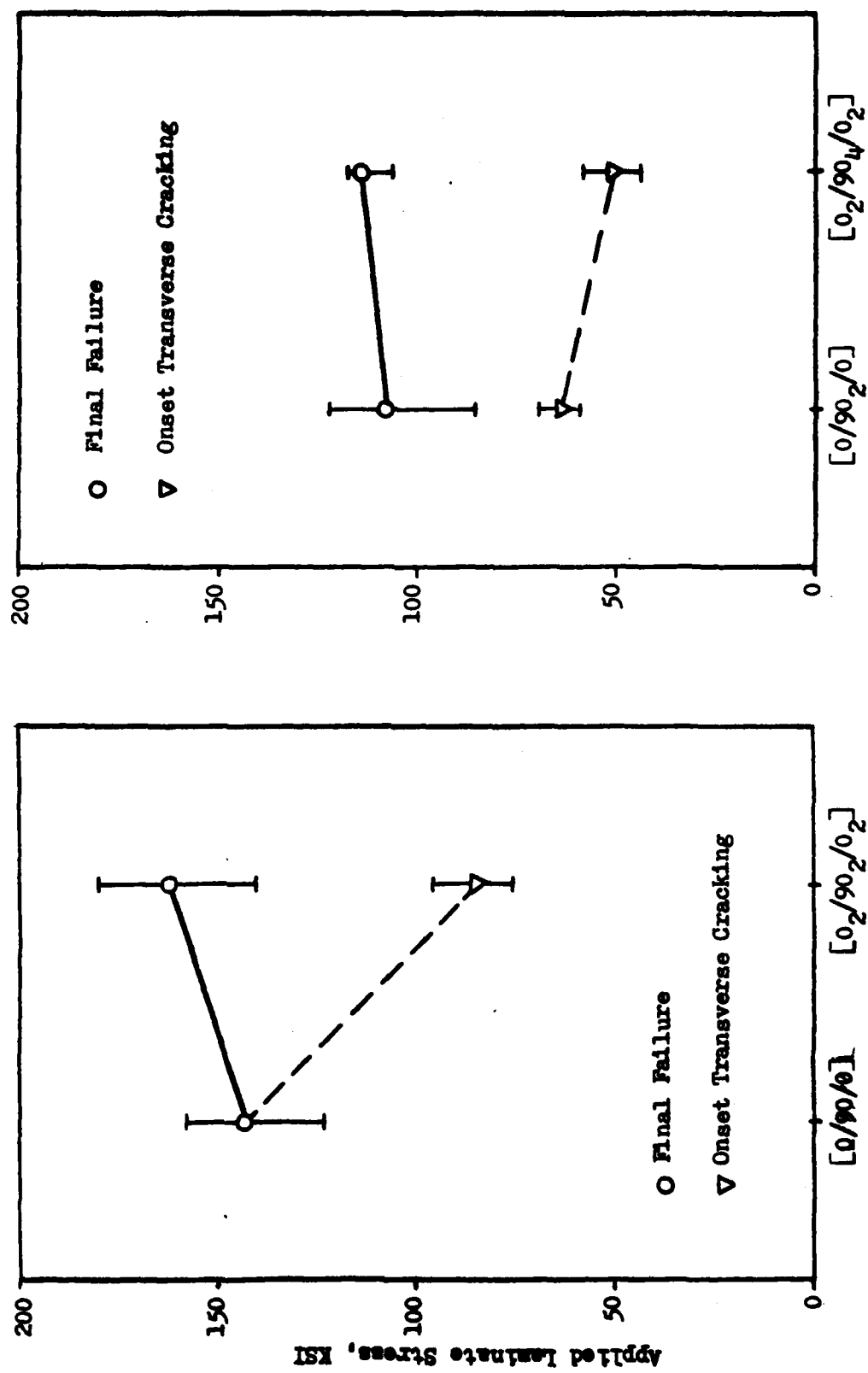
68

Figure 3.8 Test Results for [0/90ₙ/0] Laminates

Figure 3.9 Comparison of Test Results between $[0/90_n/0]$ and $[0_2/90_{2n}/0_2]$ Laminates.

70

Finally, a number of the $[0_2/90_4/0_2]$ laminates were tested under controlled temperature environments. In addition to tests in room temperature (78°F), tests were also conducted under -80°F and 156°F conditions. Test results are displayed in Fig. 3.10. It is seen that the onset stress for transverse cracking increases with the test temperature, suggesting that a toughening effect against 90°-cracking is developed by the increase temperature. However, these results are only exploratory in nature, more comprehensive experiments are needed to draw any concrete conclusion. The final failure of the laminate is controlled by the $0°-$ layer, and it is not effected by the increase of the test temperature.

(c) <u>Crack Growth in the $[\pm 25/90_n]_s$-Family.</u> In this series, laminates of $[\pm 25/90_n]_s$, n = 1/2, 1,2,3,4,6,8 as well as $[\pm 25_2/90_2]_s$ were incrementally loaded and radiographically examined. Table 3.3 summarizes the results obtained in these tests. For purpose of comparison, tests results for $[\pm 25]_{2s}$ and $[90_8]$ laminates are also listed in Table 3.3. The average stresses at onset of transverse cracking, edge delamination and final failure are tabulated, with the range of scatter given in parenthesis.

In all cases, the laminate stress-strain response was found to be essentially linear until failure. It is thus convenient to use the laminate tensile strain $\bar{e}_x$ as a measure of the applied load. A graphical representation of the data given in Table 3.3 is displayed in Fig. 3.11. Here, the applied laminate strain $\bar{e}_x$ at the onset of transverse cracking, edge delamination and final failure is plotted against the number of 90°-plies, denoted by n.
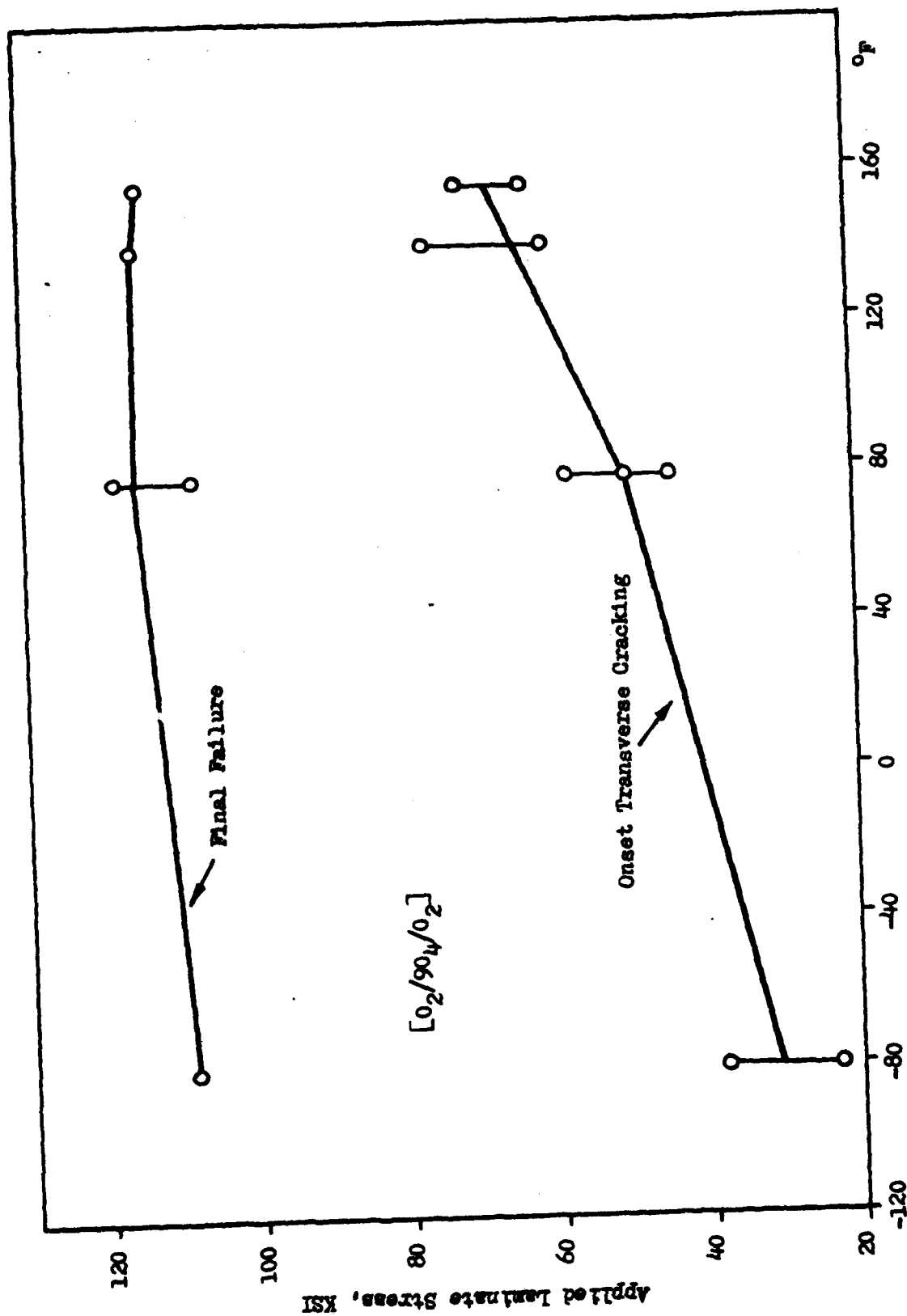
Figure 3.10 Test Results of $[0_2/90_4/0_2]$ Laminates under Temperature Environments

Table 3.3 Summary of Tensile Tests on $[\pm 25/90_n]_s$ Laminate Series

n	Young's Modulus (Msi)	Laminate Stress at Onset of Trans. Cracking (ksi)	Laminate Stress at Onset of Free-Edge Delamination (ksi)	Ultimate Tensile Strength (ksi)	Number of Specimens Tested
0	11.1	-	-	74.6(69.6-78.0)	3
1/2	10.5	-	63.5(61.6-66.3)	68.3(66.0-71.4)	3
1	10.0	-	59.3(57.0-59.9)	66.6(65.7-67.3)	4
2	7.92	32.9(30.0-35.2)	47.0(45.1-48.2)	51.6(49.6-54.8)	4
3	6.60	23.9(21.3-24.2)	39.2(37.4-41.6)	42.4(40.9-43.8)	4
4	5.70	18.4(18.4-18.4)	30.6(29.0-31.3)	30.6(29.0-31.3)	3
6	4.74	15.7(14.2-17.4)	18.6(18.1-19.6)	20.3(19.3-21.3)	3
8	3.81	13.2(12.4-14.2)	13.7(13.4-14.2)	14.7(14.1-15.1)	4
2*	9.50	40.9(39.5-42.2)	43.8(42.9-44.7)	47.0(45.0-49.5)	5
8**	1.64	-	-	6.40(5.99-6.99)	5

* $(+25_2/-25_2/90_2)_s$ Laminate
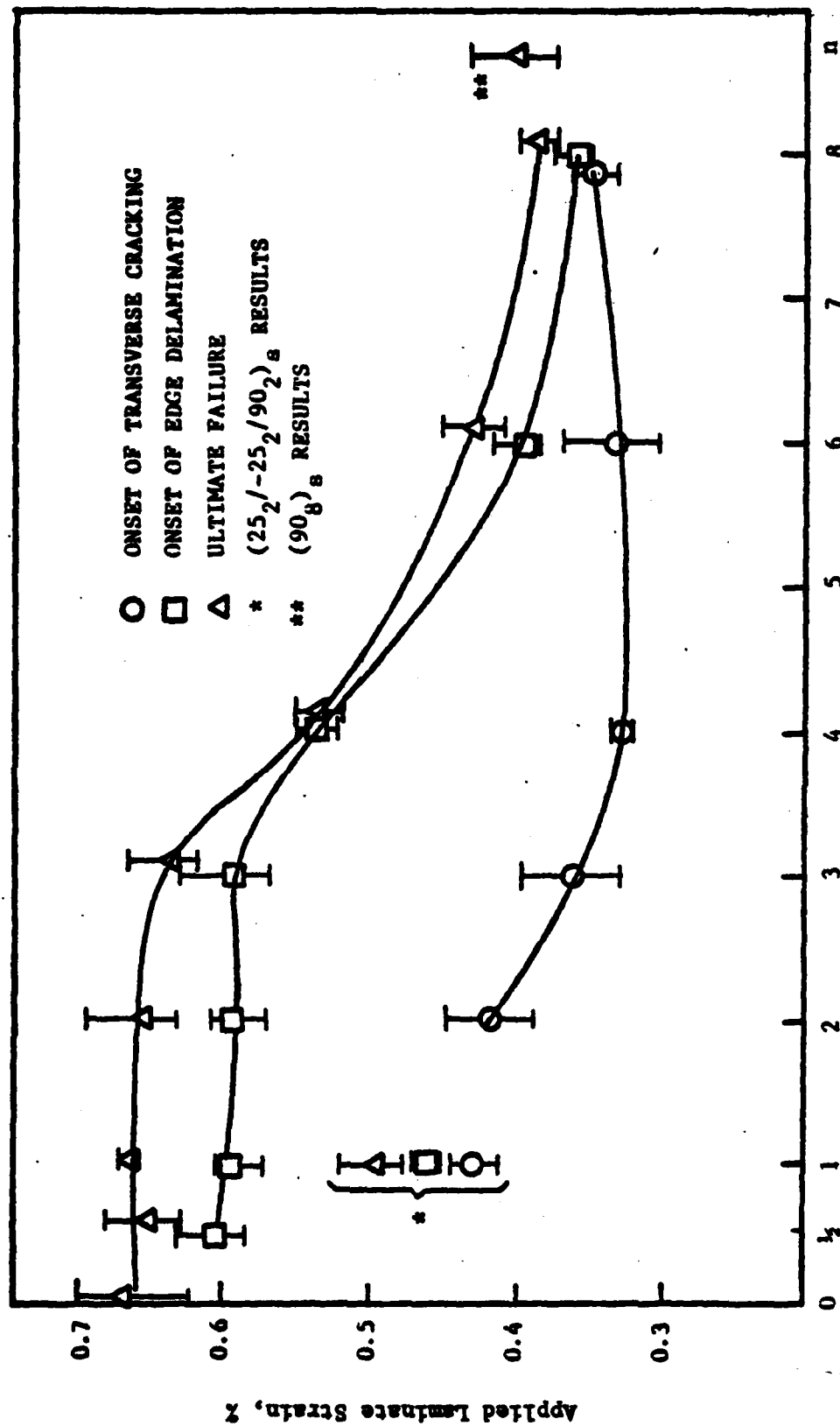
** $(90_8)_s$ Unidirectional Laminate

73

Figure 3.11 Observed Tensile Strain at the Onset of Transverse Cracking and Free-Edge Delamination, and at the Final Failure vs. the Number of 90°-plies for the $[\pm 25/90_n]_s$ Laminates.

Both the averaged value and the range of the scatter are shown for each case. The strain at failure is seen to be approximately constant for the cases of n = 1/2, 1,2,3. This value is roughly equal to the tensile strain at failure of the $[\pm 25]_{2s}$ laminate. For larger n, the strain at failure drops off significantly (discussions on this point are presented in Sections IV and V).

The onset strain for edge delamination also appears constant for the n = 1/2, 1,2,3 laminates and it drops off significantly for n > 3. The free-edge delamination generally initiates at about 90% of the strain-at-failure. In fact, the onset of edge delamination and the final failure were almost simultaneous in the $[\pm 25/90_4]_s$ laminates.

Transverse cracks were not observed in the n = 1/2 and n = 1 laminates prior to the onset of edge delamination; and the transverse cracks were largely confined within the delaminated area when they occurred. In the cases of n > 2, transverse cracks appeared before edge delamination. The onset strain for transverse cracking decreases in laminates of n = 2,3,4; and then increases slightly for n = 6 and n = 8. Generally, for the cases of n ≥ 2, the onset strain for transverse cracking is less than the ultimate tensile strain of the $[90_8]_s$ laminate. It will be shown in Section IV that this is caused by the residual thermal curing stresses in the laminate. Clearly, the onset strain for transverse cracking shows a strong dependence on n.

It is also noted that the onset strains for transverse cracking, edge delamination, and the final failure for the $[\pm 25_2/-25_2/90_2]_s$ laminate are below the values observed for the $[\pm 25/90]_s$ laminate even though these two laminates are essentially of the same construction except for the layer

75

thickness. Again, the layer thickness in this laminate plays an important role in both the cracking processes and the final failure mechanisms. In fact, the strains at the onset of transverse cracking for the $[+25_2/-25_2/90_2]_s$ and the $[\pm25/-25/90_2]_s$ laminates are about the same. Interestingly, the thickness of the 90°-layer is the same in both cases.

The transverse crack density as a function of the applied load is summarized in Figure 3.12 for the cases of n = 2,3,4,6. The range of the data is shown by the shaded band for each case. The transverse crack density N is seen to rise sharply following the onset of transverse cracking. The process of transverse cracking is enhanced, however, by free-edge delamination. Thus, an experimental limit for the transverse crack density could not be defined in these laminates either.

With this overview, it is seen that the development and transition of damage modes is dependent upon thickness of the 90°-layer. It is now convenient to separate the laminates of the $[\pm25/90_n]_s$ series into three groups as: (1) thin 90°-layer (n = 1/2, 1); (2) thick 90°-layer (n = 2,3); and (3) very thick 90°-layer (n = 4,6 8). The damage development results for these three groups will be discussed in more detail next.

Thin 90°-layer Laminates (n = 1/2, 1)

The thin 90°-layer laminates did not suffer transverse cracks prior to delamination. Their edge delamination occurred primarily inside the 90°-layer of the laminate; and it propagated stably. Final failure occurred at the laminate strain approximately equal to the failure strain of the $[\pm25]_{2s}$ laminates.
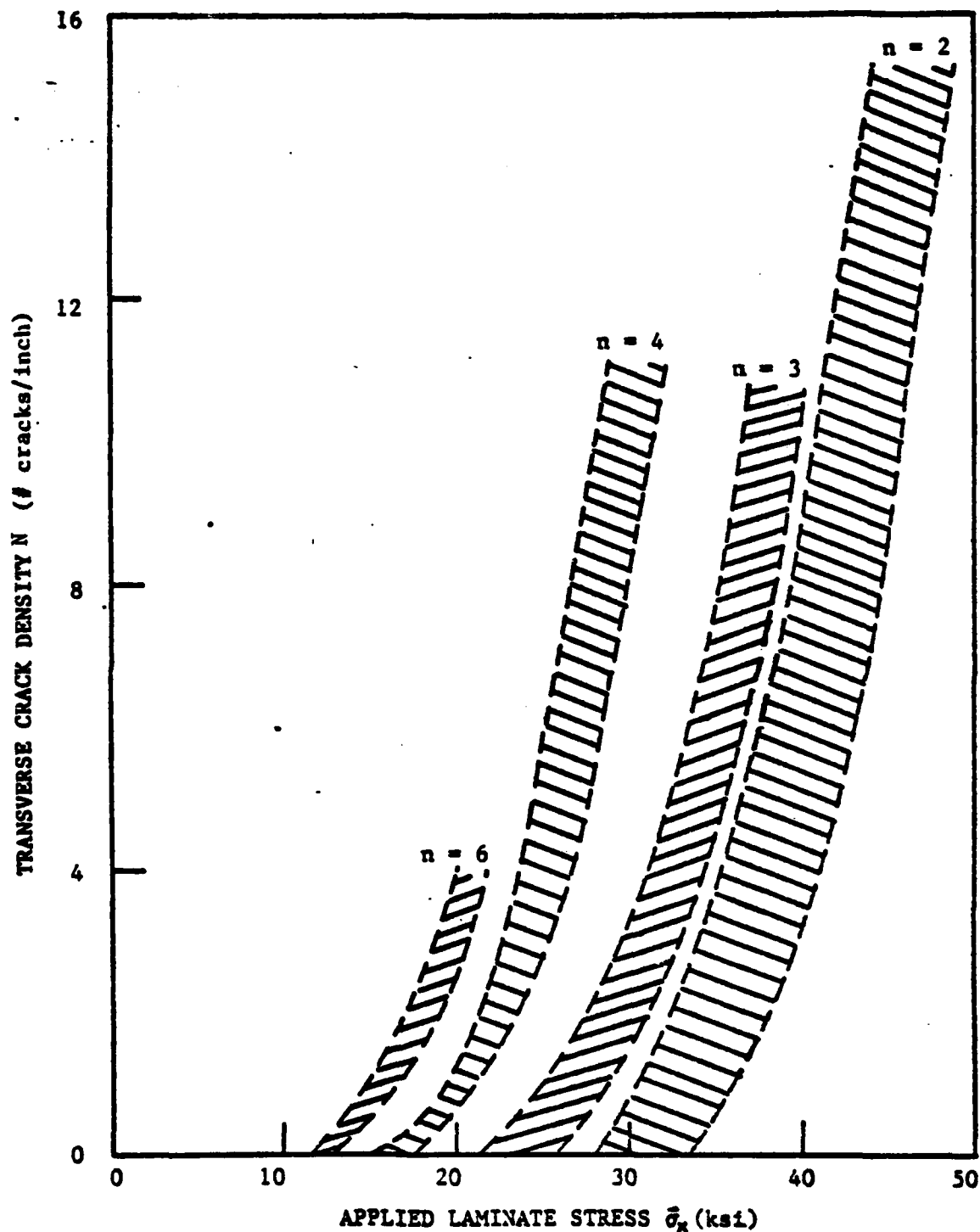
Figure 3.12   Density of Transverse Cracks vs. Applied Tensile Stress in $[\pm 25/90_n]_s$ Laminates for n = 2,3,4 and 6.

The damage development in the $[\pm 25/90_{1/2}]_s$ laminates (n = 1/2) started with a free-edge delamination along the length of one side of the test coupon and then grew larger with delamination on both sides. X-radiographs of three specimens loaded to an axial strain of $\bar{e}_x$ = 0.63% are shown in Figure 3.13. These x-rays show what appears to be transverse cracks in the delaminated region. As the ultimate load was approached, delaminations on both sides were observed to grow stably until they coalesced in the middle of the test coupon and resulted in final failure. This is shown by the failed specimen in Figure 3.13. An oblique section cut from this failed specimen was SEM examined. A magnified section view of the SEM picture shows that the delamination crack seen in the x-radiograph actually occurred mainly inside the 90°-ply, see Fig. 3.14. No transverse cracks were found to form in this laminate even after failure. The delamination is seen to initiate in the mid-plane at the free-edge, but grew inward along the 25/90 interface. Several oblique cracks are seen in the 90°-ply which may be responsible for the delamination shift. The orientation of the oblique cracks strongly suggest that a locally complex state of stress exists in the vicinity of the 25/90 interface delamination crack tip.

In the case of the $[\pm 25/90]_s$ (n = 1) laminate, mid-plane delamination was also observed as the first form of damage. However, transverse cracks occurred in the delaminated region, see Fig. 3.15; and these extended across the entire width of the specimen. The strains at the onset of delamination and at the final failure are approximately equal to those for the n = 1/2 case. It appears that the transverse cracks in the $[\pm 25/90]_s$ laminate did not have any effect on the mechanisms that caused edge delamination. And the final failure is

78

Figure 3.13 X-radiographs of Three $[\pm 25/90_{1/2}]_s$ Specimens after Loading to an Axial Strain of 0.63%.

(a)
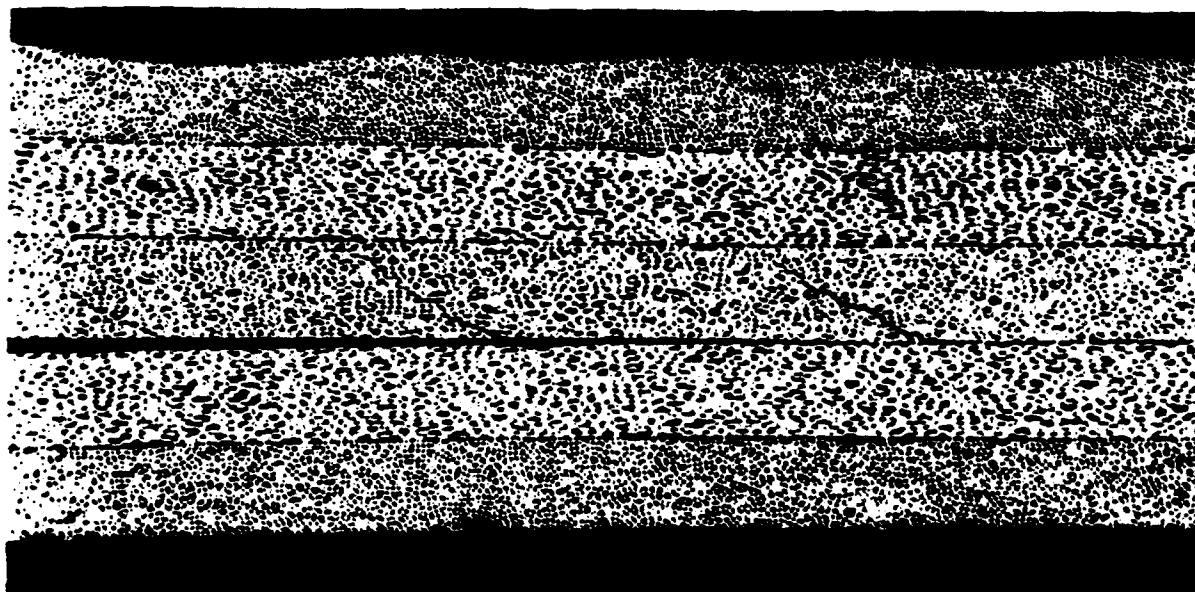
200 μm
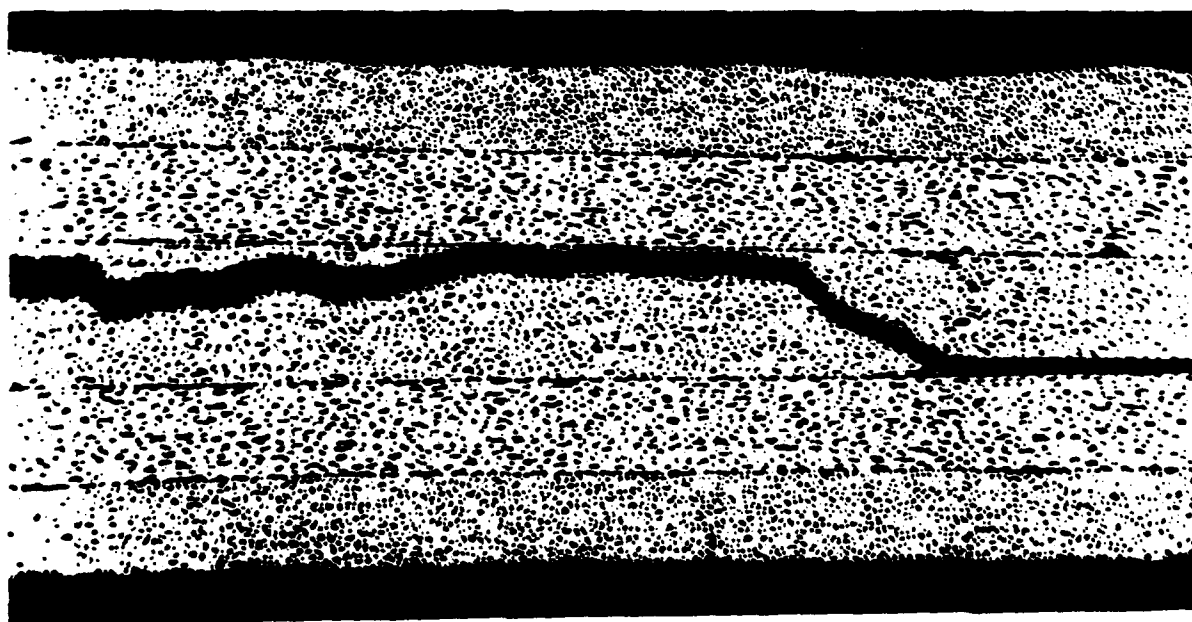
(b)

Figure 3.14   Photomicrograph of the Delaminated Region in the $[\pm 25/90_{1/2}]_s$
Specimen for the Oblique Section Shown in Fig. 3.13.

(a)   (b)

Figure 3.15 X-radiographs of A $[\pm 25/90]_s$ Specimen Taken At
(a) $\bar{e}_x = 0.64\%$ and (b) $\bar{e}_x = 0.67\%$.

81

controlled by the load-carrying $\pm 25°$-layer. The sub-laminate cracking event did not seem to affect the load-carrying capacity of the $25°$-layer.

Thick 90°-layer Laminates (n = 2,3)

The thickness of the 90°-layer in these laminates is typically found in most practical laminates. For both cases of n = 2 and n = 3, transverse cracking was the first damage mode under the load. A high density of transverse cracks was reached prior to the onset of delamination. Delamination occurred mainly in the 90°-layer for n = 2, but mainly along the 25/90 interface for n = 3. Delamination crack growth was generally stable, although the growth was quite limited in the case of n = 3, see, e.g., Fig. 3.1. The ultimate strength of the n = 2 laminates is also approximately equal to the strength of the $[\pm 25]_{2s}$ laminates. But, a reduction in the final failure strain is indicated for the case of n = 3, see Fig. 3.11. A degradation in strength has also been found in the laminates to be discussed next.

Very Thick 90°-layer Laminates (n = 4,6,8)

The first form of damage for the very thick 90°-layer laminates is also transverse cracks, which occur at a much lower stress level. Stress concentrations at the transverse crack tip and at the free-edge of the specimen cause a delamination along the 25/90 interface. The triangular shape of the delamination plane observed in the x-radiographs indicates that there is an interaction between these two modes of damage. The growth of this type of delamination appeared very unstable; and the final failure occurred at a laminate strength significantly less than the strength of the $[\pm 25]_{2s}$ laminate.

82

The delamination growth process of a $[\pm 25/90_4]_s$ laminate is illustrated by the x-radiographs shown in Figure 3.16. The x-rays show that no typical edge delamination occurred up to a load of 96.8% UTS. At the load of 99.9% UTS, a delamination originated at the transverse crack tips is developed, which extends across the full width of the coupon. A small increase in load was then sufficient to cause the final failure. An important feature of the damage in this (n = 4) laminate is the triangular shape of the delamination near the free edge. The apex of the triangle is clearly aligned with the transverse crack shown by the arrow in the figure. In the previously discussed cases of n < 4, the delamination crack front was always of a thumbnail shape when it first formed. This difference in the shape of delamination indicates clearly a change in the mechanisms that control the initiation and growth of the delamination. The damage development process for the case of n = 6 is similar, with more pronounced transverse crack-induced delamination which was observed in the experiment of this laminate.

Figure 3.17 displays the damage in two $[\pm 25/90_8]_s$ laminates after tensile loading to 97% UTS. An example of transverse crack tip induced delamination is shown in picture (a), where a dark zone (delamination) associated with a transverse crack is indicated by an arrow. The x-radiograph in (b) shows delaminations occurred in both the upper and lower 25/90 interfaces. The apex of the triangular shaped dark areas marked by the arrows are clearly aligned with a transverse crack tip delamination. It is concluded that the stress concentrations at a transverse crack tip interact with the free-edge stresses to cause this delamination.

Figure 3.16 X.-radiographs Showing Edge Delamination
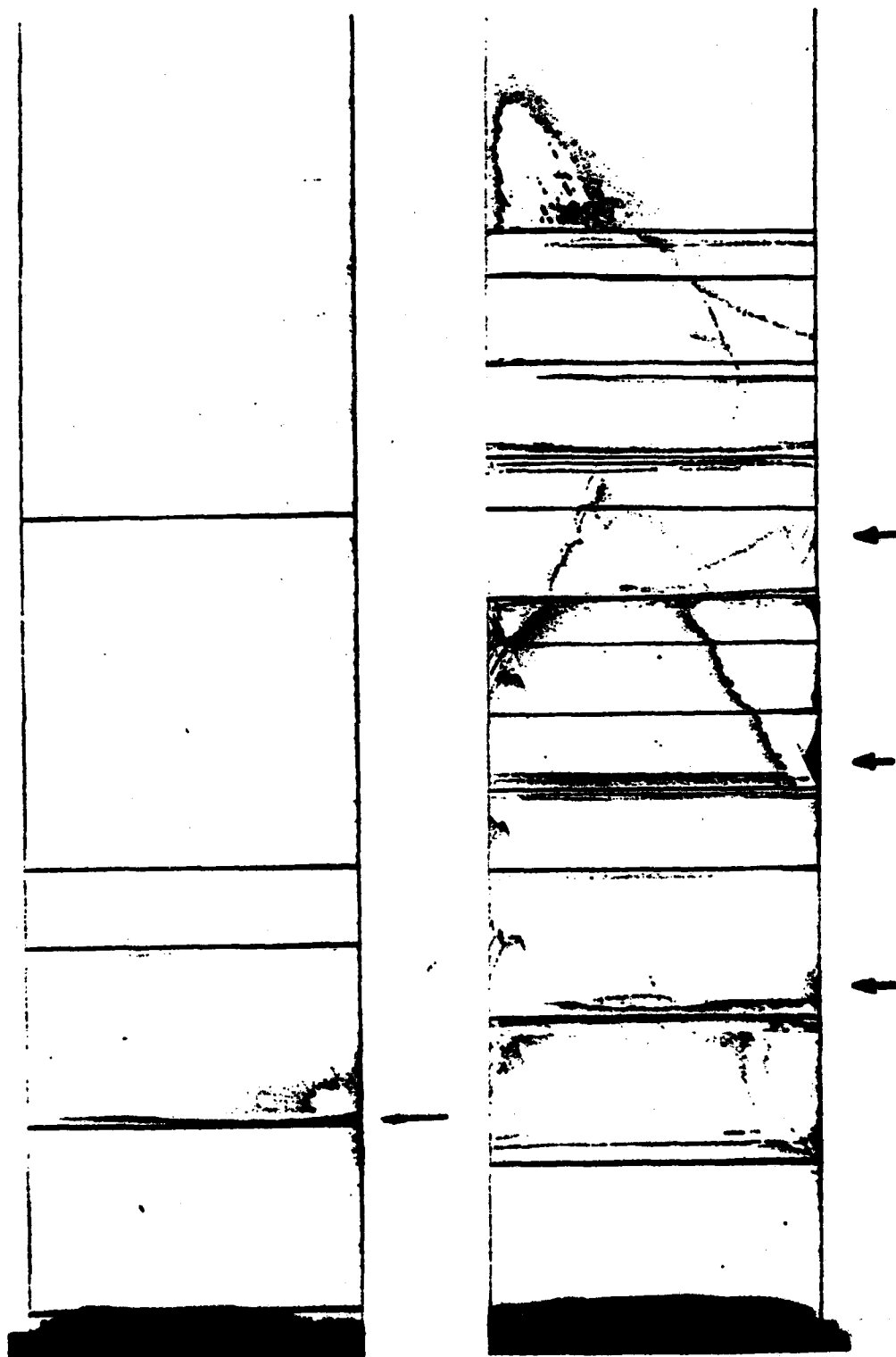Growth in a $[\pm 25/90_4]_s$ Specimen.

84

Figure 3.17 X-radiographs of Two $[\pm 25/90_8]_s$ Specimens after Tensile Loading to 97% UTS

The foregoing discussions illustrated the significant effect of the 90°-layer on the damage modes and their growth mechanisms in the $[\pm 25/90_n]_s$ laminates. Fig. 3.18 provides a schematic summary of the fracture sequences in this $[\pm 25/90_n]_s$ series. Column (a) shows the development of transverse cracks just before the onset of edge delamination, as seen in the plane view x-radiographs. Column (b) shows the plane and edge views (the broken lines are the 25/90 interface) of the test coupon immediately after edge delamination. Column (c) shows the plane views and edge views of the specimen before their final failure (transverse cracks are shown in the edge views only when they are associated with the initiation of a 25/90 delamination at the transverse crack tip).

The fracture sequences shown in Fig. 3.18 illustrate that the chosen grouping by 90°-layer thickness coincides with transitions in the several different damage modes in the $[\pm 25/90_n]_s$ series found in the experiment.

Recall for the $[\pm 25/90_n]_s$ laminates, that the observed fracture modes consisted of mainly fiber breakage. The failure section of the specimen was essentially transverse to the load direction, see Fig. 3.4. Similar fracture modes were observed for the $\pm 25°$-layer in the final failure of all the laminates in the $[\pm 25/90_n]_s$ series. The morphology of the fracture of the $\pm 25°$-layers appears to be the same for all of the laminates investigated. However, the laminate strains $\bar{e}_x$ at the final failure show a strong dependence on the thickness of the 90°-layer, especially when it is thick. Further, once edge delamination occurs, final failure is imminent. Apparently, the growth of delamination has some ill-effects on the final failure; the exact mechanisms will not be investigated in this report, however.
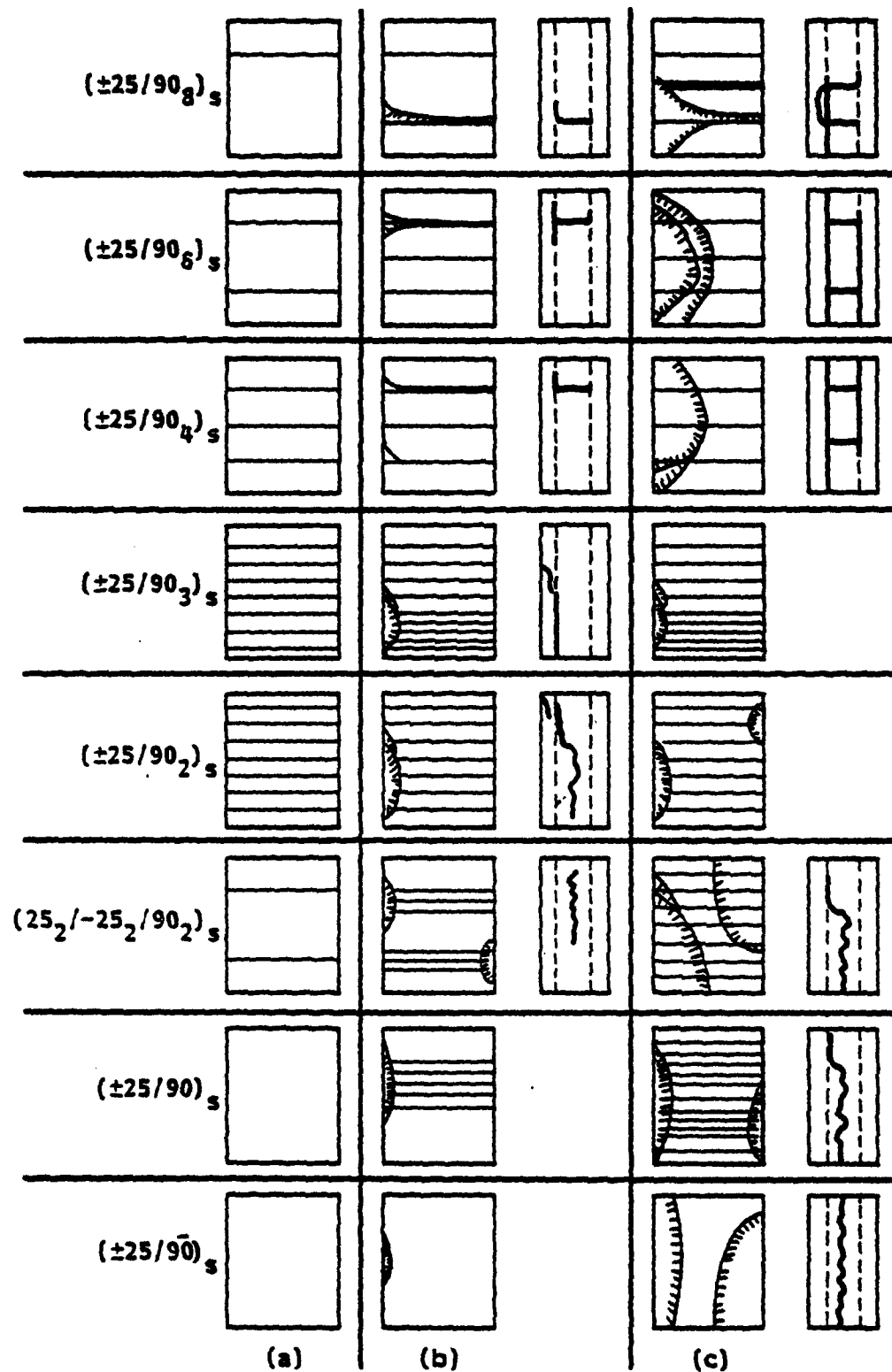
Figure 3.18 Schematic of the Fracture Sequences in the $[\pm 25/90_n]_s$ Laminates, (a) Just Prior to Edge Delamination, (b) Subsequent to Edge Delamination, and (c) Just Prior to the Final Failure.

87

(d) **Mixed-Mode Fracture in Notched $[\theta_8]$-Family.**   This series of tests con-
sisted of a class of off-axis, $[\theta_8]$ laminates.   The test specimens were cut
with 0.15" double-side notches using a nominal 8-mil diamond blade. The off-
axis angle θ varied from 0° to 90° at 15° intervals. A general configuration
of the test specimen is illustrated in Fig. 3.19.

Under uniaxial tension, fracture failure was induced in each specimen
with the crack initiating from the notch tip and propagating along the fiber
direction. Thus, a class of matrix-dominated, mixed-mode fracture was ex-
perimentally determined. Fig. 3.19 shows a plot of the far-field laminate
stress σ_0 at onset of fracture versus the fiber angle θ.

A finite element simulation of the crack propagating from the notch
tip along the fiber direction was then conducted (the numerical details are
presented in Section IV). The calculated energy release rates G_I and G_{II}
for each value of θ are displayed in Fig. 3.20.   It is seen that for $\theta \geq 60$
the fracture is essentially of mode I only. For smaller θ, mode-II contri-
bution increases rapidly. Fig. 3.21 shows the ratio of G_{II}/G_I as a function
of θ.

Correlating the calculated energy release rates with the experimental
results, the materials fracture resistance property may be evaluated. For
example, Fig. 3.22 shows the experimentally determined mixed-mode energy
release rate $G_{(I,II)c}$ of the material as a function of the G_{II}/G_I ratio. It
is seen that for $\theta \geq 60°$, $G_{(I,II)c} \sim G_{Ic}$ because the fracture was essentially
of mode I, the average value for G_{Ic} is

$$G_{Ic} \sim 0.9 \text{ in-lb/in}^2 \tag{3.4}$$
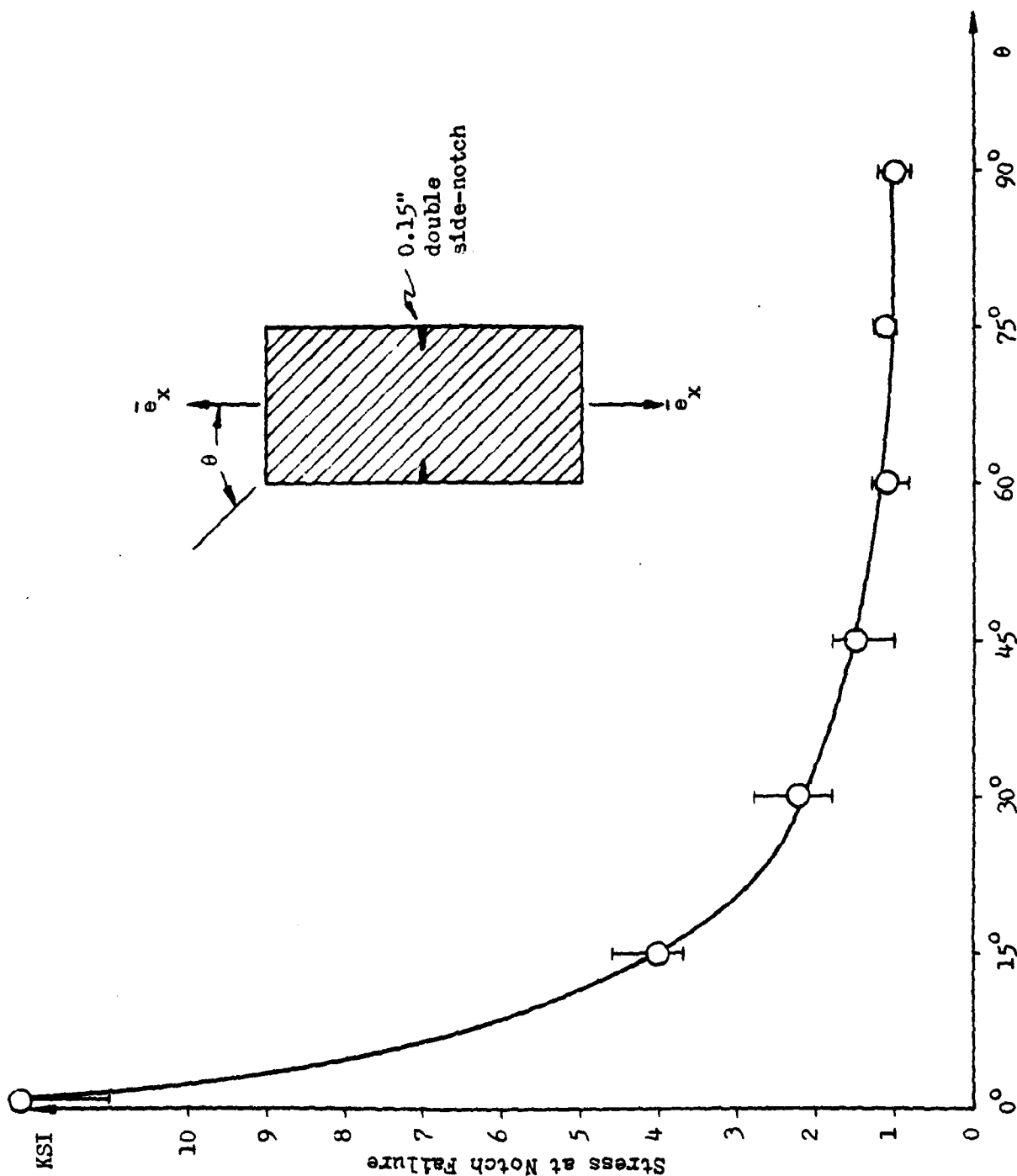
Figure 3.19 Mixed-Mode Fracture Data of the Notched $[\theta_8]$ Laminates.

89
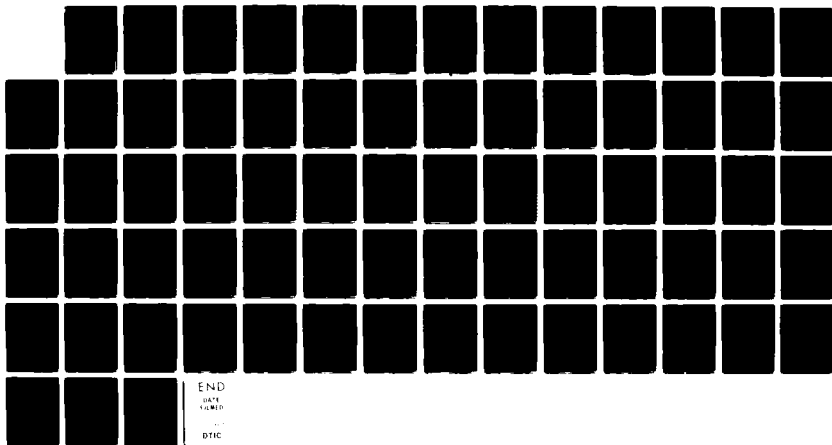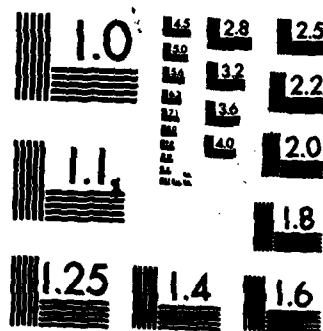
MICROCOPY RESOLUTION TEST CHART

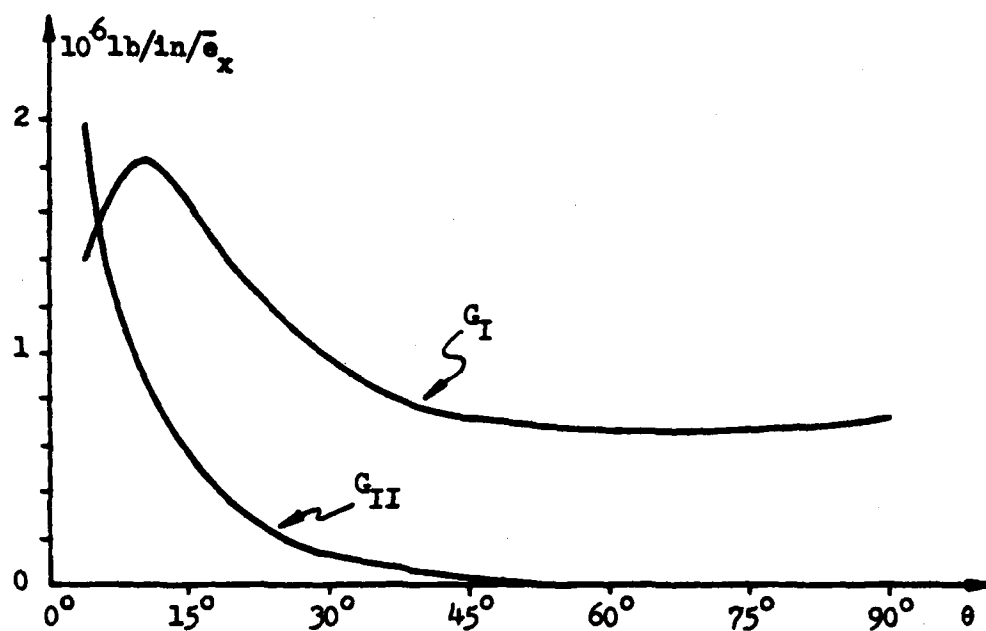NATIONAL BUREAU OF STANDARDS-1963-A

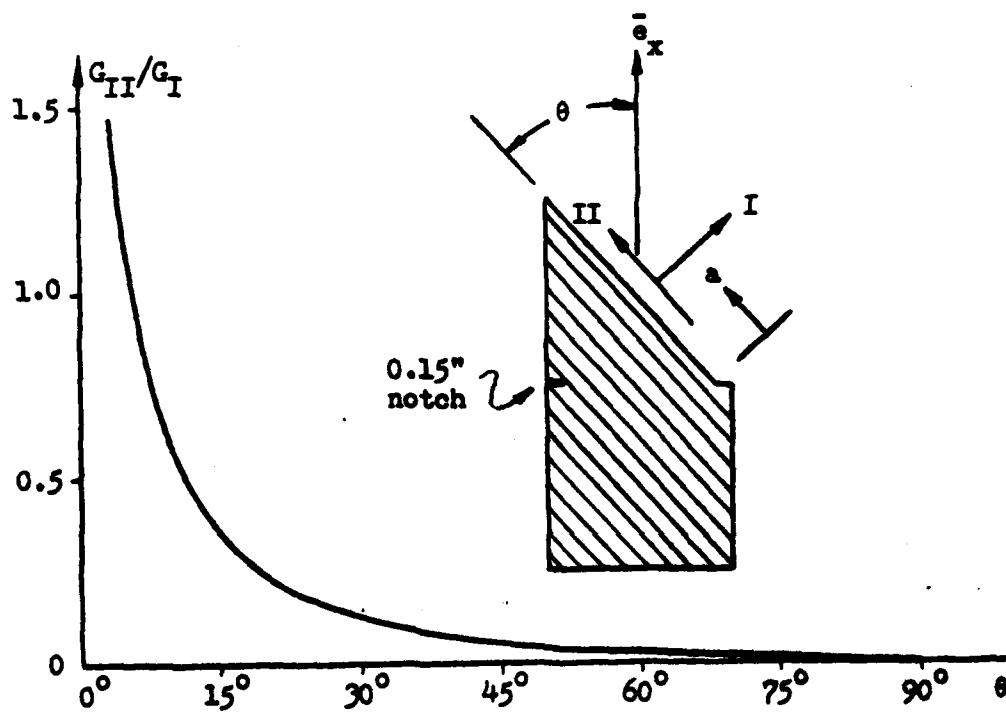**Figure 3.20 Calculated G_I and G_{II} as a Function of θ.**

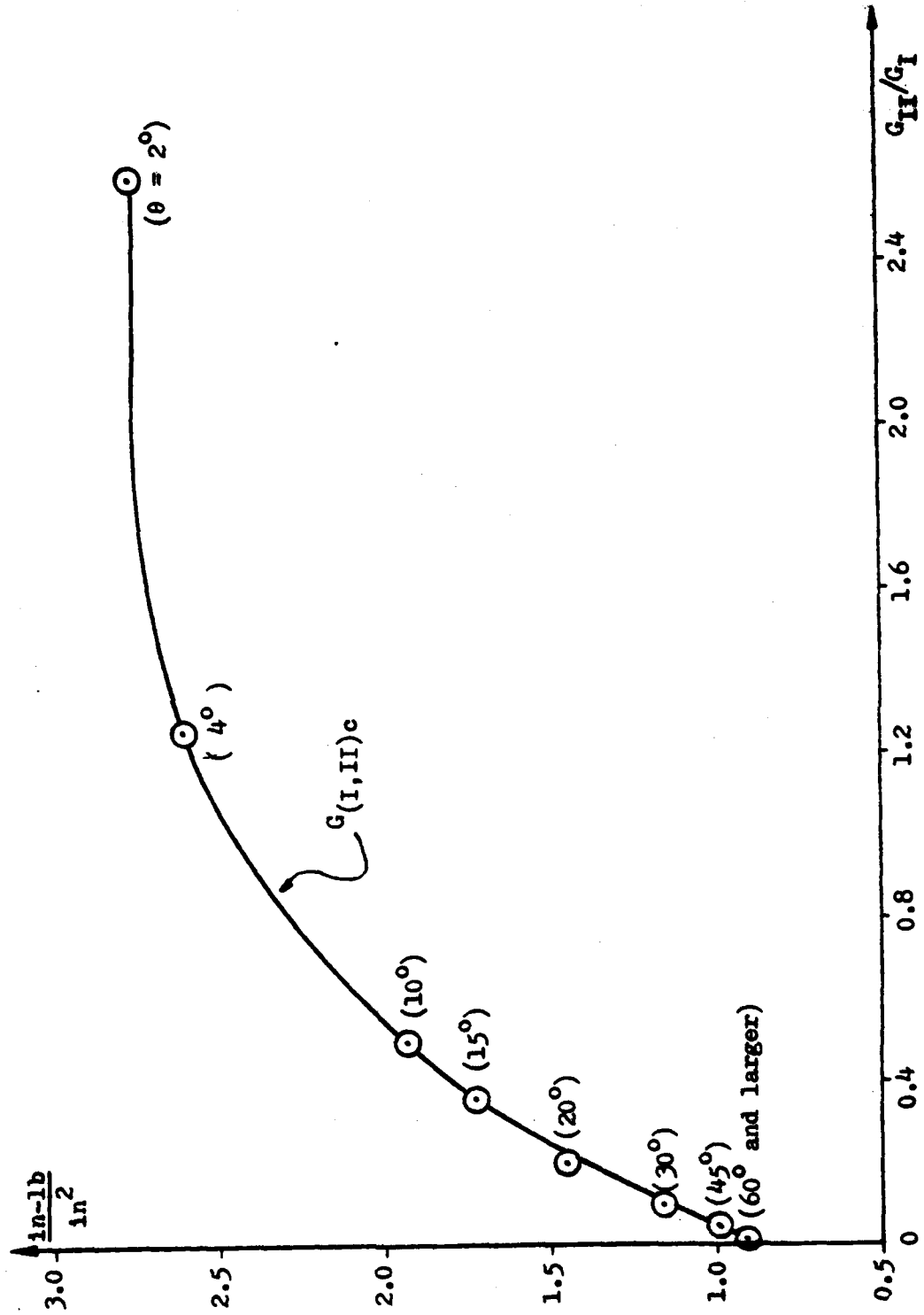**Figure 3.21 G_{II}/G_I Ratio as a Function of θ.**

Figure 3.22 Material Fracture Resistance $G_{(I,II)c}$ versus G_{II}/G_I Ratio

Note that the value of G_{Ic} determined in this experiment represents the fracture resistance of the unidirectional composite against the type of cracking as illustrated in Fig. 1.8(a); it is essentially a case of 0°/0° interface delamination.

Similar values for G_{Ic} (0.8-0.92 in-lb/in^2) were obtained by Cullen [11] and Williams [12] who used the AS-3502 composite system and tested under a different set of specimen configurations.

From Fig. 3.22, it is also seen that the value of $G_{(I,II)c}$ increases with the ratio of G_{II}/G_I, suggesting that the energy required to fracture a mixed-mode crack is not constant; it may be dependent on the amount of the shearing action. In addition, the plot in Fig. 3.22 indicates the existence of G_{IIc}, being

$$G_{IIc} \approx 2.80 \text{ in-lb/in}^2 \tag{3.5}$$

Dependence of the fracture energy on the G_{II}/G_I ratio has been encountered recently by Vanderkley [13], who also tested the unidirectional AS-3502 composite system. And, the existence of G_{IIc} (at the macroscopic level) has been discussed by Wilkins [28]. For the AS-3501-06 graphite-epoxy system used, Wilkins found the value of $G_{(I,II)c}$ (0°/0° delamination) ranged from 2.1 to 2.98 in-lb/in^2 with G_{II}/G_{II} equaled 3.4. This range is within the same experimental range of the present study.

Apparently, the problem of mixed-mode crack propagation is much more complicated than the limited study has shown here. It requires concentrated efforts on this particular subject, both experimentally and analytically.

In the case of the double-side notched $[90_8]$ laminate, the calculated energy release rate G_I can be expressed in terms of the notch size a,

$$G_I(a) = 4.75 \times 10^6 \cdot a \cdot \bar{e}_x^2 \qquad (3.6)$$

Now, using the failure strain of the unnotched $[90_8]$ specimen $\bar{e}_x = 0.39\%$ from Table 3.1, and the critical energy release rate $G_{Ic} = 0.9$ lb/in from (3.4), we obtained for the macroscopic material flaw size

$$a_0 \sim 0.0125''. \qquad (3.7)$$

This is about 2.5 times the thickness of a single material ply.

IV. FINITE ELEMENT ANALYSIS AND EXPERIMENTAL CORRELATIONS

4.1 Finite Element Formulation

Shown in Fig. 4.1 is the cross-section of a symmetric laminate. Assume the laminate is long in the axial x-direction. Then, under the axial tensile load F_x, the displacement field of the laminate can be expressed in the general form [3].

$$u(x,y,z) = e_0 x + U(y,z)$$
$$v(x,y,z) = V(y,z) \qquad (4.1)$$
$$w(x,y,z) = W(y,z)$$

where e_0 is the uniform axial laminate strain induced by F_x, and V and W are the y and z displacements respectively, which are independent of x. The function U represents the warping of the laminates cross-section. Owing to symmetry, the solution field can be reduced to the first quadrant of the laminate cross section as shown by the shaded region in Fig. 4.1. The solution region is then represented by a network of nodes and triangular elements as shown in Fig. 4.2 with the following symmetric boundary conditions,

$$u(0,z) = v(0,z) = 0$$
$$w(y,0) = 0 \qquad (4.2)$$

The formulation of the (constant strain) triangular finite element based on the displacement field of (4.1) begins with the nodal force-displacement relationship for a typical element,

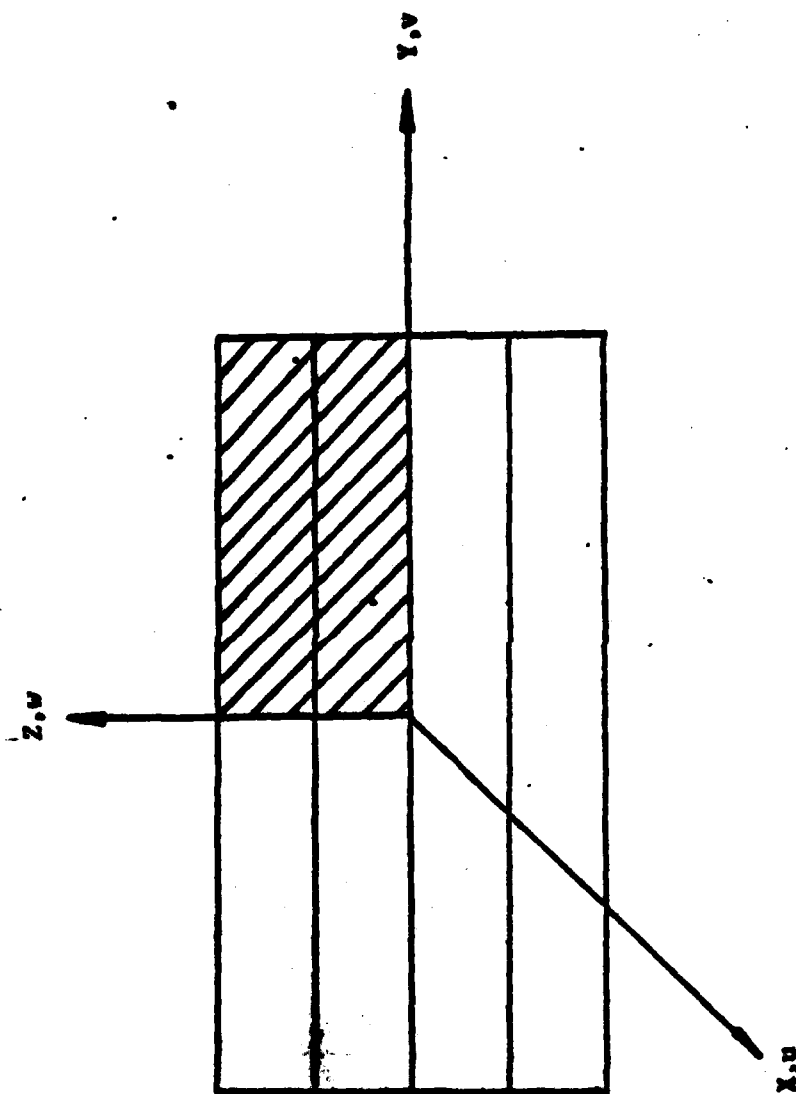$$R_i - R_i^0 = K_{ij} \delta_j \qquad i,j = 1,9 \qquad (4.3)$$

94

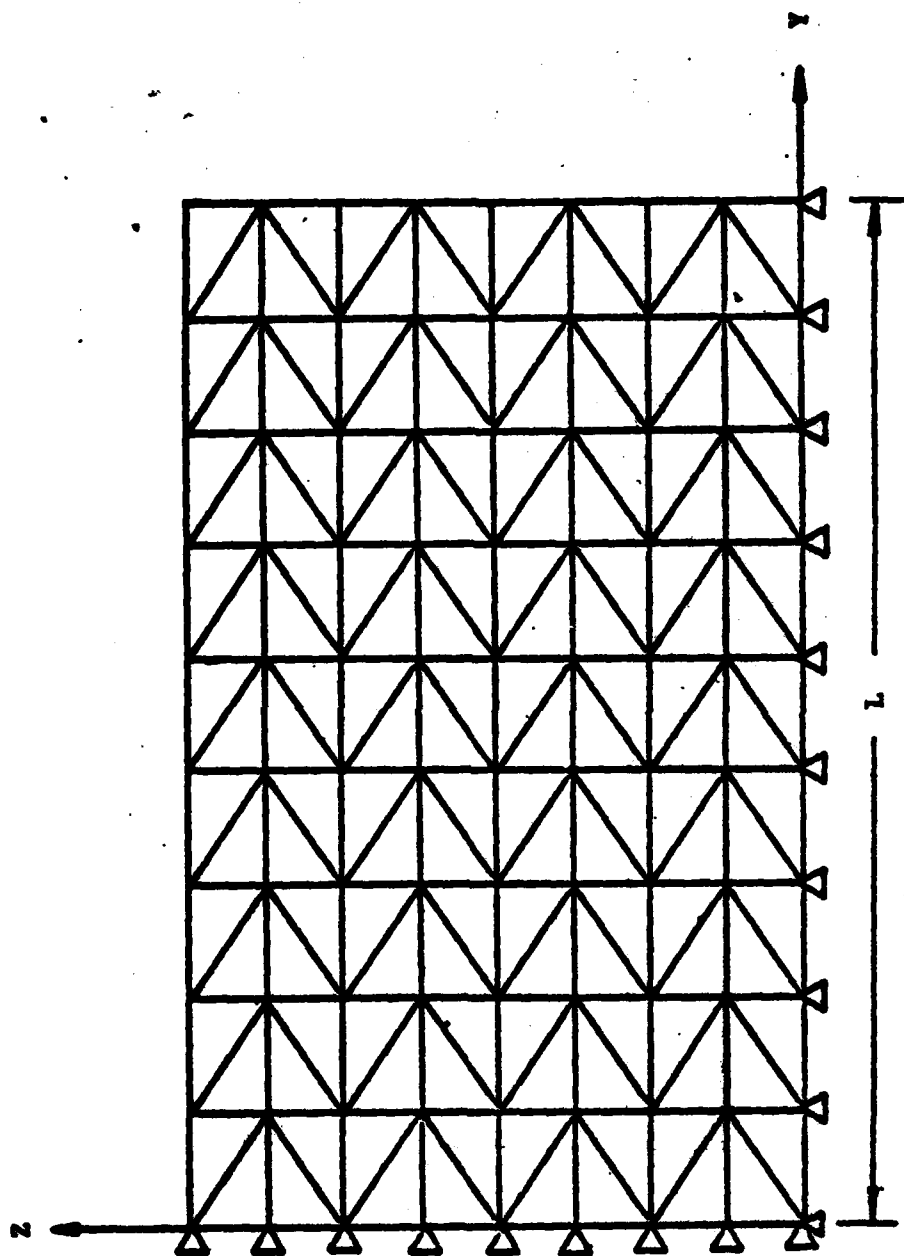Figure 4.1   Symmetric Laminate Geometry

Figure 4.2   Finite Element Gridwork.

96

where K is the element stiffness matrix and R^0 represents the element residual nodal force vector. The δ vector denotes the u, v, w functions at the three nodes of the element and R represents the "reactive" nodal forces (see details in Ref. [6]).

Assume the material of the element is described by the generalized Hooke's Law as

$$\sigma_i = C_{ij}(e_j - \alpha_j \Delta T) \qquad i,j = 1,6 \qquad (4.4)$$

Then, the element stiffness matrix K is given by [6],

$$K_{ij} = (B_{im} D_{mn} B_{nj})V \qquad \begin{matrix} i,j = 1,9 \\ m,n = 1,5 \end{matrix} \qquad (4.5)$$

and the residual nodal forces R^0 are given by

$$R^0 = (B_{im} D_{mn} e_n^* + B_{in} \sigma_n^*)V \qquad \begin{matrix} m,n = 1,5 \\ i = 1,9 \end{matrix} \qquad (4.6)$$

where B is a 5 x 9 operator matrix depending on the coordinates of the three nodes. In (4.5) and (4.6), V is the volume (area) of the element and

$$D_{mn} = C_{(m+1)(n+1)}$$
$$e_n^* = -\alpha_{n+1}\Delta T \qquad m,n = 1,5 \qquad (4.7)$$
$$\sigma_n^* = C_{1(n+1)}[e_0 - \alpha_1 \Delta T]$$

If the axial strain e_0 is known, then the "residual" nodal forces R^0 can be calculated. Thus, for a total of N elements in the network, N sets of nine equations are obtained. However, these 9N equations can be consolidated into a set of 3M linear equations in the form

$$f_i = A_{ij} d_j \qquad i,j = 1, 3M \qquad (4.8)$$

M being the number of nodes in the network. In (4.8), f denotes the system resultant nodal force vector which consists of both the residual force R^0 and the reactive force R; A denotes the global stiffness matrix; and d represents the displacement vector of the M nodes in the fields. Equation (4.8) can be solved either given a force boundary condition, a displacement boundary condition, or mixed boundary conditions for the nodal network.

The local stresses and strains for each of the N elements can then be calculated from the nodal displacement solution as

$$\left. \begin{aligned} e_1 &= e_0 \\ e_{m+1} &= B_{mi}d_i \qquad\qquad m = 1,5; \; i = 1,9 \end{aligned} \right\} \qquad (4.9)$$

$$\left. \begin{aligned} \sigma_i &= C_{1i}(e_j - \alpha_j \Delta T) \qquad\qquad j = 1,6 \\ \sigma_{m+1} &= D_{mn}(e_n{}^* + e_{n+1}) + \sigma_n{}^* \quad m,n = 1,5 \end{aligned} \right\} \qquad (.10)$$

If the applied axial force F_x is specified, then the value of e_0 must be determined to satisfy the equilibrium condition that the sum of the forces in the x-direction be equal to F_x. For the case of a thermal load condition, the applied axial force F_x is equal to zero. Then, e_0 must be determined; e_0 represents the thermal axial strain in the plate, caused by the constant thermal load ΔT.

The present formulation can be applied to solve the free-edge delamination and transverse cracking processes by means of the "crack-closure" technique described in Section II.

The delamination process is modeled by taking the axial x-direction as the load direction of the laminate, and the applied laminate load is e_0. The free-edge of the laminate is at $y = L$ as shown in Fig. 4.2. Then the delamination process may be modeled by a crack starting at the free-edge and extending towards the z-axis along a chosen plane defined by $z = $ constant.

The transverse cracking process is modeled by taking the y-direction as the load direction of the laminate. The laminate is loaded by prescribing a uniform y-displacement boundary condition along $y = L$. The applied load in the x-direction, F_x, is specified as zero to maintain a uniaxial tensile load condition in the y-direction. Then, the transverse cracking process may be modeled by a crack starting at $z = 0$ and extending in the positive z direction.

Some simplifications in the calculation of G may be made when a crack is extended along a line of symmetry. The details concerning these simplifications, the loading conditions, and the boundary conditions will be discussed next in the actual calculation of the transverse cracking and delamination processes.

4.2 Calculation Of The Energy Release Rate

In the present analysis, both mechanical and thermal loadings are considered. The mechanical load is the uniaxial tension e_0 and the thermal loading is the uniform temperature drop ΔT. Within the context of linear elasticity, the mechanical and thermal loading cases may be solved independently under unit load conditions and then superimposed to obtain the solution for a combined load condition. It is convenient to choose the mechanical load as the far field laminate strain e_0 equal to one microstrain

(1×10^{-6}). This represents a "fixed-grip" load condition. The thermal load ΔT is chosen as minus one degree Fahrenheit for convenience. Let $\tilde{f}_m$ and $\tilde{d}_m$ be the nodal forces and displacements respectively, due to the unit mechanical strain load as determined by the finite element solution of Equation (4.8). Similarly, let $\tilde{f}_T$ and $\tilde{d}_T$ be the nodal forces and displacements respectively, due to the unit thermal load of $\Delta T = -1°F$. Then, under a combined loading of e_0 and ΔT, the nodal forces and displacements can be expressed as

$$\tilde{f} = f_m e + f_T \Delta T$$
$$\tilde{d} = d_m e + d_T \Delta T \qquad (4.11)$$

To calculate the strain energy release rate it is necessary to introduce a crack in the finite element network as described in Section II. Referring to Fig. 2.4, let $\tilde{D}$ be the relative displacements of nodes f and g when the crack is extended to $a + \Delta a$ defined as

$$\tilde{D} = \tilde{u}_f - \tilde{u}_g \qquad (4.12)$$

$\tilde{D}$ may be represented in terms of a combined mechanical and thermal load of e_0 and ΔT as

$$\tilde{D} = \tilde{D}_m e + \tilde{D}_T \Delta T \qquad (4.13)$$

where $\tilde{D}_m$ and $\tilde{D}_T$ are the relative displacements associated with the unit mechanical and unit thermal loadings respectively. Let $\tilde{F}$ be the nodal forces required to close nodes f and g together. $\tilde{F}$ may be expressed in terms of a combined load of e_0 and ΔT as

$$\tilde{F} = \tilde{F}_m e + \tilde{F}_T \Delta T \qquad (4.14)$$

100

where $\bar{F}_m$ and $\bar{F}_T$ are the nodal closing forces associated with the unit
mechanical and unit thermal loadings respectively. The energy release
rate per unit thickness may then be expressed as

$$G = \left[\frac{1}{2\Delta a} (\bar{F}_m e + \bar{F}_T \Delta T) \cdot (\bar{D}_m e + \bar{D}_T \Delta T)\right] t \qquad (4.15)$$

where Δa is the incremental crack extension as shown in Fig. 2.4.
Equation (4.15) may be rewritten in the form

$$G = [C_e (e_0)^2 + C_T (\Delta T)^2 + C_{eT} (e)(\Delta T)] t \qquad (4.16)$$

where *

$$C_e = (\bar{F}_m \cdot \bar{D}_m)/2\Delta a$$

$$C_T = (\bar{F}_T \cdot \bar{D}_T)/2\Delta a \qquad (4.17)$$

$$C_{eT} = (\bar{F}_m \cdot \bar{D}_T + \bar{F}_T \cdot \bar{D}_m)/2\Delta a$$

The parameter t, appearing in Eq. (4.16) is the scale factor of length
between the actual dimension and the finite element dimension of the specimen.
Note that, for a given geometry and material properties, equations (4.17)
are functions of the non-dimensional crack length a/t and are independent
of the applied loading. Thus, the functions C_e, C_T, and C_{eT} are character-
istic for a particular crack growth and are hereafter denoted as the "energy
release rate coefficient functions".

The mechanical load coefficient function C_e may be expressed in terms
of the x, y, z components of $\bar{F}_m$ and $\bar{D}_m$ as

---

* The expression for C_{eT} is equivalent to Eq. (2,31)

$$C_{eI} = (F_{my} \cdot D_{my})/2\Delta a$$

$$C_{eII} = (F_{mx} \cdot D_{mx})/2\Delta a \qquad (4.18)$$

$$C_{eIII} = (F_{mz} \cdot D_{mz})/2\Delta a$$

noting that

$$C_e = C_{eI} + C_{eII} + C_{eIII} \qquad (4.19)$$

The subscripts I, II, and III are identified with the mode I, mode II and mode III crack extension modes respectively. Similar expressions may be obtained for the thermal and mixed load coefficient functions. Thus, the mode I, mode II, and mode III components of the energy release rate may be expressed in terms of the coefficient function as

$$G_I = t[C_{eI}(e)^2 + C_{TI}(\Delta T)^2 + C_{eTI}(e)(\Delta T)]$$

$$G_{II} = t[C_{eII}(e)^2 + C_{TII}(\Delta T)^2 + C_{eTII}(e)(\Delta T)] \qquad (4.20)$$

$$G_{III} = t[C_{eIII}(e)^2 + C_{TIII}(\Delta T)^2 + C_{eTIII}(e)(\Delta T)]$$

4.3 Numerical Solution Convergence Study

The numerical solution of the transverse cracking and delamination problems requires an optimal finite element discretization which yields sufficiently accurate results with minimum computational requirements. Lacking an exact solution for comparison, the acceptability of the numerical approximation is determined here by comparisons between the results obtained from various node and mesh distributions.

For example, consider the interlaminar shear stress distribution in the vicinity of a transverse crack of the $[\pm 25/90]_s$ laminate, see Fig. 2.10 The calculated interlaminar shear stress τ_{yz} along the 25/90 interface is plotted against the logarithm of the distance from the transverse crack tip in Fig. 4.3. It is seen that by using different crack tip nodal spacing, the convergence of the shear stress near the crack tip can be evaluated. For a spacing of $\Delta a = 0.025t$ (t being a single ply thickness), the semi-log plot of the shear stress τ_{yz} is almost a straight line; the slope of the line is nearly -0.5. This agrees with the commonly accepted notion that the stress singularity at a crack tip in an isotropic medium is associated with $1/\sqrt{r}$.

Similarly, the calculated energy release rates G_I for a transverse crack growing in the $[\pm 25/90_n]_s$ laminates are plotted against the increment crack length $\Delta a/nt$ in Fig. 4.4. Here, it is seen that for $\Delta a = 0.05t$, the calculated G_I reaches almost 99% the converged value (using $\Delta a = 0.025t$). Apparently, the numerical convergence of G is faster than the crack-tip stress, Fig. 4.5. This is due to the fact that G is calculated from the nodal forces and displacements, while the stress is calculated from the first derivatives of the nodal displacements.

Use of a nodal spacing $\Delta a = 0.050t$ is sufficient for purpose of experimental correlation of the fracture processes discussed in this study. It should be noted that, the single ply thickness of the material is nominally $t = 0.0052"$, Eq. (3.2). Then, $\Delta a (= 0.05t)$ is in the order of 250×10^{-6} inch, which is about 2-3 times the graphite fiber diameter. Thus, the choice of Δa is probably the limit for which the assumption of "ply-elasticity" remains valid.
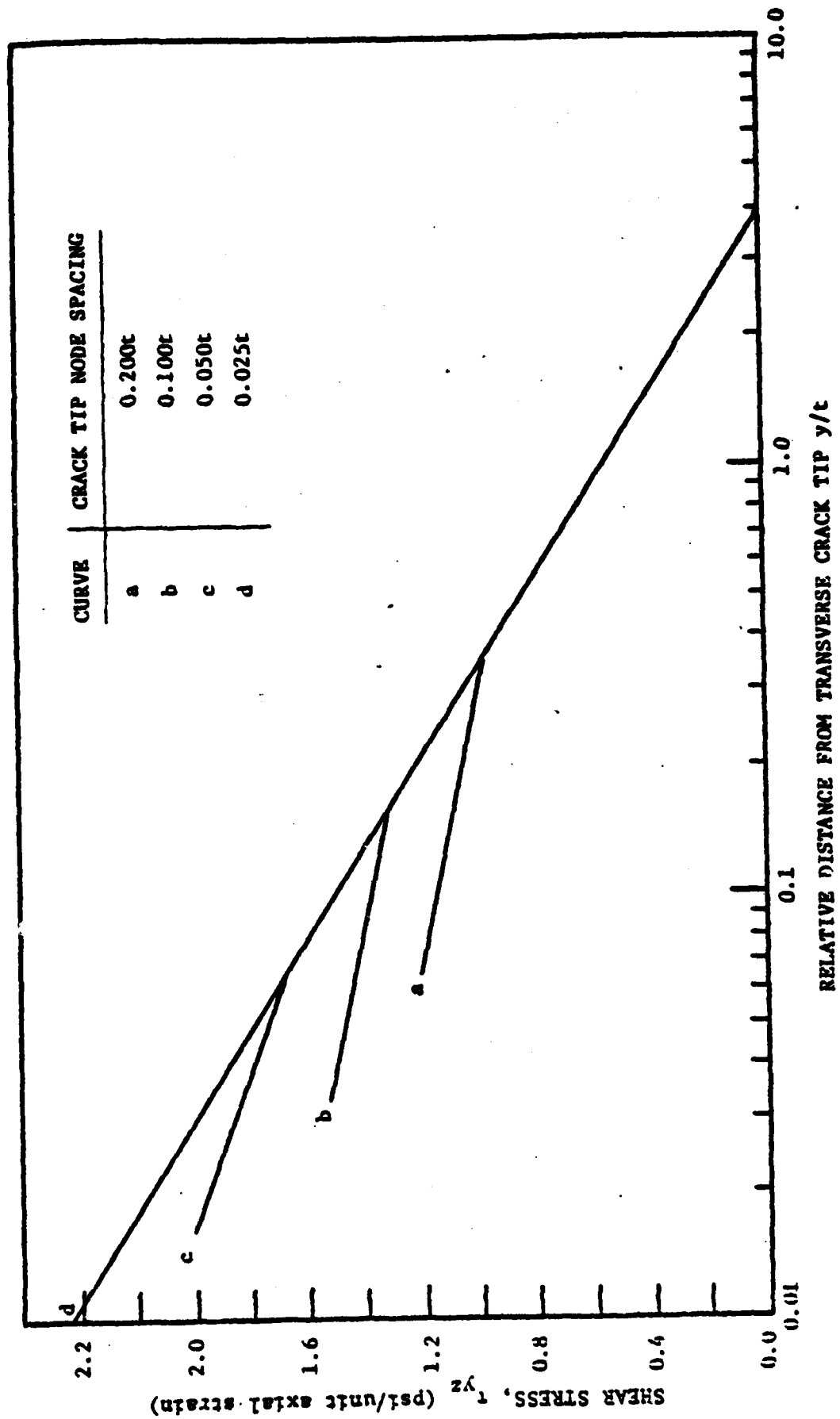
Figure 4.3 Interlaminar Shear Stress Distribution of a $[\pm 25/90_1]_s$ Laminate for Mesh Analysis.
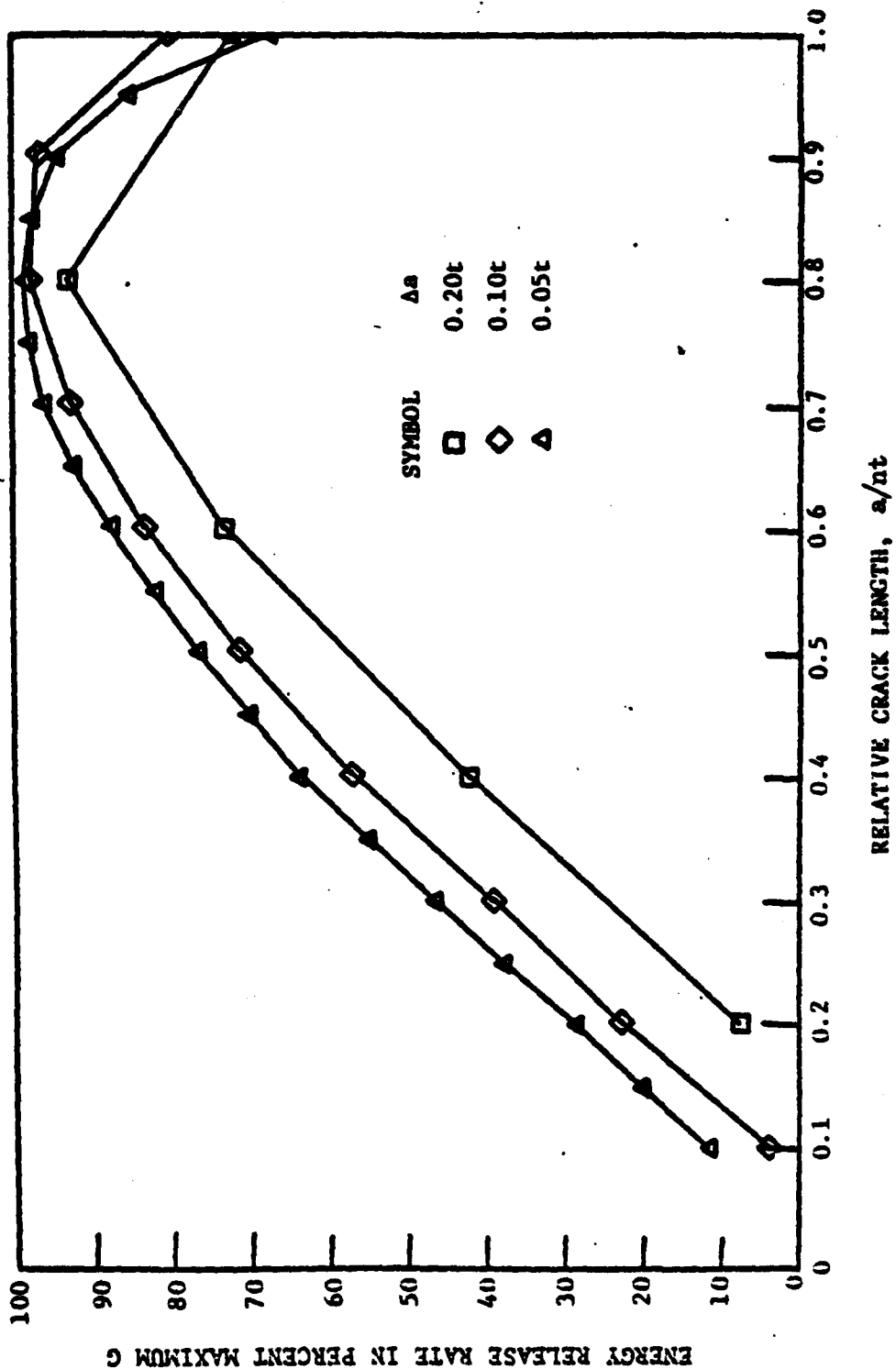
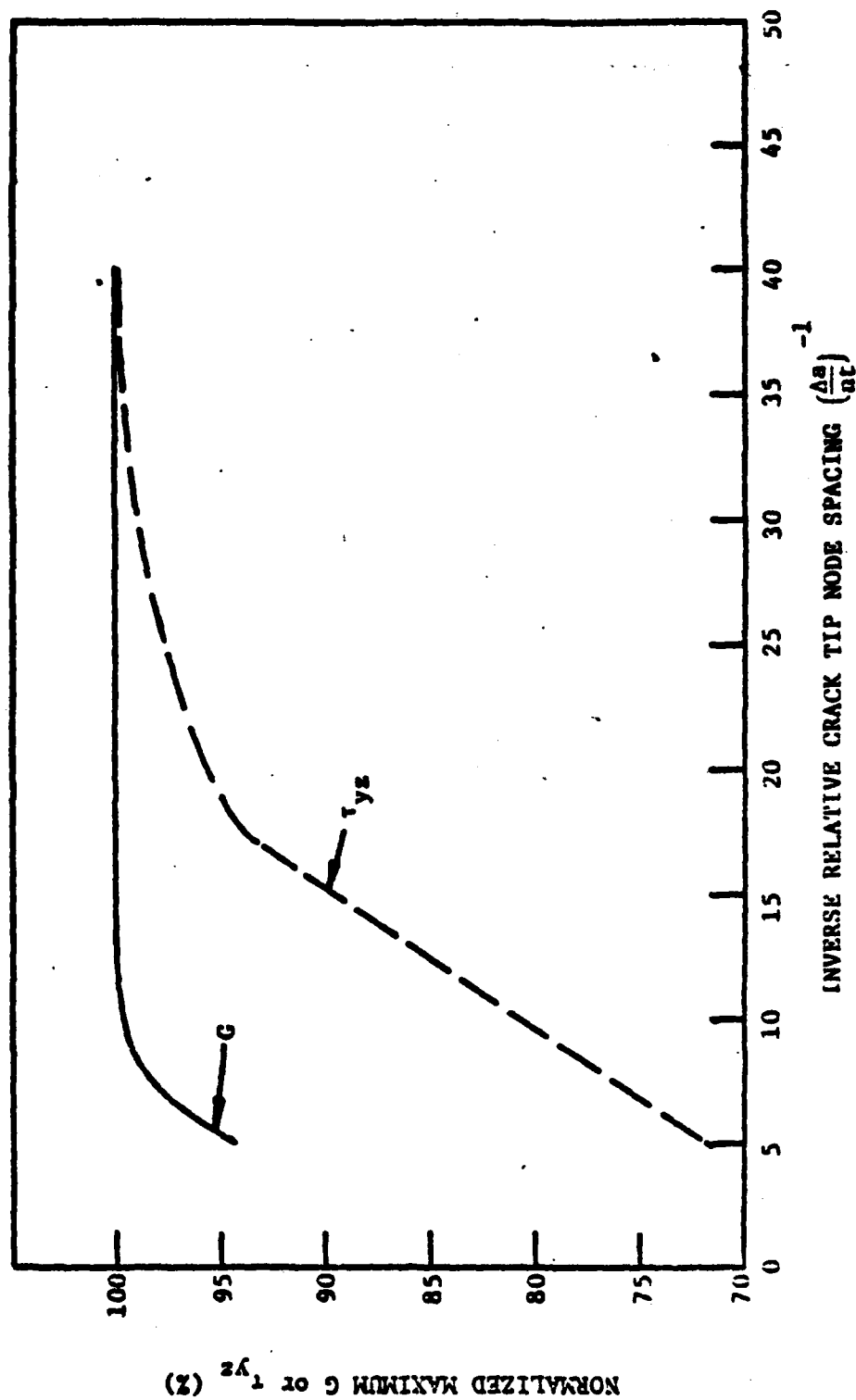Figure 4.4 Energy Release Rate vs. Crack Length for Transverse Crack Mesh Analysis.

105

Figure 4.5 Convergence of the Energy Release Rate and the Interlaminar Shear Stress.

106

4.4 Correlation with the $[0/90_n/0]$-Family

Recall in the experiment that laminates of the form $[0/90_n/0]$, $n = 1,2,3,4$ and $[0_2/90_{2n}/0_2]$, $n = 1,2$ were tested under uniaxial tension under room temperature condition. The $[0_2/90_{2n}/0_2]$ laminates were also tested under varying test temperatures. In all cases, except $[0/90/0]$, transverse cracks in the 90°-layer were recorded before final laminate failure. Experimental results obtained in this test series have been summarized and tabulated in Table 3.2, Section III.

According to the finite element simulation procedures discussed previously for the growth of transverse cracking, energy release rate coefficient functions are generated for each type of laminate in this series. The material constants for the basic material ply used in the calculation are given in Eq. (3.1) in Section III. Figs. 4.6, 4.7 and 4.8 display the coefficient functions C_e, C_{eT} and C_T, respectively for the $[0/90_n/0]$ series.

In order to use the coefficient functions for predicting the initiation of transverse cracking in these laminate, it is necessary to define, at the outset, the fracture quantities G_{Ic} and a_0.

As has been already discussed earlier, transverse cracking in the 90°-layer is of mode-I fracture. The associated material resistance G_{Ic} must be determined experimentally in a manner analogous to the cracking process itself. The experiment discussed in Section 3.3(d), however, was not appropriate for simulating transverse cracking. Rather, it determined the G_{Ic} value for cracking similar to 0°/0° delamination. In that case, it was found that $G_{Ic} \sim 0.9$ in-lb/in^2.

107

William [12], who used the AS-3502 graphite-epoxy system, found that G_{Ic} for $0°/0°$ delamination cracking was in the range of 0.8 to 0.92 in-lb/in^2, and G_{Ic} for $90°/90°$ delamination cracking was in the range of 1.2 to 1.4 in-lb/in^2. The latter simulates more closely with the transverse cracking process discussed here.

Since the T300/934 material system used in this test series is very similar to the AS-3502 system used by Williams [12], we shall use the value $G_{Ic} = 1.3$ in-lb/in^2 for all transverse cracking simulations conducted in this study. Thus,

$$G_{Ic} = 1.3 \text{ in-lb/in}^2 \qquad (4.21)$$

As for the quantity a_0, it is much more difficult to determine experimentally. Recall that the definition of a_0 must be viewed at the macroscopic level and in the sense of the Griffith's original problem (see discussion in Section II). It represents some effective flaw interior to the $90°$-layer with a size of $2a_0$.

Again, in the experiment discussed in Section 3.3(d), where specimens of double-side notches were tested, on the basis of the experimental strength of the $[90_8]$ specimens, it was suggested that the specimen had an effective side notch of size $a_0 = 2.5$ times the ply thickness (ply thickness = 0.0052"). This a_0 value is associated with specimens having cut edges; man-made flaws along the edge may have contributed greatly to the size a_0.
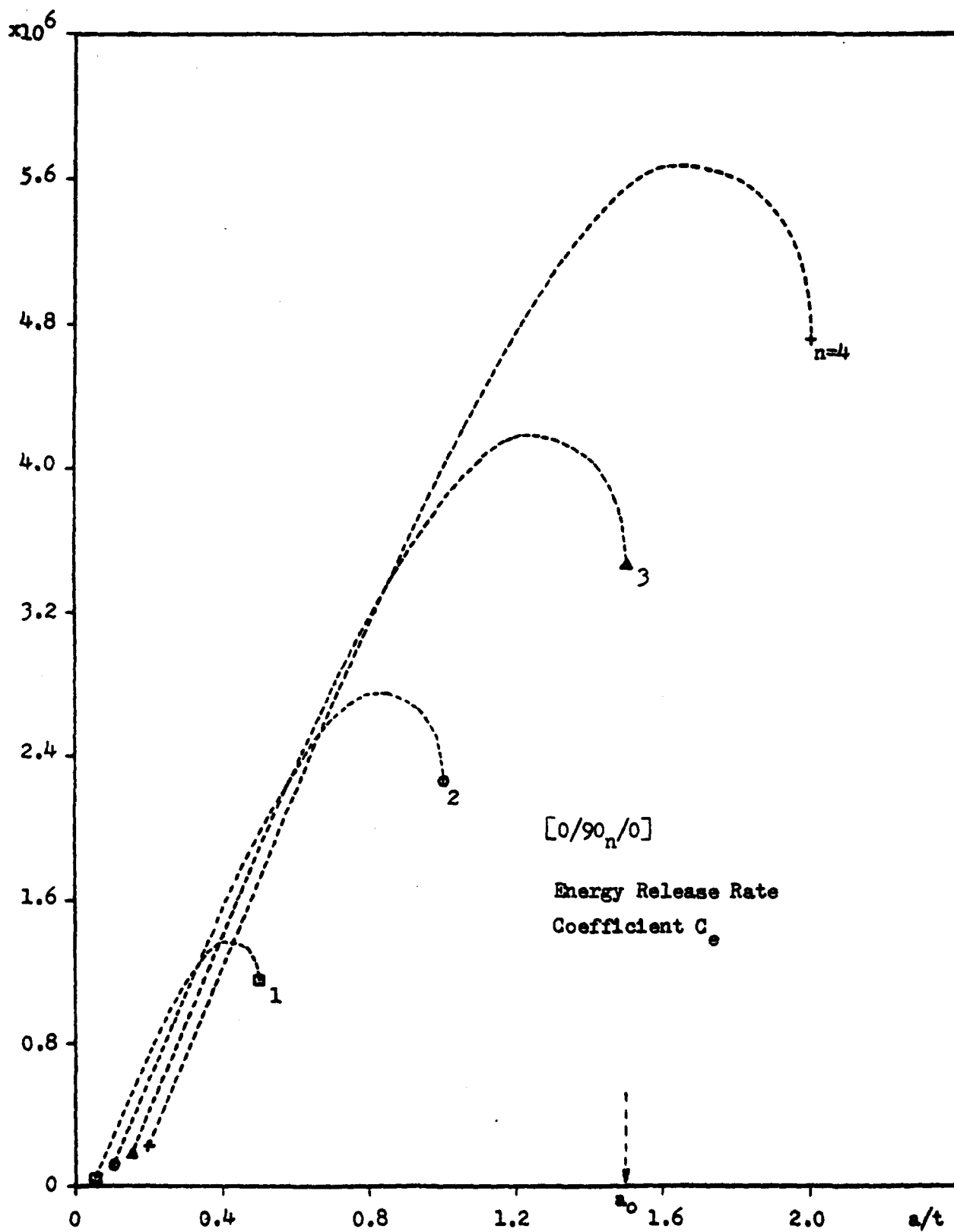
Figure 4.6   Energy Coefficient Functions C_e for Transverse
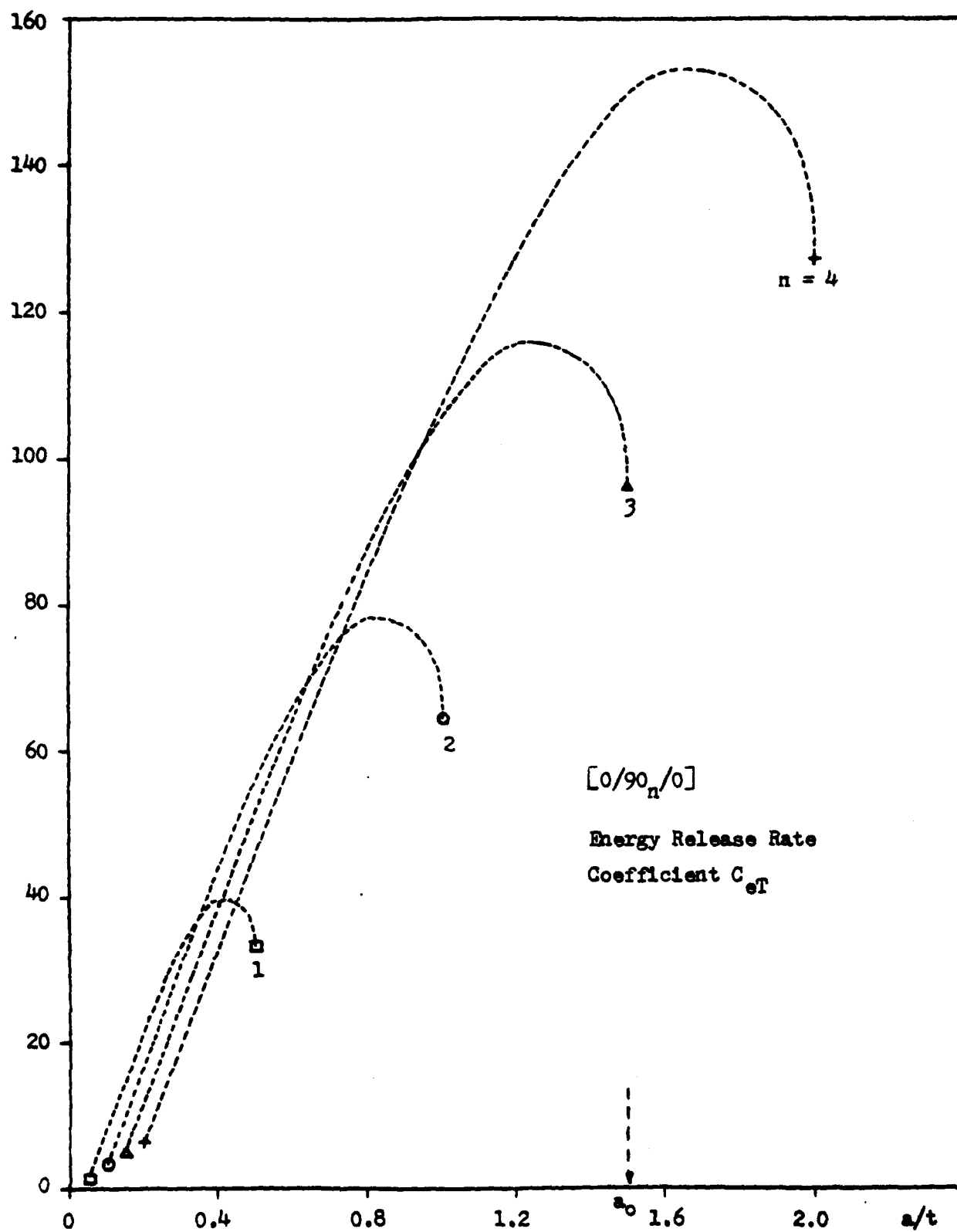Cracking in $[0/90_n/0]$ Laminates.

109

Figure 4.7   Energy Coefficient Functions C_{eT} for
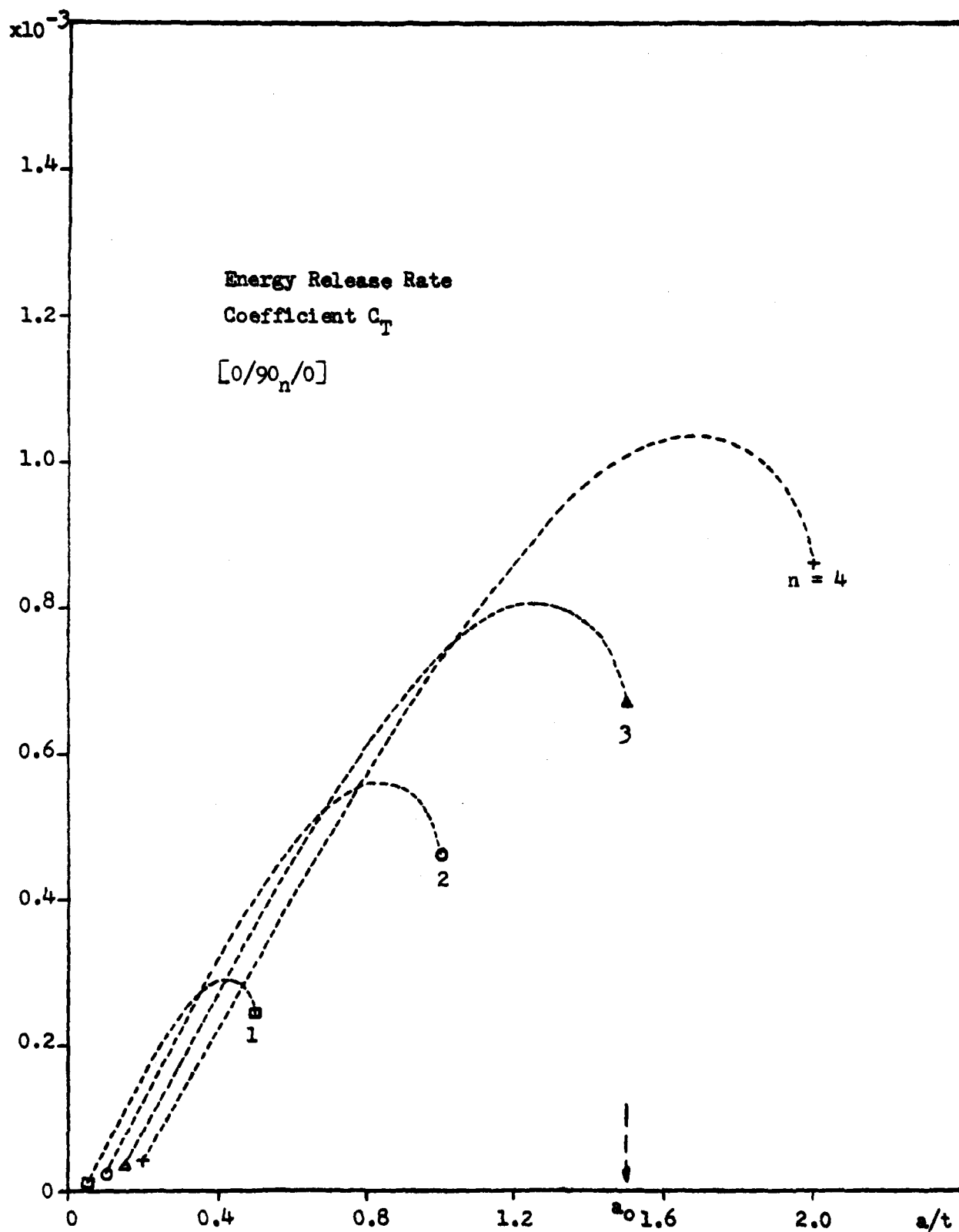Transverse Cracking in $[0/90_n/0]$ Laminates

Figure 4.8 Energy Coefficient Functions C_T for Transverse
Cracking in [0/90$_n$/0] Laminates

In the case where the 90°-layer without edges (the Griffith problem), or its edges are constrained from cracking, it is believed that the effective flaw should be much smaller. Thus, without a direct experimental determination, we shall assume here that if the thickness of the 90°-layer is unbounded, an interior flaw of size $2a_0 = 3t$ exists, which determines the unstable mode-I crack propagation of the 90°-layer under tension. Or, alternatively, the quantity a_0 associated with the transverse cracking simulation is defined as

$$a_0 = 1.5 t \qquad (4.22)$$

t being one ply thickness (equal 0.0052").

With G_{Ic} and a_0 defined, the prediction of the onset of transverse cracking in this series of tests are presented in the following.

Consider first the laminate [0/90/0], n = 1. The total thickness of the 90°-layer is only t = 0.0052". Any inherent flaws in the thickness direction cannot be more than 0.0052" in size, but can be anything smaller than t. Thus, for all possible sizes, the largest possible energy release rate is associated with $a_m \sim 0.4t$, see Fig. 4.6. The energy release rate coefficients C_e, C_{eT} and C_T at $a = a_m$ are found from, respectively, Figs. 4.6, 4.7, and 4.8:

$$C_e(a_m) = 136 \times 10^4; \quad C_{eT}(a_m) = 39; \quad C_T(a_m) = 2.9 \times 10^{-4}.$$

Then by means of Eq. (2.30), the maximum available energy release rate for transverse cracking is

$$G(a_m) = [C_e(a_m)\bar{e}_x^{\,2} + C_{eT}(a_m)\bar{e}_x^{\,2}\Delta T + C_T(a_m)\Delta T^2]t \qquad (4.23)$$

112

And, according to the criterion for initiation, Eq. (2.32), onset of transverse cracking is defined by

$$G(a_m) = G_{Ic} \qquad (4.24)$$

Using the prescribed values of $G_{Ic} = 1.3$ in-lb/in^2, $t = 0.0052''$ and $\Delta T = T_0 - T_{test} = 300° - 75° = 225°F$, we calculate from (4.23) and (4.24) the onset laminate strain $\bar{e}_x$,

$$\bar{e}_x = 1.03\%.$$

The calculated laminate modulus E_x is 14.55 msi. Hence, the onset laminate stress $\bar{\sigma}_x$ is

$$\bar{\sigma}_x = 150 \text{ ksi.}$$

Similarly, onset strains for the $[0/90_2/0]$ and $[0/90_3/0]$ laminates can also be found using the maximum strain energy release rate at $a = a_m$: for $n = 2$, $a_m = 0.8t$, and for $n = 3$, $a_m = 1.2t$; all are smaller than $a_0 = 1.5t$. Thus, for $n = 2$

$$C_e(0.8t) = 270 \times 10^4; \quad C_{eT}(0.8t) = 77; \quad C_T(0.8t) = 5.5 \times 10^{-4}$$

for $n = 3$,

$$C_e(1.2t) = 415 \times 10^4; \quad C_{eT}(1.2t) = 115; \quad C_T(1.2t) = 8 \times 10^{-4}.$$

The predicted onset strains are

$$\bar{e}_x = 0.64\% \quad \text{for } n = 2$$
$$\bar{e}_x = 0.464\% \quad \text{for } n = 3$$

The computed laminate moduli E_x are, respectively 11.35 and 9.4 msi; hence, the respective onset laminate stresses are,

113

$$\bar{\sigma}_x = 72.6 \text{ ksi} \quad \text{for } n = 2$$

$$\bar{\sigma}_x = 43.6 \text{ ksi} \quad \text{for } n = 3.$$

In the case of $[0/90_4/0]$, $n = 4$, the total thickness of the 90°-layer is larger than $2a_0 = 3t$. Hence, the worst flaw in the thickness direction cannot be larger than $2a_0 = 3t$, Then, using the energy release rate coefficient curves in Figs. 4.6, 4.7 and 4.8, we determine

$$C_e(a_0) = 550 \times 10^4; \quad C_{eT}(a_0) = 150; \quad C_T(a_0) = 0.1 \times 10^{-2}.$$

By equating $G(a_0) = G_{Ic}$, we obtain the onset laminate strain,

$$\bar{e}_x = 0.37\%$$

With the computed laminate modulus $E_x = 8.12$ msi, the onset stress is

$$\bar{\sigma}_x = 30 \text{ ksi.}$$

The prediction for the $[0_2/90_2/0_2]$ laminates is carried out using the energy release rate coefficients found for the $[0/90/0]$ laminate. But, in this case, t takes the value of $2 \times 0.0052''$ for double plies in each of the layers. Hence, the predicted onset laminate strain is

$$\bar{e}_x = 0.63\%$$

and the corresponding stress is

$$\bar{\sigma}_x = 91.6 \text{ ksi.}$$

114

As for the $[0_2/90_4/0_2]$ laminate, the energy release rate coefficient curve for $[0/90_2/0]$ may be used. Here, the length scale t takes the value $2 \times 0.0052"$. The value of G is evaluated at $a = a_0 = 0.75t$ (because the $90°$-layer thickness is now larger than a_0). Hence, from Figs. 4.6, 4.7 and 4.8, we determine C_e, C_{eT} and C_T at $a/t = 0.75$, from the curves corresponding to $n = 2$.

$$C_e(a_0) = 260 \times 10^4; \quad C_{eT}(a_0) = 70; \quad C_T(a) = 5.2 \times 10^{-4}$$

and the calculated onset strain for transverse cracking is then

$$\bar{e}_x = 0.384\%$$

or the stress is

$$\bar{\sigma}_x = 43.5 \text{ ksi.}$$

Table 4.1 below summarizes the calculated results. Values in the parentheses indicate the corresponding experimental results. A comparison between the calculated and the experimental results is illustrated in Fig. 4.9. It is seen that the transverse cracking model not only provided the correct trend reflecting the effect of the $90°$-layer thickness on the cracking initiation, but also yielded reasonably close agreement numerically with the experiment. It should also be noted that the prediction actually gives the "minimum" load required for cracking initiation, and it is, therefore, the lower bound description.

In the calculations of the onset laminate strain or stress, it is noted that the contribution to the energy release rate from thermal curing stress is rather significant. Fig. 4.10 shows for the $[0/90_n/0]$ series, the actual proportions of G_e, G_{eT} and G_T in the total energy release rate.

It is seen that the thermal energy itself is relatively small, especially in the laminates of thin 90°-layer. On the other hand, the thermal/ mechanical coupling energy is the most dominant; it is more pronounced in the laminates with thicker 90°-layer.

Table 4.1 Summary of Calculated Results

Laminate	E_x, msi	Stress at Transverse Crack
[0/90/0]	14.55(13.9)	150(No crack), ksi
$[0/90_2/0]$	11.35(11.3)	72.6(59-71)
$[0/90_3/0]$	9.4(8.9)	43.6(44-53)*
$[0/90_4/0]$	8.1(7.9)	30 (34-44)*
$[0_2/90_2/0_2]$	14.55(13.9)	91.6(76-98)
$[0_2/90_4/0_2]$	11.35(11.2)	43.5(42-57)

* Cracks found between the load interval indicated.

Finally, for the $[0_2/90_4/0_2]$ laminates that were tested at different temperature environments, see Fig. 3.10, prediction of transverse cracking can be carried out similarly as before, except now

$$\Delta T = T_0 - T_{test} = 300°F - T_{test}.$$
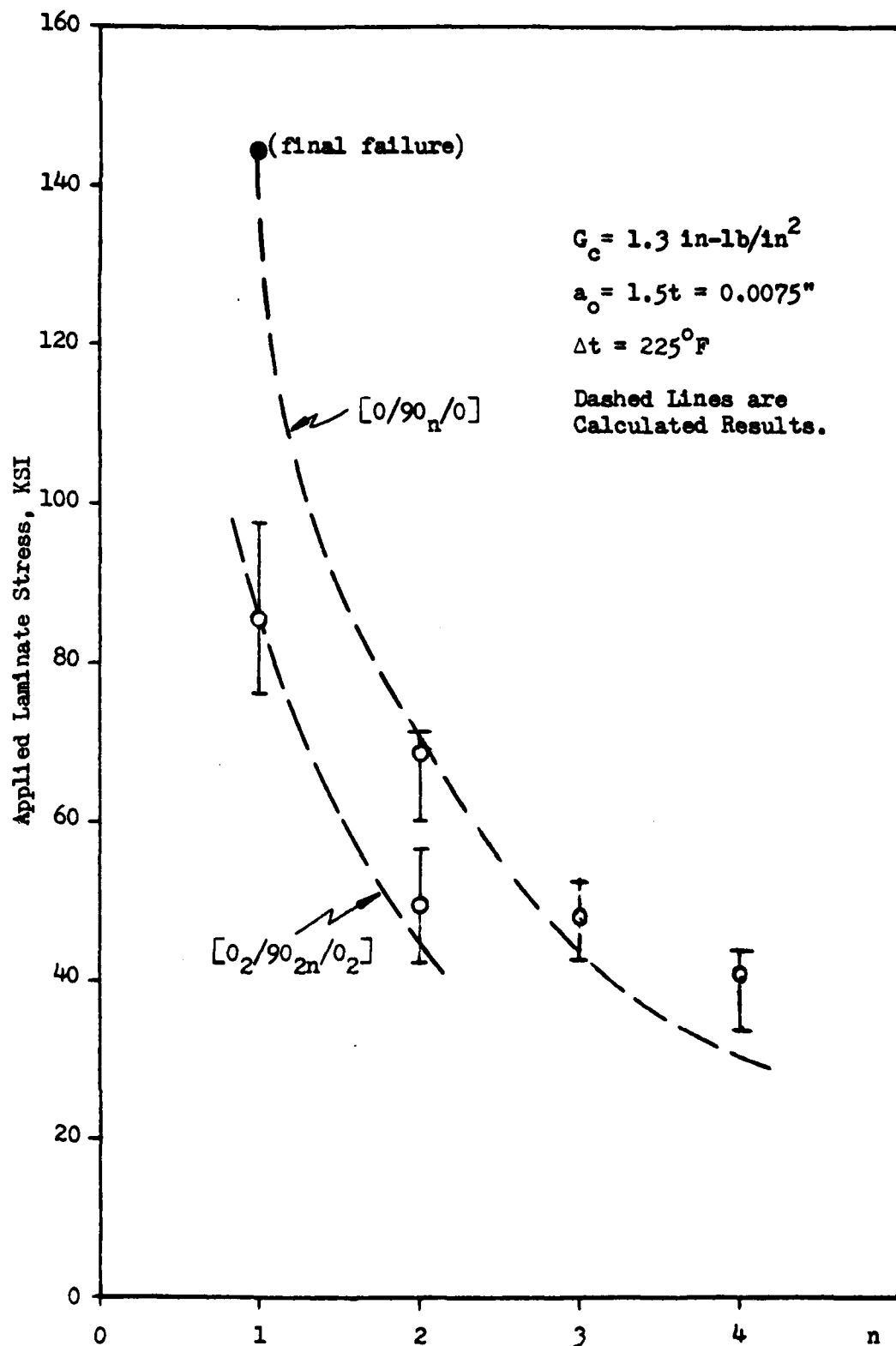
116

Figure 4.9   Comparison of the Predicted and the
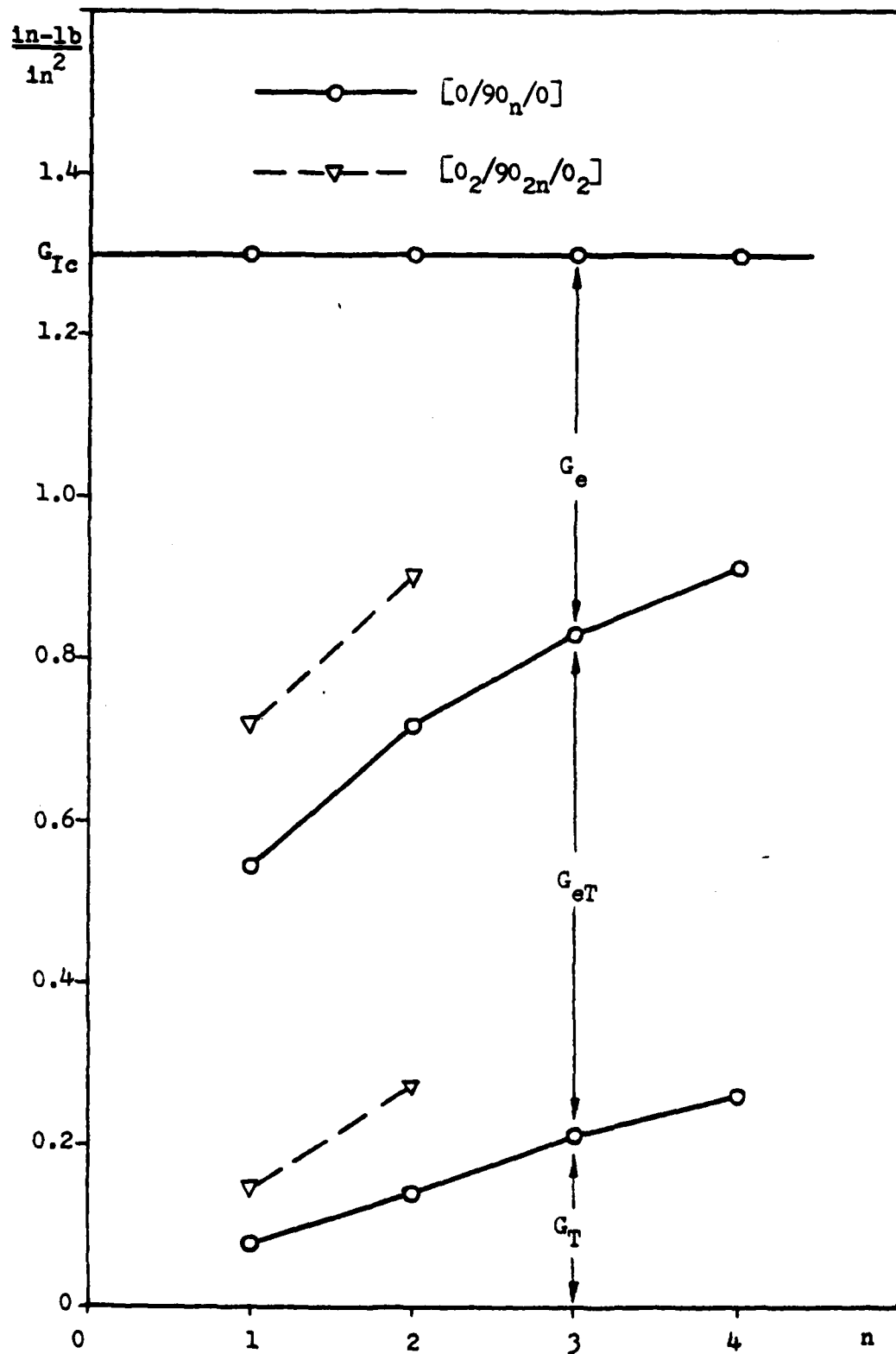   Experimental Results; [0/90n/0] Series.

117

Figure 4.10   Contribution of the Mechanical, Termal and the
Coupled Load Effects on the Total Energy Release
Rate at Onset of Transverse Cracking.

Experiments [12, 28] have suggested that the value of G_{Ic} is generally affected by temperature, that G_{Ic} increases slightly with increasing temperature and vice versa.

Lacking an experimental determination of the dependence of G_c on temperature for the T300/934 system, we shall defer this question in a latter study. However, if we use $G_{Ic} = 1.2$ and $G_{Ic} = 1.4$ in-lb/in^2, respectively in the calculation, a narrow band is obtained for the onset laminate stress (at transverse cracking) as a function of the test temperature, Fig. 4.11. It is seen that the experimental results generally lie within the band, except at higher temperature. The latter suggests that the material G_{Ic} value may actually be larger than 1.4 in-lb/in^2 at temperature $> 120^{\circ}C$.

4.5 Correlation with the $[\pm 25/90_n]_s$-Family

In the experimental study on the $[\pm 25/90_n]_s$ family, it is recalled that several different cracking modes occurred in the laminates. The sequence of occurrence of the various cracking modes was found to depend on the thickness of the 90°-layer, or the parameter n. In order to model these crack growth events, we shall consider separately the onset of transverse cracking and the onset of delamination that occur in the laminate series.

(a) <u>Prediction for Onset of Transverse Cracking</u>. For the $[\pm 25/90_n]_s$ series, the transverse cracking mechanisms are identical to the $[0/90_n/0]$ laminates that were discussed previously. The finite element simulation of the crack provides the energy release rate coefficients C_e, C_{eT} and C_T for each value of n($= 1/2,1,2,3,4,6,8$). These coefficient curves are plotted as a function of the crack length a/t, t being the thickness of a single ply (0.005"), Figs. 4.12, 4.13 and 4.14. It is seen that these curves are similar to those shown in Figs. 4.6, 4.7 and 4.8 for the $[0/90_n/0]$ series.
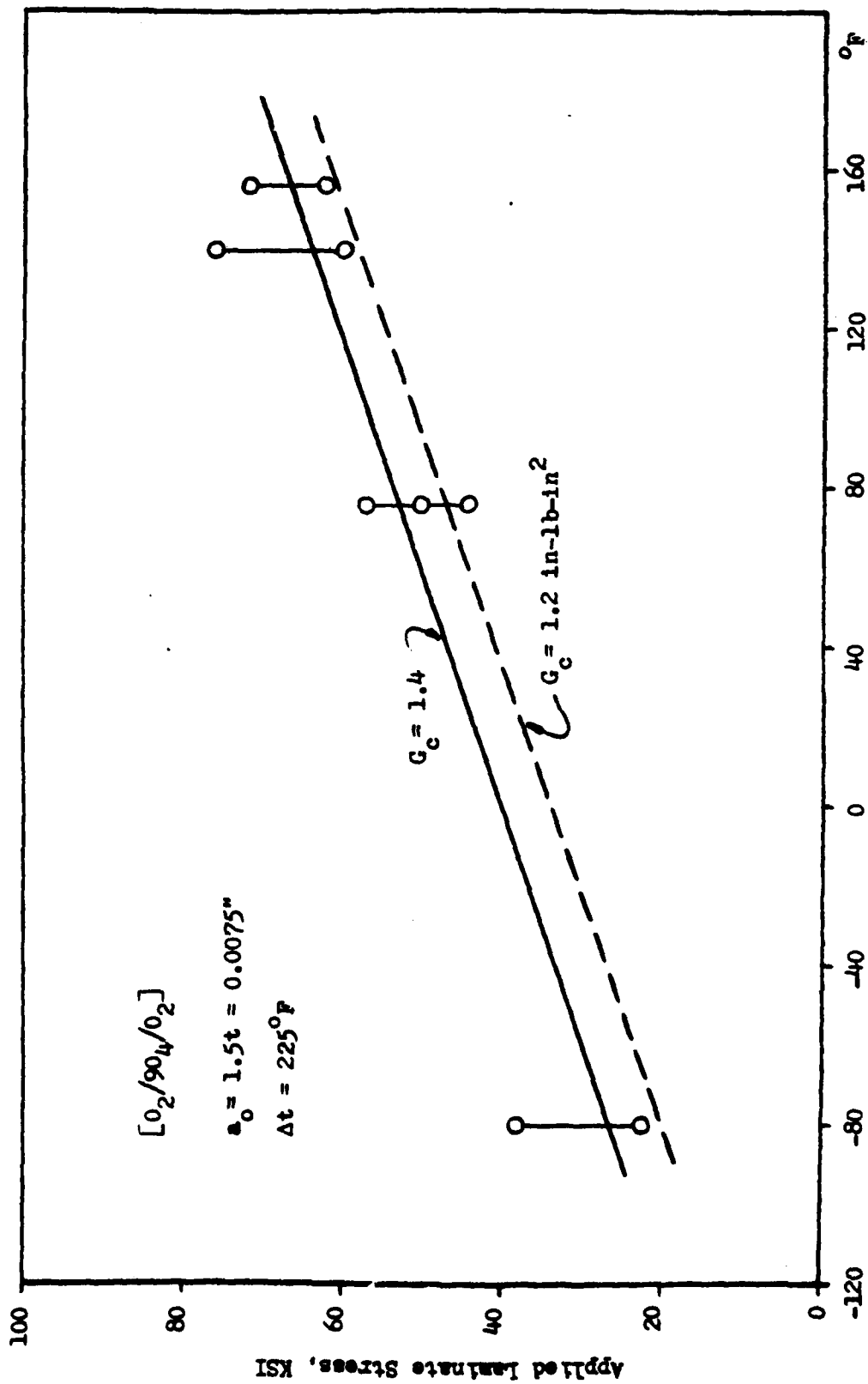
119

Figure 4.11 Comparison of the Predicted and the Experimental Results, $[0_2/90_4/0_2]$ Laminates
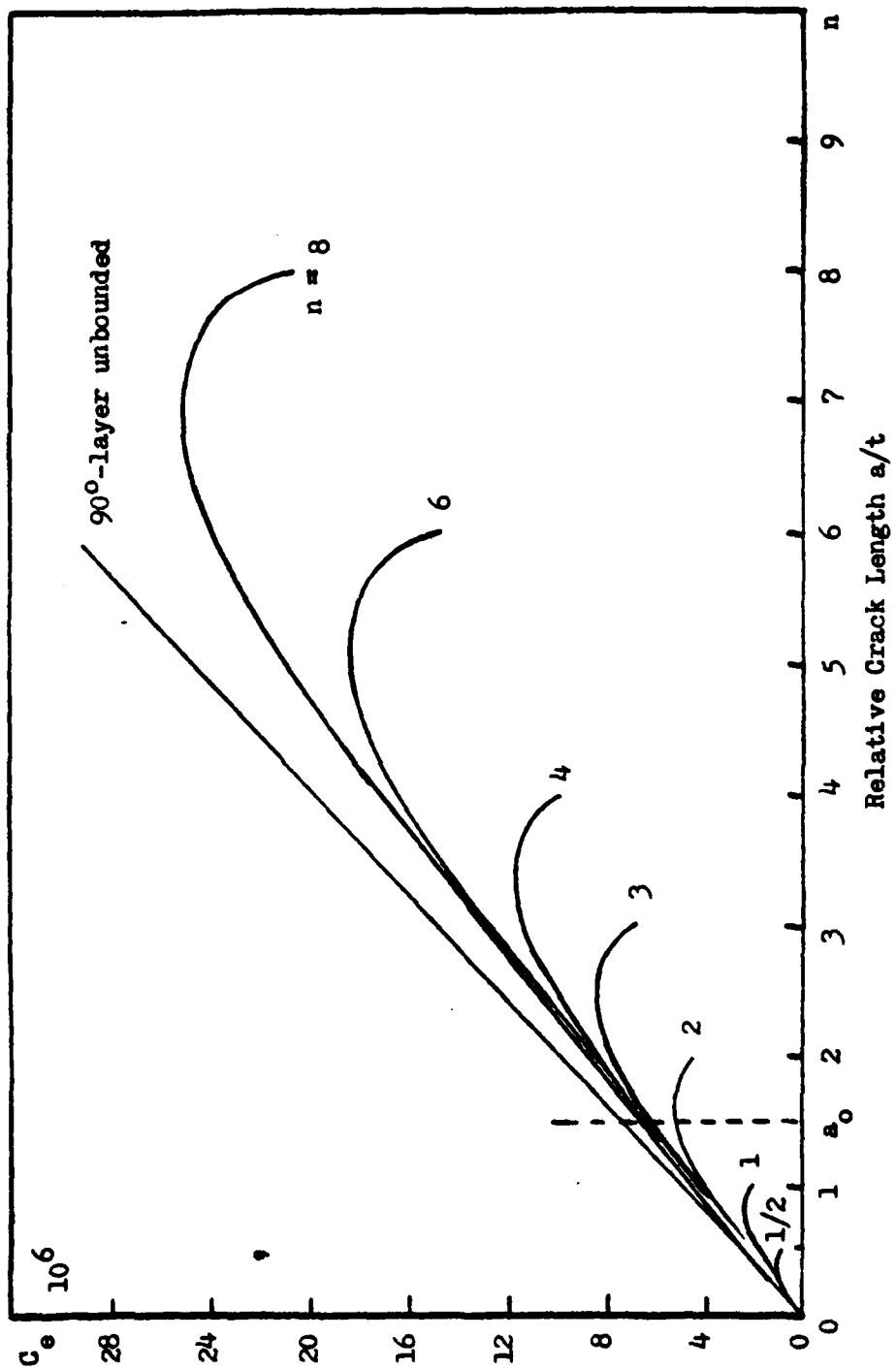
Figure 4.12   Mechanical Load Energy Release Rate Coefficient for Transverse Cracking in the $[\pm 25/90_n]_s$ Laminates.
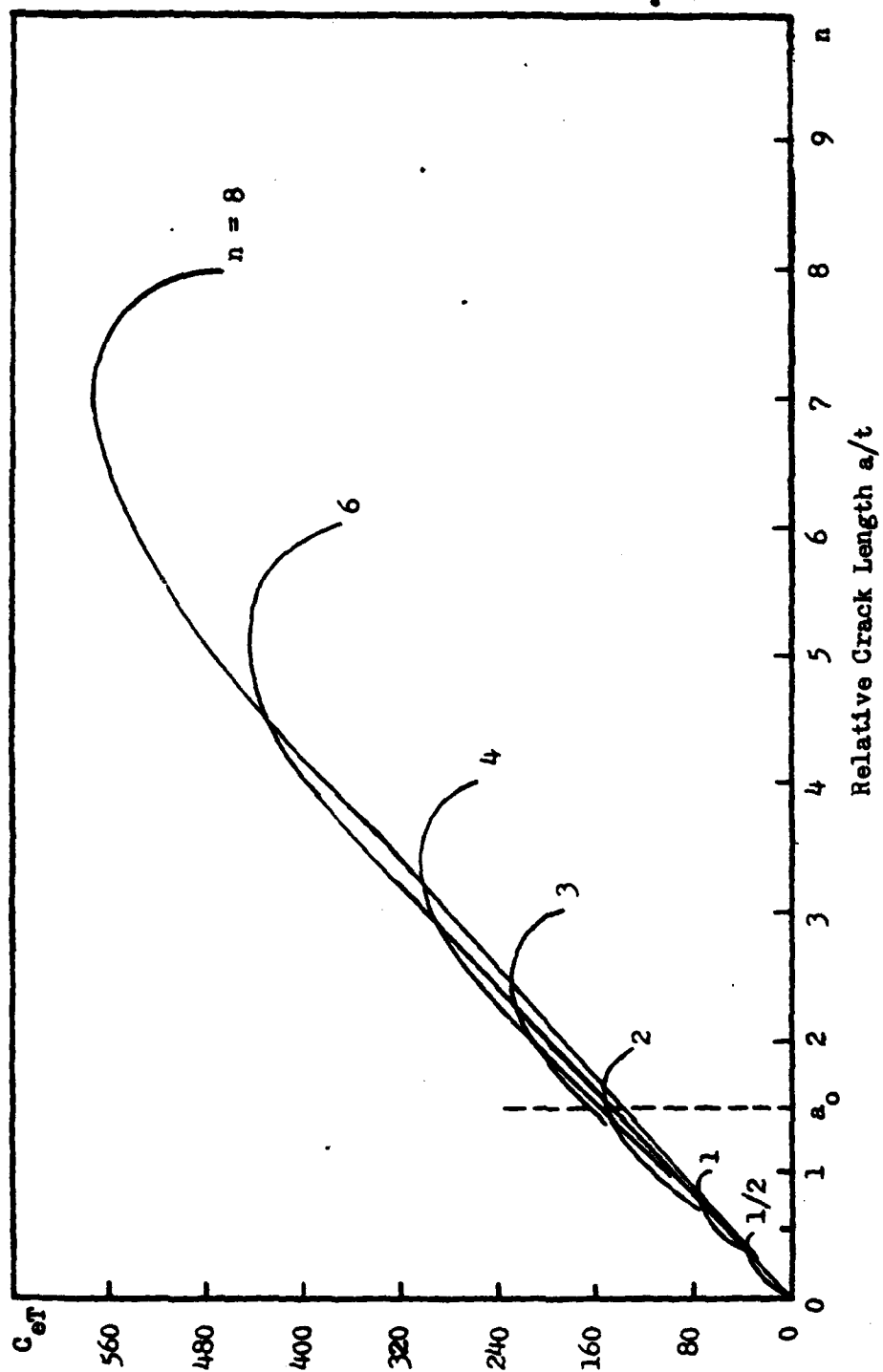
Figure 4.13 Coupled Mechanical/Thermal Energy Release Rate Coefficient for Transverse Cracking in the $[\pm 25/90_n]_s$ Laminates.
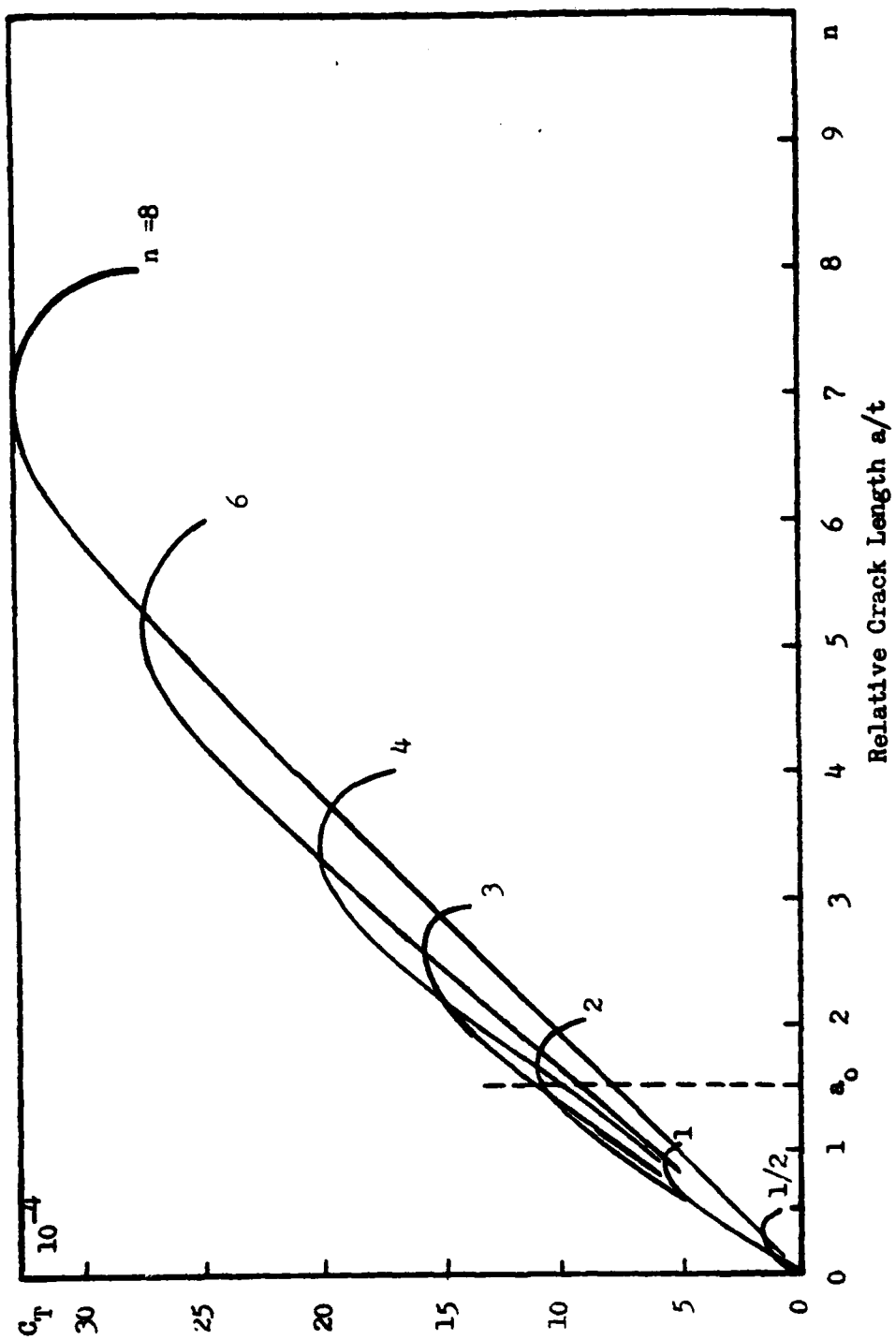
Figure 4.14 Thermal Load Energy Release Rate Coefficient for Transverse Cracking in the $[\pm 25/90_n]_s$ Laminates.

123

To predict the onset of transverse cracking for this series of laminates, we shall use the same material constants as before. Namely, $\Delta T = 225°F$, $a_0 = 1.5t = 0.0075"$ and $G_{Ic} = 1.3$ in-lb/in^2. Table 4.2 below summarizes the appropriate values for C_e, C_{eT} and C_T used in the calculation, and the calculated onset laminate strains for transverse cracking in the series.

Table 4.2 Summary of Calculated Results for
Onset of Transverse Cracking

$[\pm25/90_n]_s$	C_e, x 10^6	C_{eT}	C_T, x 10^{-4}	$\bar{e}_x$, %
n = 1/2	1.0	41	2.1	1.14
1	2.5	75	6.1	0.66
2	5.4	140	10.5	0.38
3	5.7	161	10.9	0.352
4	6.0	154	9.5	0.36
6	6.4	148	8.5	0.363
8	6.5	140	7.5	0.378
$[\pm25_2/90_2]_s$	2.45	73	6.0	0.375*

* Use t = 2 x 0.0052"

In the above table, it is seen that the thermal/mechanical coupling effect is largest in the case of n = 3. Hence, the predicted onset laminate strain for transverse cracking is also the lowest. Also, in the cases of n = 1/2 and 1, the calculated onset laminate strain are large, because of

the available energy release rates are small. In fact, for these two cases, there was no transverse crack found in the experiment (instead, free edge delamination occurred). These calculated results are graphically displayed in Fig. 4.15 along with the corresponding experimental values found in Section III. It is noted that the comparison between the prediction and the experiment is exceptionally close, not only in the trend, but also in the actual numerical value.

(b) <u>Prediction for Onset of Edge Delamination</u> It is recalled in the experiment (Section III) that edge delamination was observed prior to final failure in each of the laminates in the $[\pm 25/90_n]_s$ series. The observed edge delaminations generally occurred at loads in excess of 90% of the ultimate laminate strength; it, therefore, may be regarded as the initiator of the laminates' final failure.

In the finite element modeling, the same ply properties were used in the calculation, except (1) the appropriate critical energy release rate, whether be it G_{Ic} or mixed-mode $G_{(I,II)c}$; (2) the appropriate value for a_0 and (3) the ply properties of the 90°-layer after it had suffered transverse cracks.

As has been discussed previously, edge delamination along the mid-plane of the laminate can be modeled as mode-I crack. Experimental observations in this type of delamination, indicated that the cracked surface was similar to the crack surface of a transverse crack in the 90°-layer. Thus, for mode-I crack, the value of $G_{Ic} = 1.3$ in-lb/in^2 may be confidently used.
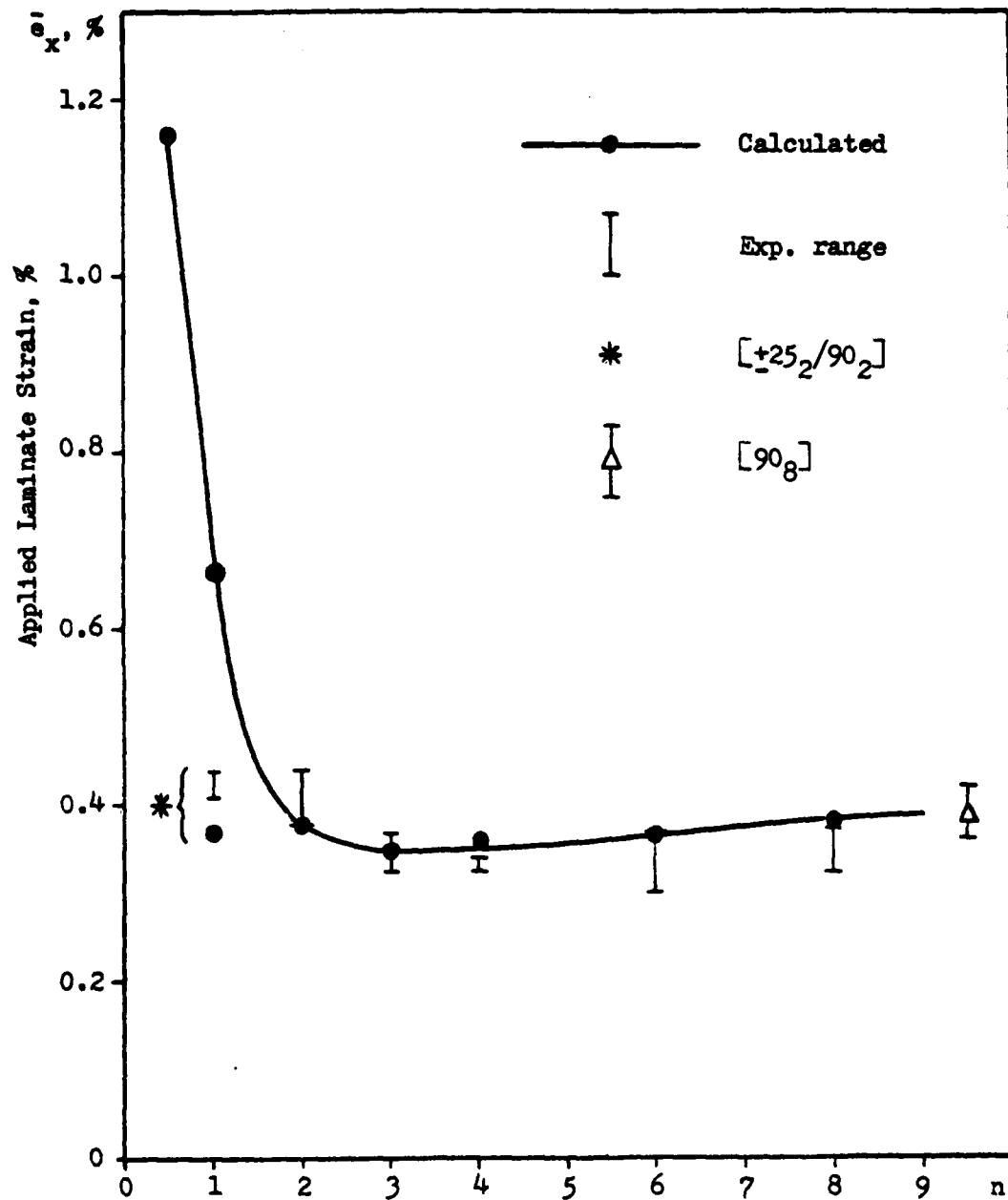
Figure 4.15 Calculated Laminate Strain at Onset of Transverse Cracking in $[\pm25/90_n]_s$ Laminates.

On the other hand, delamination along the 25/90 interface is generally in mixed-mode. As will be shown later, the calculated G_I to G_{III} ($G_{II} \sim 0$) ratio is approximately one to one for laminates $n = 3$ and $n = 4$; G_{III} is much less than G_I for $n = 2$. Referring to the experimental data discussed in Section III(d) and in particular the data shown in Fig. 3.22, the possible range of $G_{(I,II)c}$ should be

$$1.5 < G_{(I,II)c} < 2.5 \text{ in-lb/in}^2 \qquad (4.25)$$

The appropriate value for a_0 in the free edge delamination cases should be larger than 1.5t, which was used in the transverse cracking modeling. The reason is that the crack is initiated from the cut edges of the specimen, rather than from the interior as in the case of transverse cracking. In the calculations that follow, a_0 takes the value of 2t,

$$a_0 = 2t = 2 \times 0.0052" \qquad (4.26)$$

Finally, for the laminates of $n \geq 2$, multiple transverse cracks were formed in the 90°-layer before edge delamination. The ply elastic properties of the 90°-layer have obviously been degraded. An approximate estimate for the reduced 90°-layer stiffness may be determined by a backward calculation using the laminated plate theory. In the laminate series of $n \geq 2$, the following reduced property for the 90°-layer is used in the calculation:

$E_L = 21.0$ Msi	$E_T = 1.2$ Msi	$E_Z = 1.72$ Msi
$\nu_{LT} = 0.3$	$\nu_{TZ} = 0.3$	$\nu_{LZ} = 0.3$
$G_{LT} = 0.66$ Msi	$G_{TZ} = 0.35$ Msi	$G_{LZ} = 0.94$ Msi
$\alpha_L = 0.2$ $\mu e/°F$	$\alpha_T = 16$ $\mu e/°F$	$\alpha_Z = 16$ $\mu e/°F$

$$(4.27)$$

127

Note that only four moduli are affected and they are underlined. The global effect of the transverse cracks gives approximately the same reduction in the effective laminate stiffness as observed experimentally. It will be shown later that the reduction of the 90°-layer property is not sufficient to predict the onset of delamination whenever transverse cracking preceded delamination. In these cases, the interactions between the transverse cracking and delamination processes become more pronounced as has been discussed previously in Sections II and III.

Mid-Plane Delamination

Calculation for mid-plane delamination was carried out for laminates of $n = 1/2$, 1,2,3 and 4. The energy release rate coefficients associated with the mechanical, thermal, and the coupled components are calculated and shown in Figs. 4.16, 4.17 and 4.18. The general shape of these coefficient functions . increase from zero to a maximum value followed by a slow reduction in value as the crack propagates inward. This implies that once a mid-plane delamination forms, it may undergo stable crack growth. With the exception of the case of $n = 1/2$, the magnitude of these shape functions decreases as n is increased. In the case of $n = 1/2$, the total laminate is approaching the limiting case, say, of a $[\pm25]_s$ laminate, which does not delaminate at all in the assumed opening mode.

These energy release rate coefficient functions are calculated based on the assumption that delamination is the first mode of damage in the laminate and hence the full ply properties are used for all plies in the laminate.
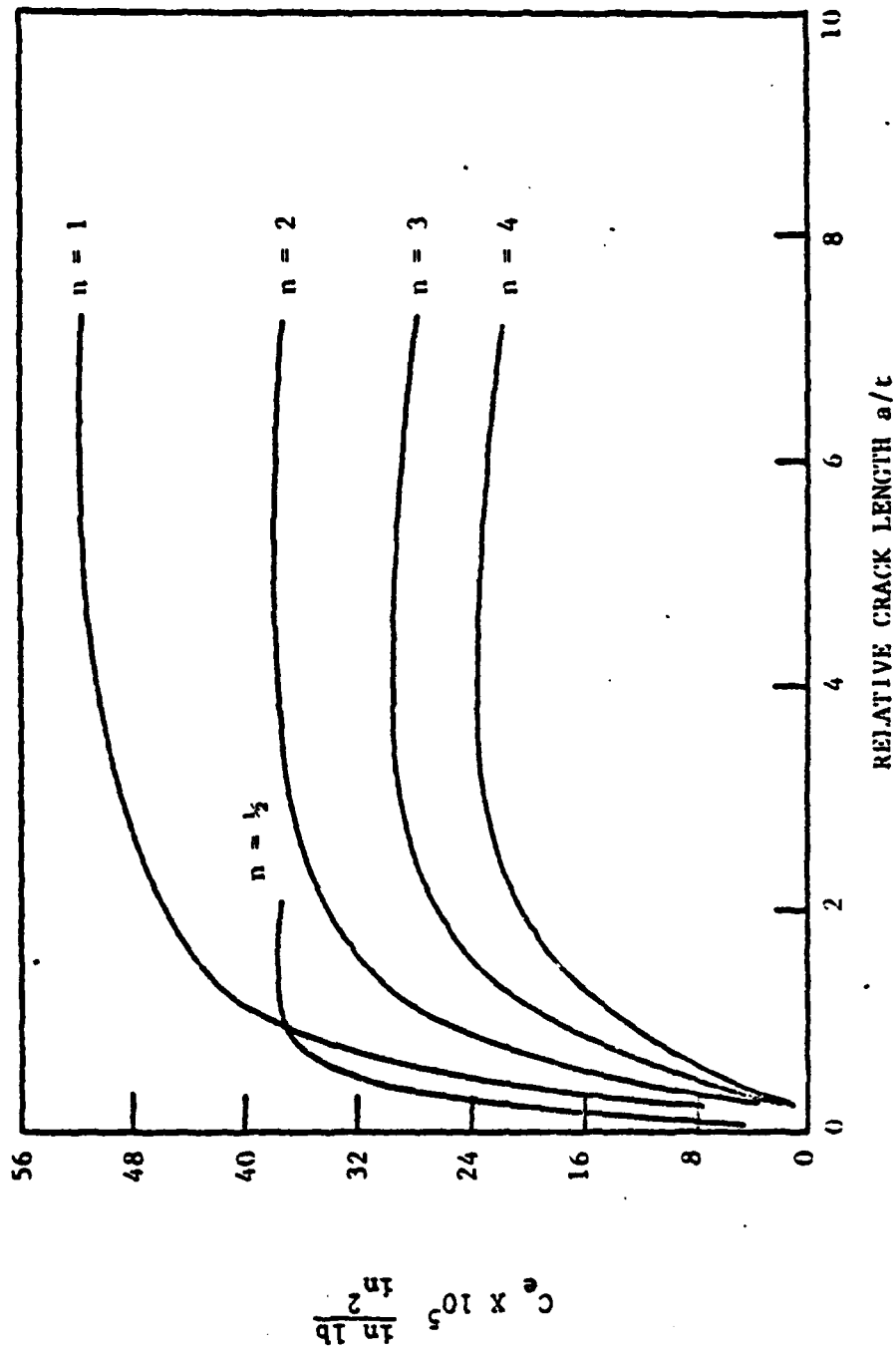
Figure 4.16 Mechanical Energy Release Rate Coefficients for Mid-Plane Delamination in the n = 1/2, 1,2,3 and 4 Laminates.
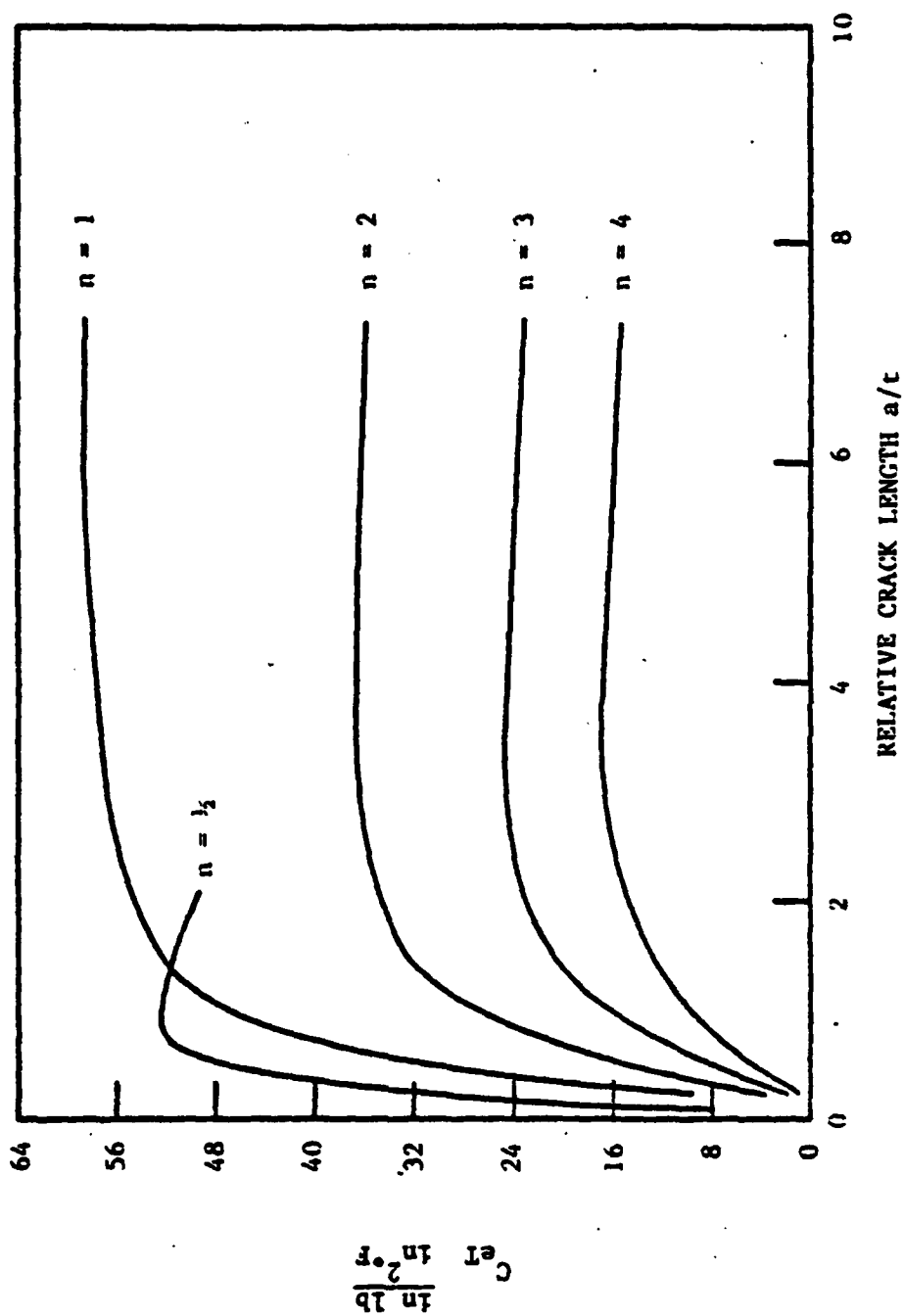
129

Figure 4.17 Coupled Thermal/Mechanical Energy Release Rate Coefficients for Mid-Plane Delamination in the n = 1/2, 1,2,3 and 4 Laminates.
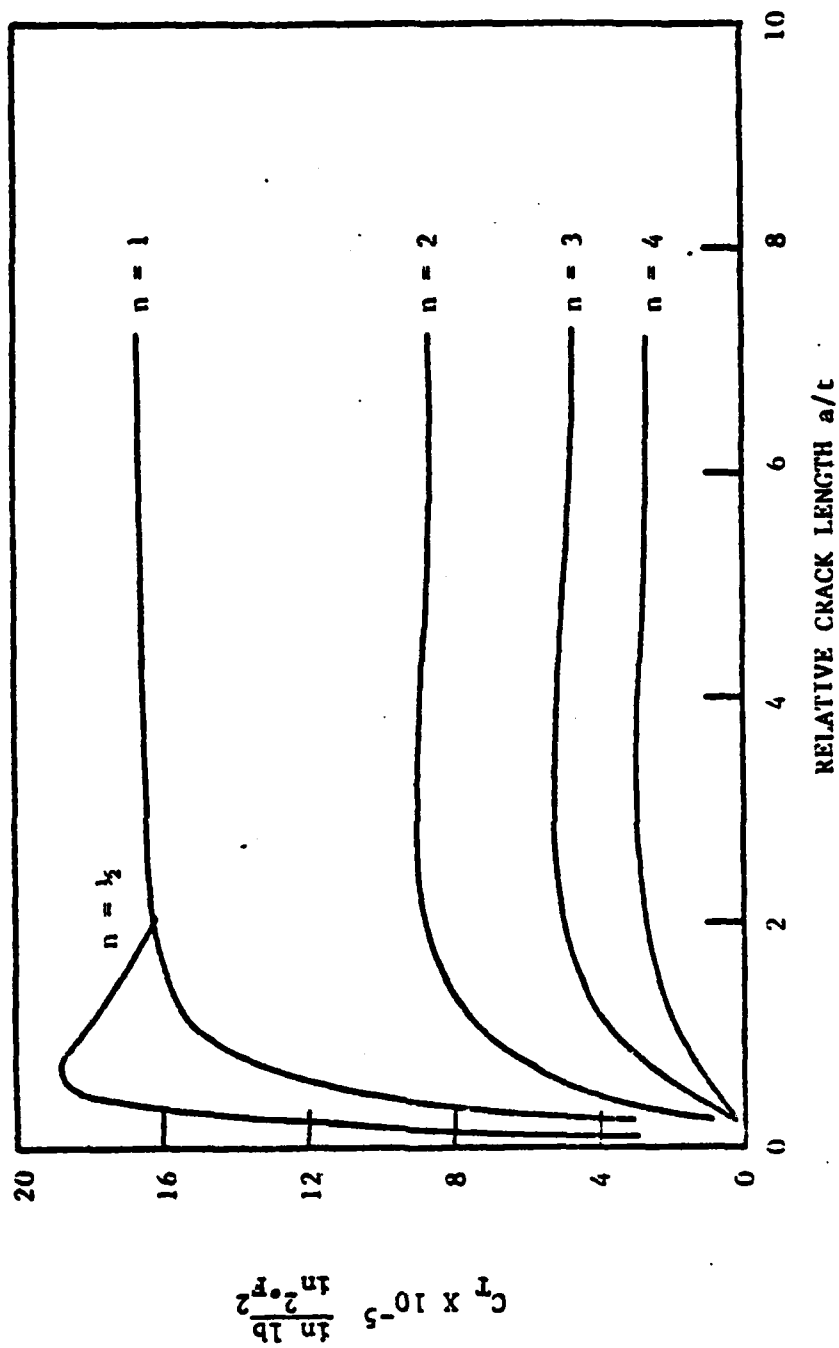
Figure 4.18   Thermal Load Energy Release Rate Coefficients for Mid-Plane Delamination in the n = 1/2, 1,2,3 and 4 Laminates.

As discussed before, edge delamination occurred after the formation of transverse cracks in the 90°-layer for those laminates of $n \geq 2$. Thus, the post-transverse cracking mid-plane delaminations are modeled a second time using the reduced effective moduli as given in equation (4.27) for the cracked 90°-layers only. The corresponding energy release rate coefficient functions for $n = 1/2$, 1,2,3 and 4 are shown in Figs. 4.19, 4.20 and 4.21 for the mechanical, thermal, and the coupled components, respectively. These coefficient functions are slightly larger in magnitude than those which do not include the effect of transverse cracking. These indicate a larger available energy release rate for delamination. Thus, the inclusion of the effect of transverse cracks in this manner will predict a lower onset load for mid-plane delamination.

For prediction of mid-plane delamination, we use $\Delta T = 225°F$ and $G_{Ic} = 1.3$ in-lb/in^2 as before; and $a_0 = 2t$ as discussed earlier. The predicted onset laminate strains for $n = 1/2$, 1,2,3 and 4 are summarized in Table 4.3. It is seen that the predicted onset strains, with or without the effect of reduced 90°-layer property (due to transverse cracks) are practically the same. Since, for the cases of $n = 1/2$ and 1, the predicted onset strain for delamination is lower than the predicted onset strains for transverse cracking (see Table 4.2), and since the predicted onset strains for delamination are larger than the onset strains for transverse crack in the cases of $n \geq 2$, the values that are underlined in Table 4.3 govern.

From Table 4.3, it is seen that the mechanical component of the energy release rate generally dominates the fracture process while the thermal energy is quite insignificant. Also, with the exception of $n = 1/2$, the onset

Figure 4.19 Mechanical Load Energy Release Rate Coefficients for Mid-Plane Delamination in the n = 1/2, 1,2,3 and 4 Laminates with Reduced 90°-Ply Properties.

Figure 4.20 Coupled Energy Release Rate Coefficients for Mid-Plane Delamination in the $n = 1/2, 1, 2, 3$ and 4 Laminates with Reduced 90° Ply Properties.

134
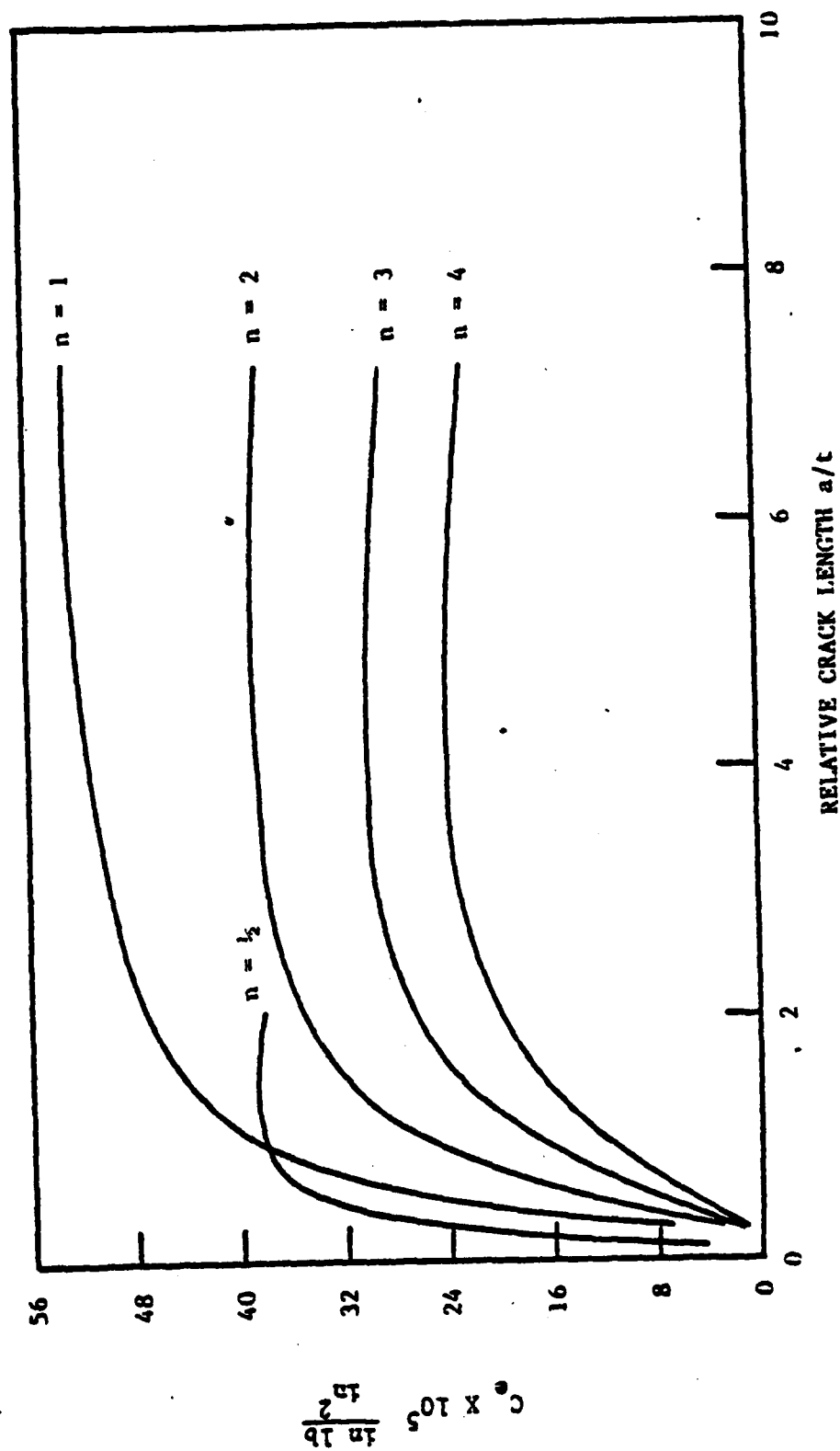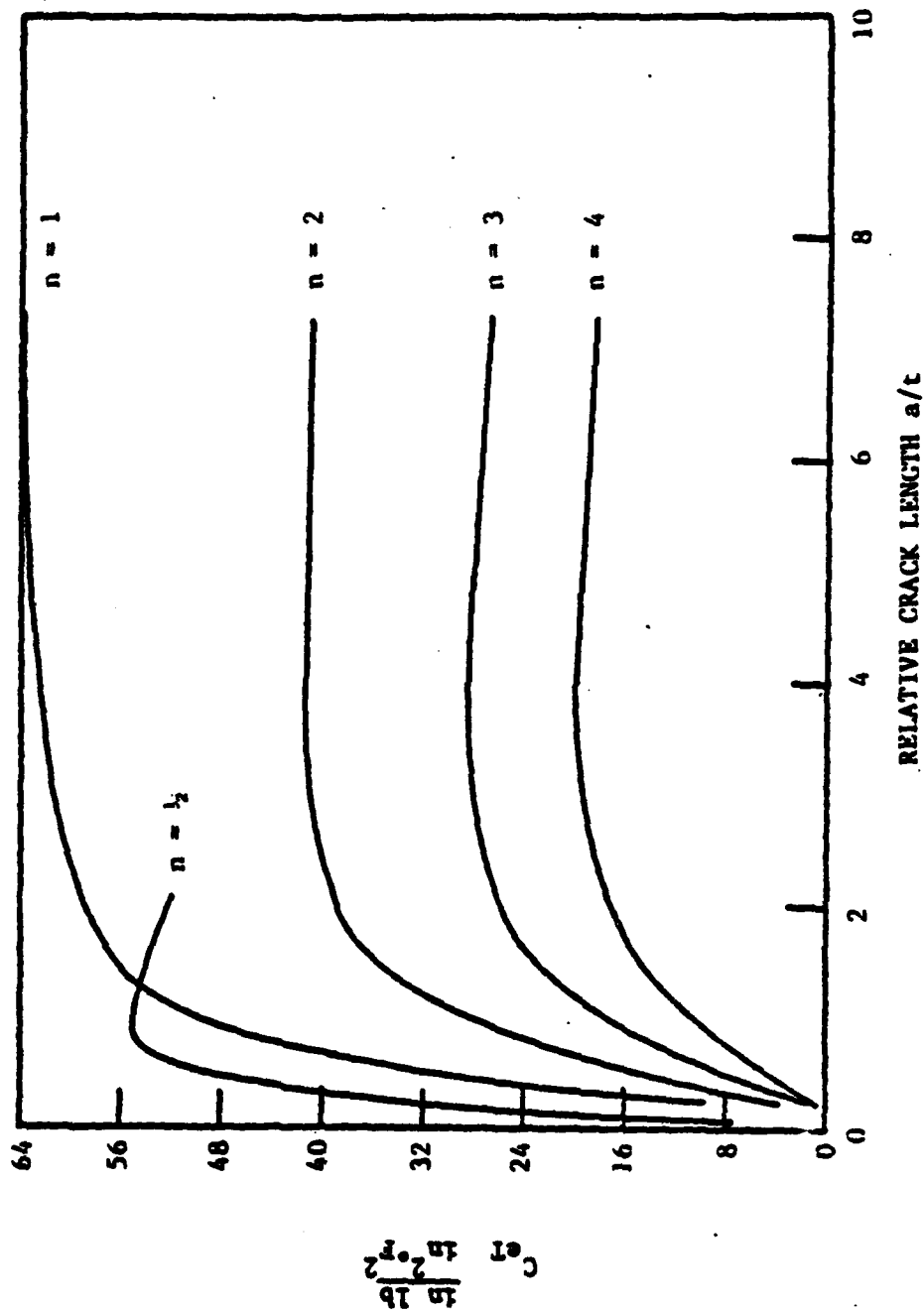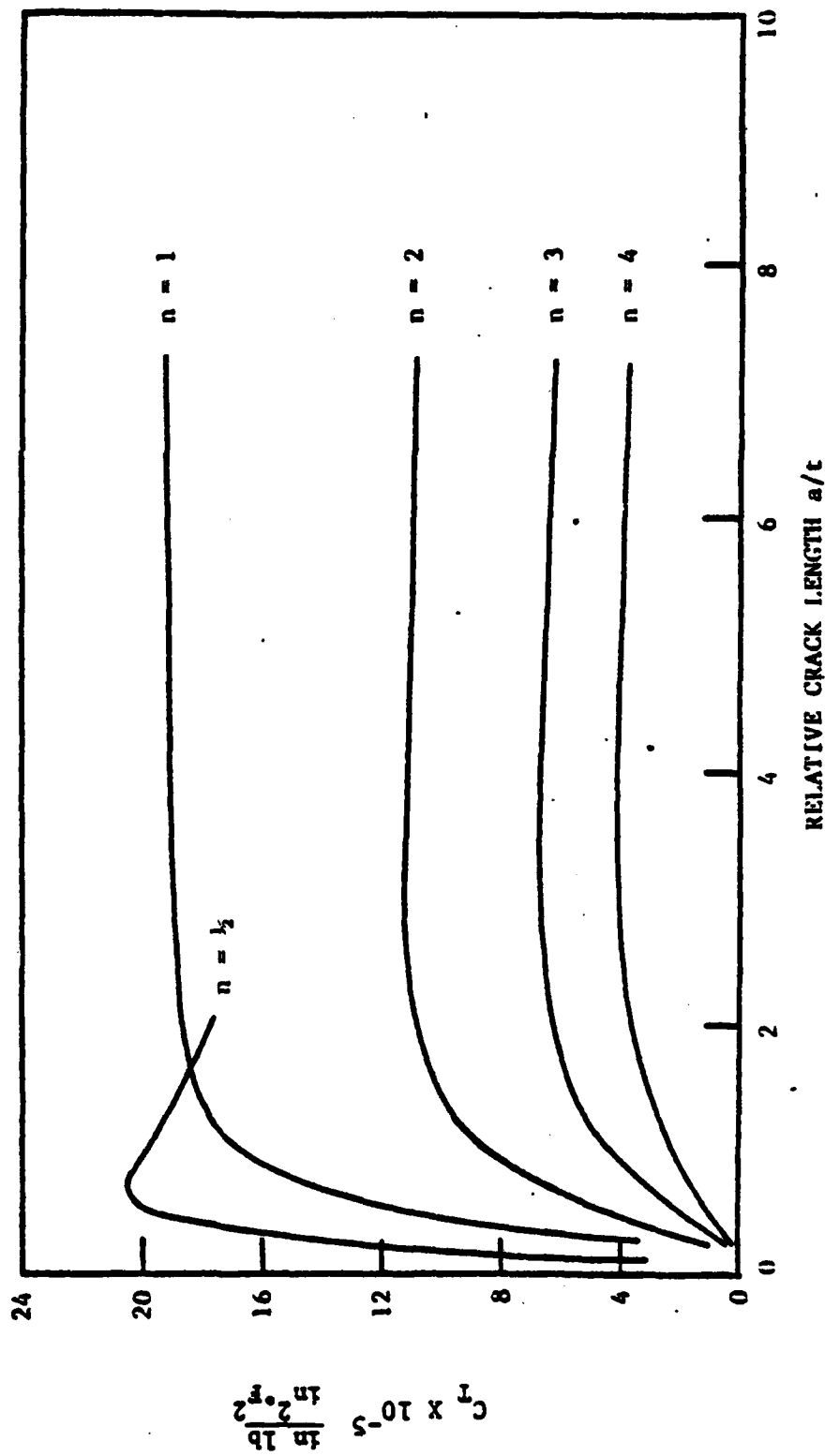
Figure 4.21 Thermal Load Energy Release Rate Coefficients for Mid-Plane Delamination in the n = 1/2, 1,2,3 and 4 Laminates with Reduced 90° Ply Properties.

Table 4.3 Calculated Critical Strain and Energy Release
Rates for Mid-Plane Free-Edge Delamination.

n	$\frac{a_o}{t}$	NO TRANSVERSE CRACKING				WITH TRANSVERSE CRACKING			
		G_e ($\%G_c$)	G_T ($\%G_c$)	G_{eT} ($\%G_c$)	$\bar{e}_x$ (%)	G_e ($\%G_c$)	G_T ($\%G_c$)	G_{eT} ($\%G_c$)	$\bar{e}_x$ (%)
½	1	64.7	3.8	31.5	0.666	65.8	3.6	30.6	0.655
1	2	67.0	3.3	29.7	0.603	65.1	3.7	31.2	0.592
2	2	75.1	1.8	23.1	0.733	72.6	2.2	25.2	0.718
3	2	81.0	1.0	18.0	0.867	78.5	1.3	20.2	0.850
4	2	85.7	0.6	13.7	1.025	83.7	0.7	15.6	1.023

laminate strain increases as the thickness of the 90°-layer also increases. This trend suggests that mid-plane delamination may not be possible when $n \geq 2$. Indeed, as will be shown next, a mixed-mode 25/90 delamination is predominant when $n \geq 2$ (this was also observed in experiment).

Mixed-mode 25/90 Delamination

The schematics of this mixed-mode crack and the finite element representation have been shown in Fig. 2.13. The energy release rate coefficients C_e, C_{eT} and C_T for the laminates of $n = 1/2, 1,2,3,4,6,8$ are calculated for the 25/90 delamination. Figs. 22, 23 and 24 show the coefficients calculated using full ply properties (no consideration of transverse cracking) for the 90°-layer. And, Figs. 25, 26 and 27 show those calculated with reduced 90°-layer properties.

For predicting the onset strains for this type of delamination, we used all the previously used material constants (ΔT, a_0, etc) except that

$$G_{(I,II)c} = 1.5 \ \text{in-lb/in}^2. \tag{4.28}$$

This quantity has been suggested as the lower bound value for mixed-mode cracking. And, there is no other experimental evidence to indicate a more definite value for $G_{(I,II)c}$.

Accordingly, the theoretical onset strains are calculated; and they are tabulated in Table 4.4. Again, the effect of the reduced 90°-layer property is negligible. Although, the predicted strains for $n \geq 2$ are uniformly smaller than that for mid-plane delamination, the 25/90 delamination may not govern when $n \geq 4$, because the increasing trend of the prediction with the increase of the 90°-layer thickness suggests that a different mode of failure may occur before this type of delamination, which is due to edge effects alone.

137

Figure 4.22 Mechanical Load Energy Release Rate Coefficients for 25/90 Interface Free-Edge Delamination.

138
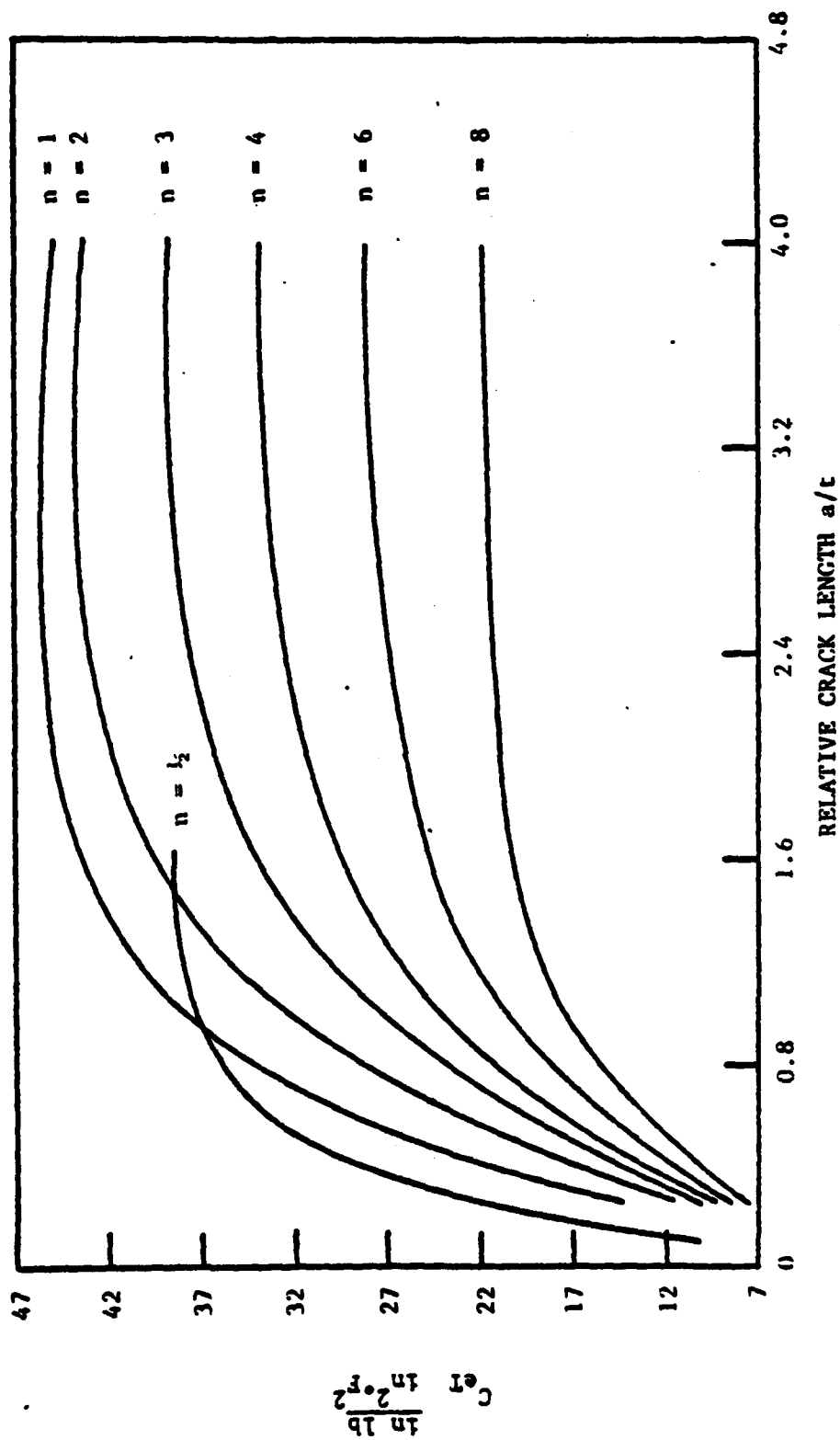
Figure 4.23 Coupled Thermal/Mechanical Energy Release Rate Coefficients for 25/90 Interface Free-Edge Delamination.

139
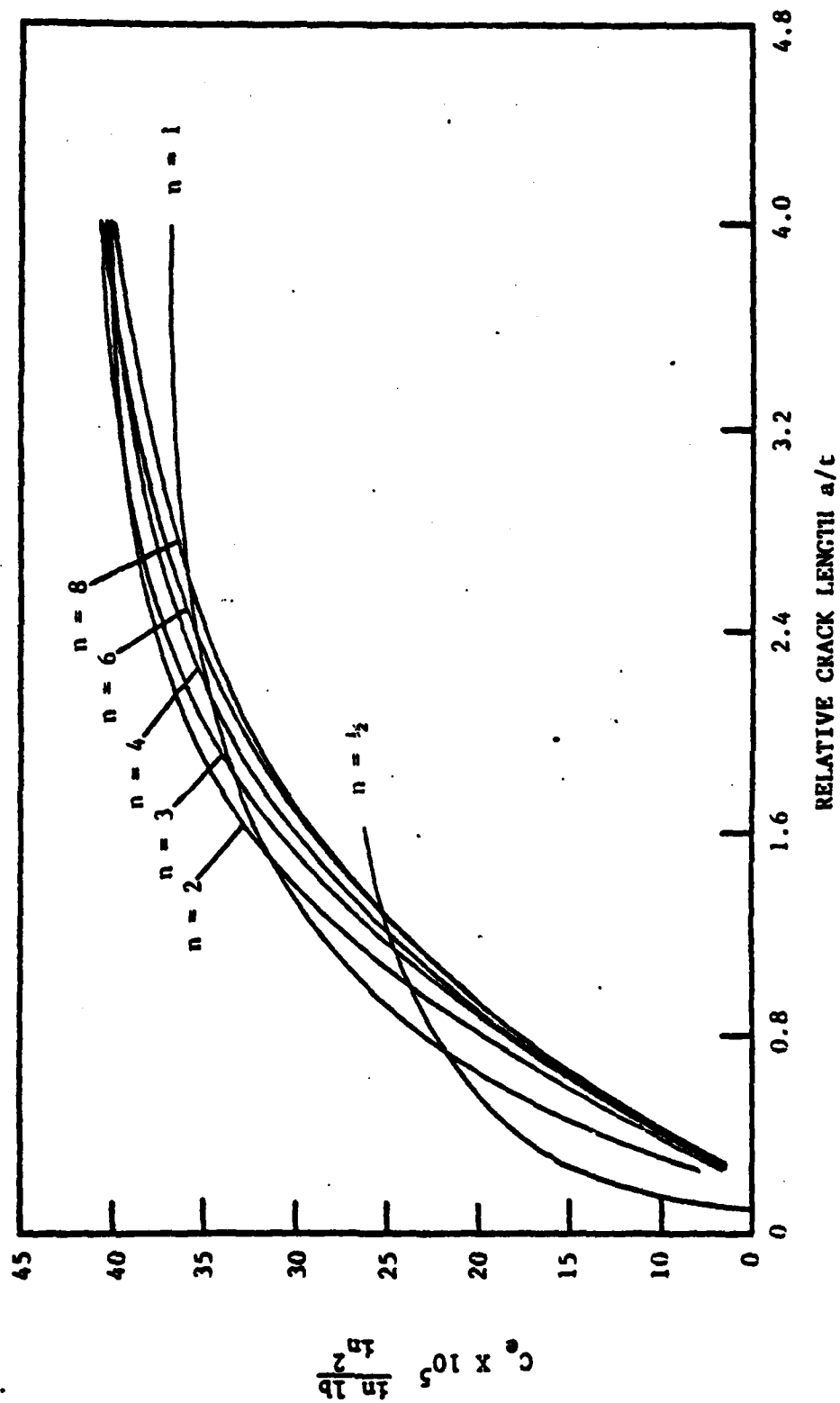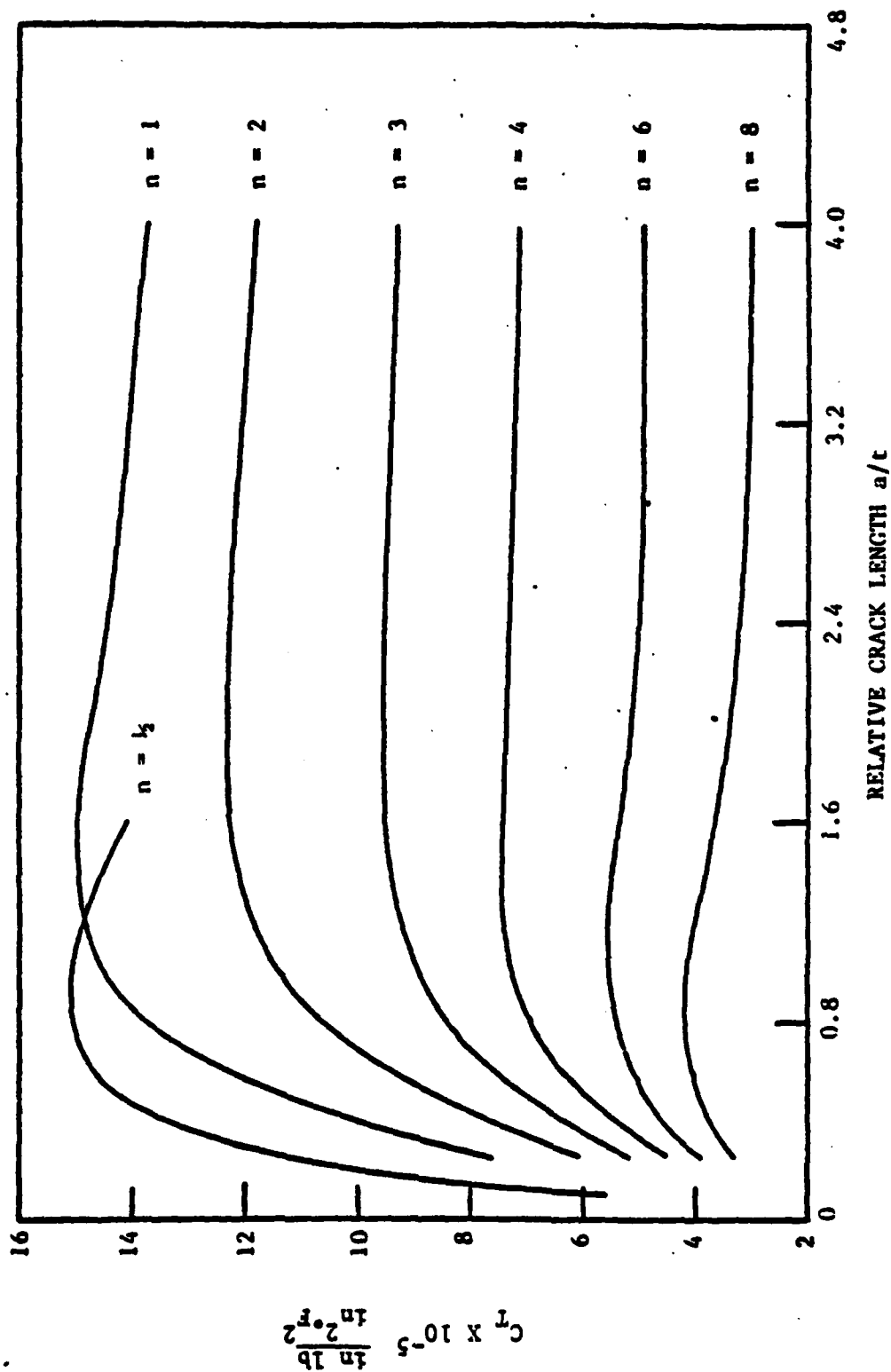
Figure 4.24   Thermal Load Energy Release Rate Coefficients for
25/90 Interface Free-Edge Delamination.

Figure 4.25 Mechanical Load Energy Release Rate Coefficients for 25/90 Interface Free-Edge Delamination with Reduced 90° Ply Properties.
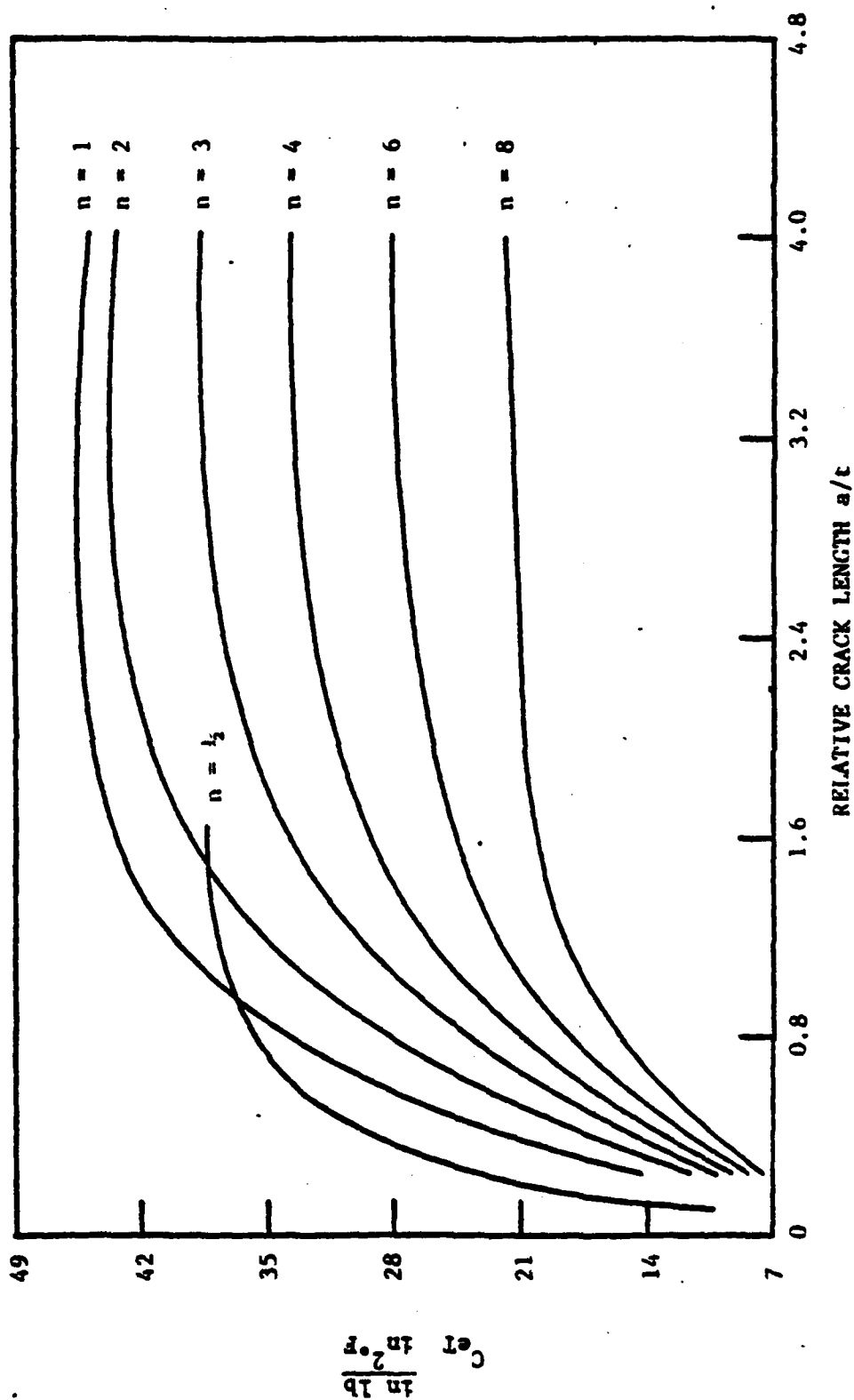
Figure 4.26 Coupled Thermal/Mechanical Energy Release Rate Coefficients Free-Edge Delamination with Reduced 90° Ply Properties.
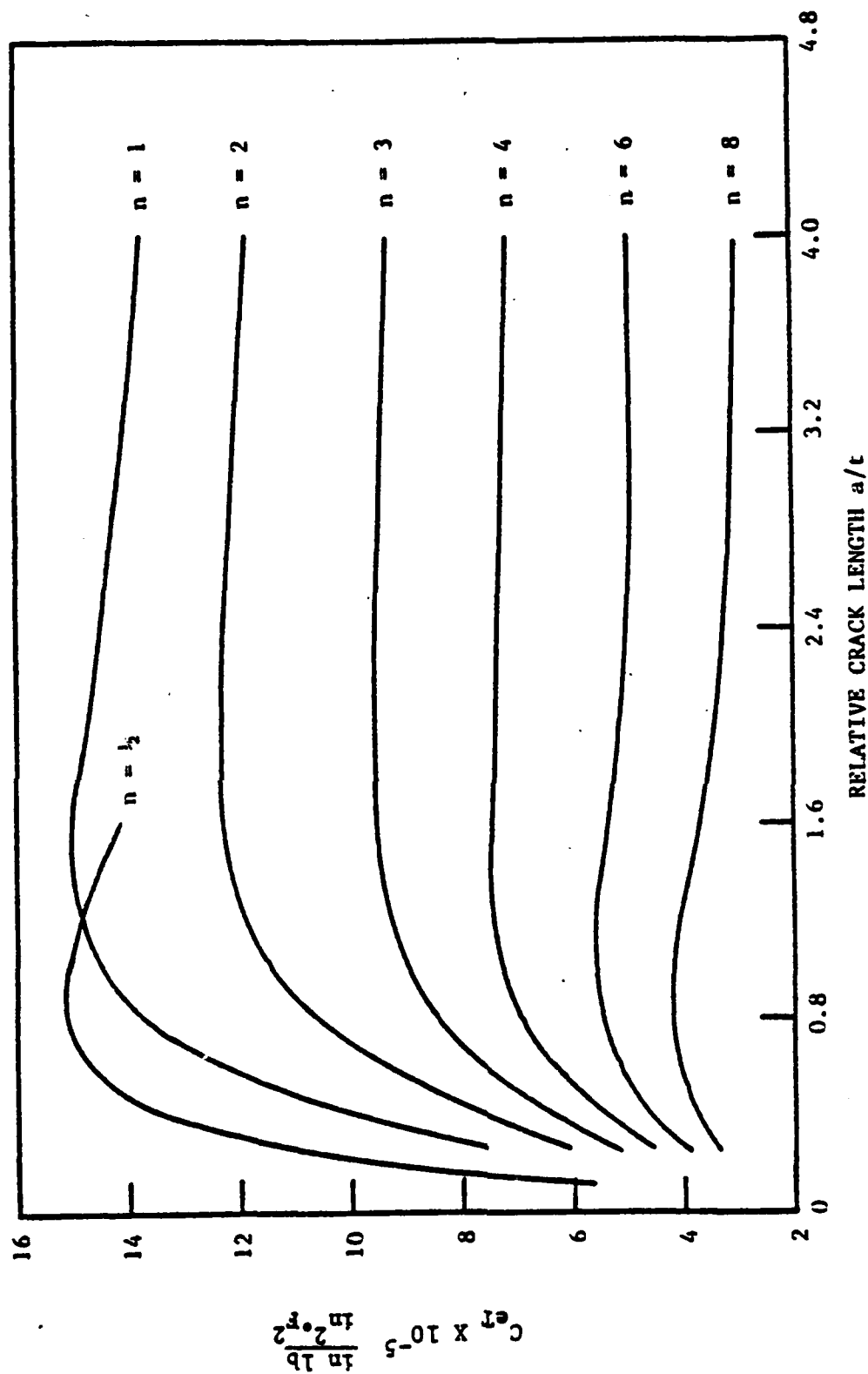
Figure 4.27 Thermal Load Energy Release Rate Coefficients for 25/90 Interface Free-Edge Delamination with Reduced 90° Ply Properties.
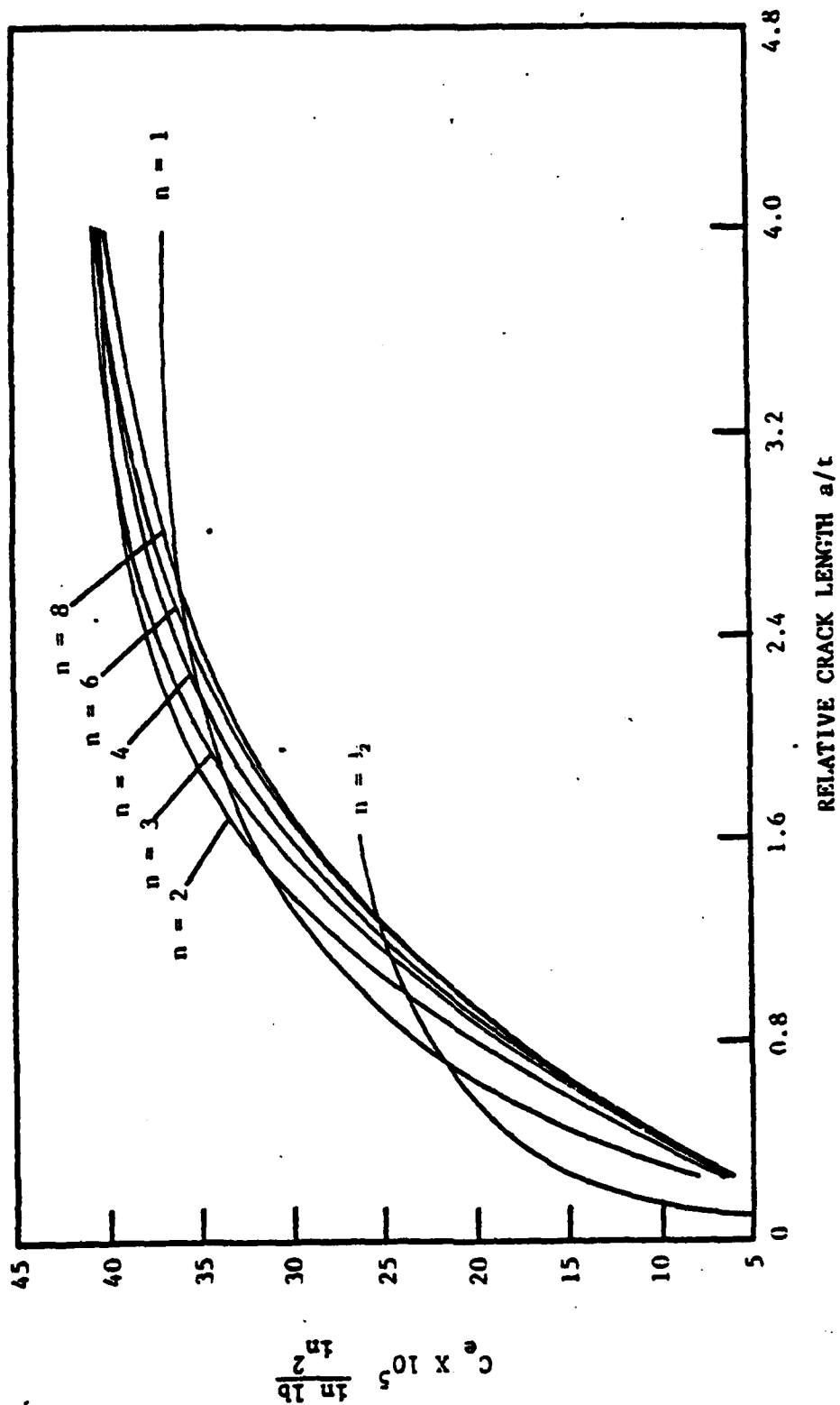
Table 4.4 Calculated Critical Strain and Energy Release Rates
for 25/90 Interface Free-Edge Delamination

n	$\frac{a_0}{t}$	NO TRANSVERSE CRACKING				WITH TRANSVERSE CRACKING			
		G_e $(\%G_c)$	G_T $(\%G_c)$	G_{eT} $(\%G_c)$	e_x (%)	G_e $(\%G_c)$	G_T $(\%G_c)$	G_{eT} $(\%G_c)$	e_x (%)
1	2	68.6	3.0	28.4	0.706	68.5	3.0	28.5	0.704
2	2	70.9	2.5	26.6	0.702	70.9	2.5	26.6	0.701
3	2	74.2	1.9	23.9	0.730	73.6	2.0	24.4	0.727
4	2	77.2	1.5	21.3	0.758	77.0	1.5	21.5	0.756
6	2	80.5	1.1	18.4	0.781	80.5	1.1	18.4	0.781
8	2	84.1	0.7	15.2	0.804	84.0	0.7	15.3	0.804

144

Mixed-Mode Delamination From a Transverse Crack Tip

From the previous discussions, it is evident that formation of free edge delamination interacts with the formation of transverse cracking in the $[\pm 25/90_n]_s$ series. The relative dominance of one over the other depends closely on the parameter n. For n > 2, transverse cracks always form before delamination. And, the shear stress concentration at the transverse crack tip can aggravate delamination along the 25/90 interface where the transverse crack is terminated. Fig. 4.28 shows the interlaminar shear stresses τ_{yz} as plotted against the distance from a transverse crack tip along the 25/90 interface. It is seen that the singular stress magnitude near the crack tip is essentially the same for all values of n. However, the shear stress gradient away from the crack tip becomes gradual as the value of n increases. Thus, in terms of the available strain energy for delamination along the interface, the larger the value of n, the more available strain energy. Clearly, for a large n (or thicker 90°-layer), the likelihood of a transverse crack tip induced delamination becomes predominant.

Fig. 4.29 illustrates the schematical representation of the transverse crack tip induced delamination. Without considering other interacting factors, such a delamination growth can be modeled as a 1-dimensional crack propagation in the load direction along the 25/90 interface. Accordingly, the finite element simulation, in this case, is shown in Fig. 4.30. The applied load is represented by a uniform displacement δ of the ± 25-layer, such that the far-field axial laminate strain is a unity. Delamination growth is denoted by the crack size a.
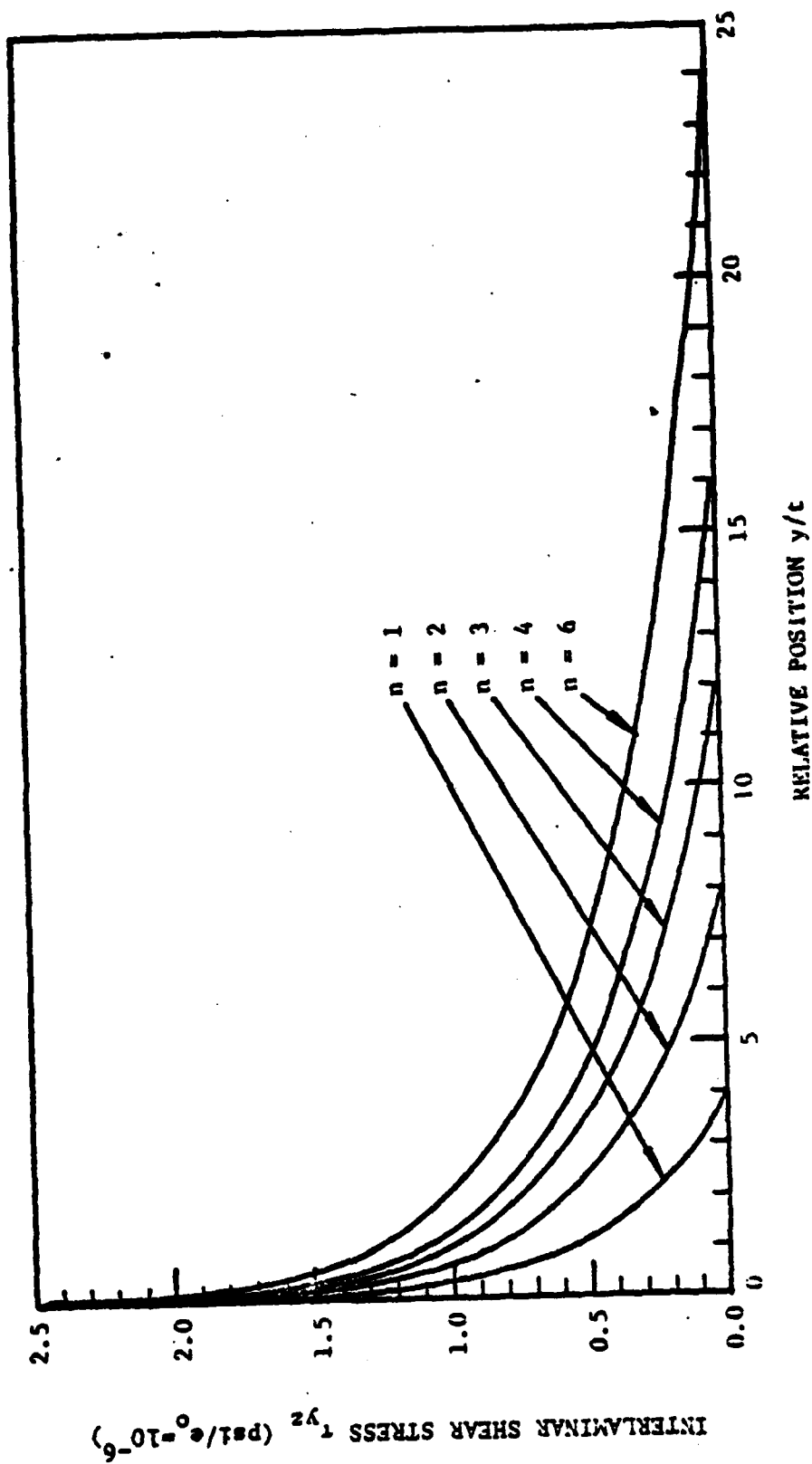
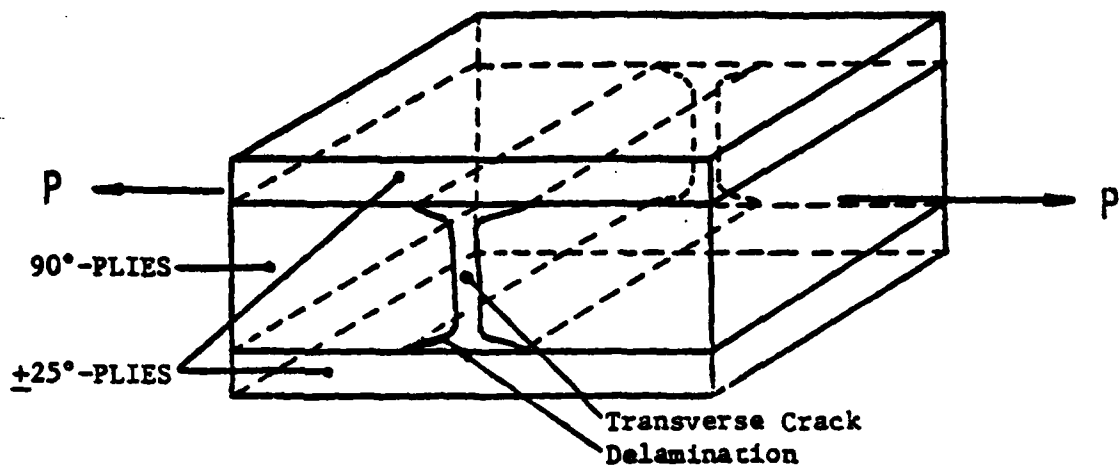Figure 4.28 Interlaminar Shear Stress vs. Relative Distance from a Transverse Crack Tip.

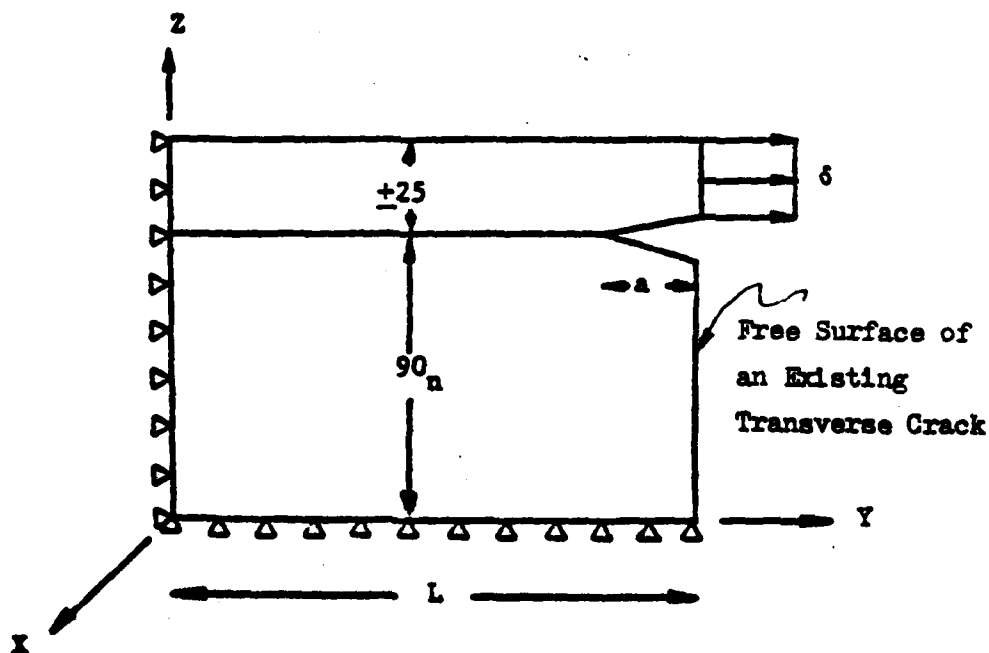Figure 4.29 Schematic of Transverse Crack Tip Delamination

Figure 4.30 Finite Element Model for Transverse Crack Tip Delamination.

147

Numerical calculations for the energy release rate coefficients are conducted for the laminates of n = 3,4,6 and 8. And, these are shown in Fig. 4.31. These calculated coefficients represent the total sum of the mode I and II components; the mode-III component is negligible for all values of n.

It is noted that for this type of delamination, the mode-II shearing action is predominant. Initially, when the crack is small, the crack-tip "opening" is actually closed. As the crack becomes large (greater than t), then, the mating surfaces of the crack become separated with some "opening". The emergence of the "opening" mode for each value of n is indicated by the transition of the dashed lines to solid lines in Fig. 4.31.

Let us now examine again the schematic representation in Fig. 4.29. Along the free edge of the $[\pm 25/90_n]_s$ laminate, there is still the competing delamination action due to the edge interlaminar stresses on the 25/90 interface. The available strain energy for this edge crack action has been evaluated earlier for the 25/90 mixed-mode delamination cases, and the corresponding energy release rate coefficients are displayed in Figs. 4.25, 4.26 and 4.27.

The driving forces (energy release rate) for the above discussed crack are mutually orthogonal at the instant of initiation; the transverse crack tip delamination is in the load direction and the edge delamination perpendicular to the load direction. Thus, in the absence of a truly 3-dimensional crack growth simulation model, we simply assume that the two orthogonal energy release rates can be added as a vector sum, which is then the driving force for the triangular shaped delamination, as observed in the experiment for cases of $n \geq 4$.
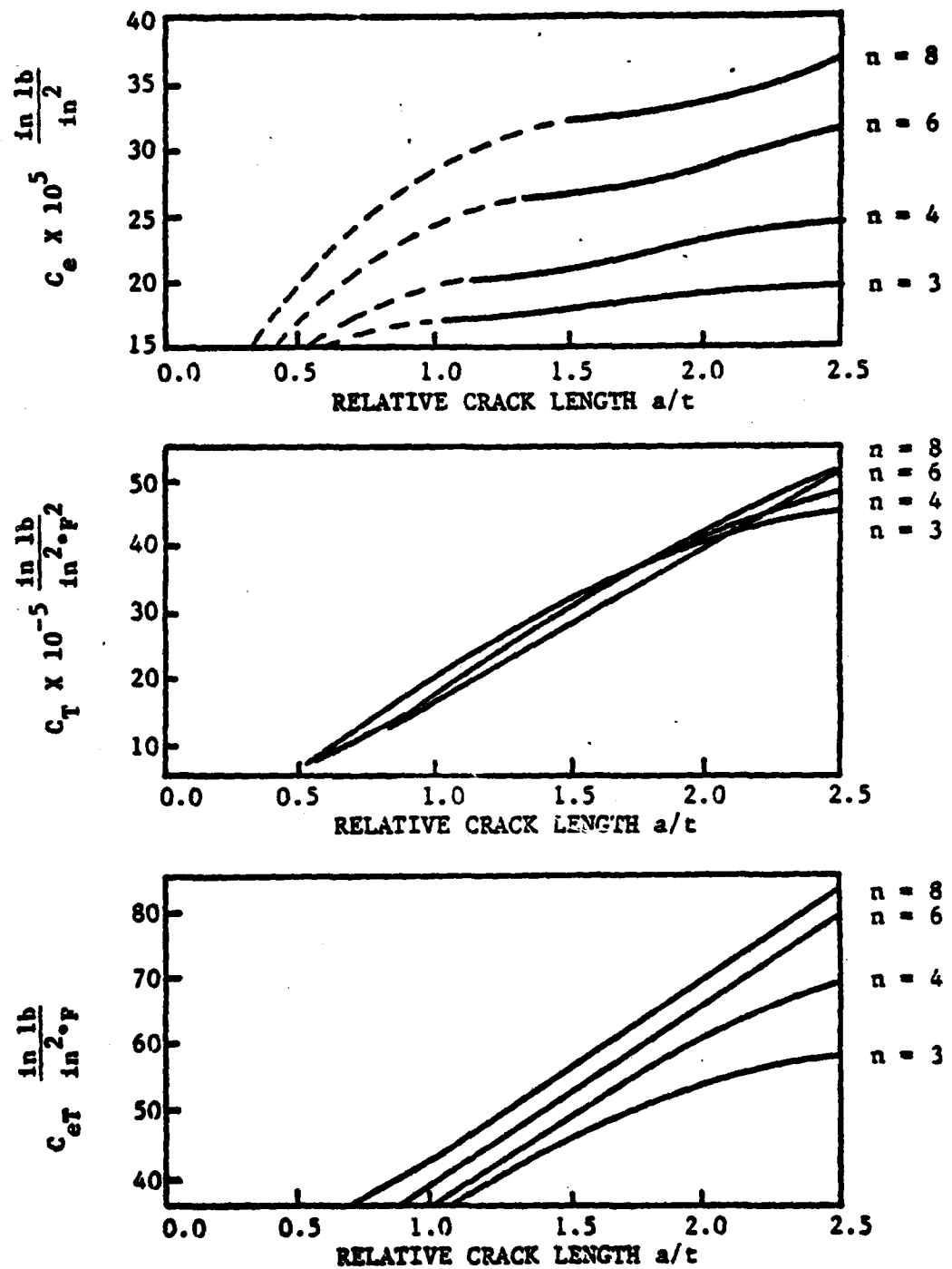
Figure 4.31   Mechanical, Thermal, and Coupled Energy Release
Rate Coefficients for Transverse Crack Tip
Delamination in the n = 3,4,6 and 8 Laminates.

Thus, the vector sum of the energy release rate is given by

$$G_{TOT} = \sqrt{G_{TC}^2 + G_{ED}^2} \qquad (4.29)$$

where G_{TC} is the energy release rate associated with delamination emanating from the transverse crack tip, and G_{ED} is the energy release rate associated with the mixed-mode 25/90 interface delamination at the free edge. The corresponding initiation criteria for such a delamination is then given by

$$G_{TOT}(a_0) \geq G_{(I,II)c} \qquad (4.30)$$

As in the previous cases of mixed mode cracking, we again use values for $G_{(I,II)c} = 1.5$ in-lb/in^2 and $a_0 = 2t$. A prediction for the onset of these cracks are then calculated. These calculated results are given in Table 4.5 below.

Table 4.5 Calculated Critical Strain for Combined Transverse Crack Tip Delamination and 25/90 Interface Free-Edge Delamination

n	3	4	6	8
$\bar{e}_x$ (%)	0.611	0.596	0.573	0.555

Figure 4.32 summarizes the predicted onset strains of edge delamination for the series of laminates, along with the experimentally obtained values. The different symbols used in the figure distinguish the various delamination
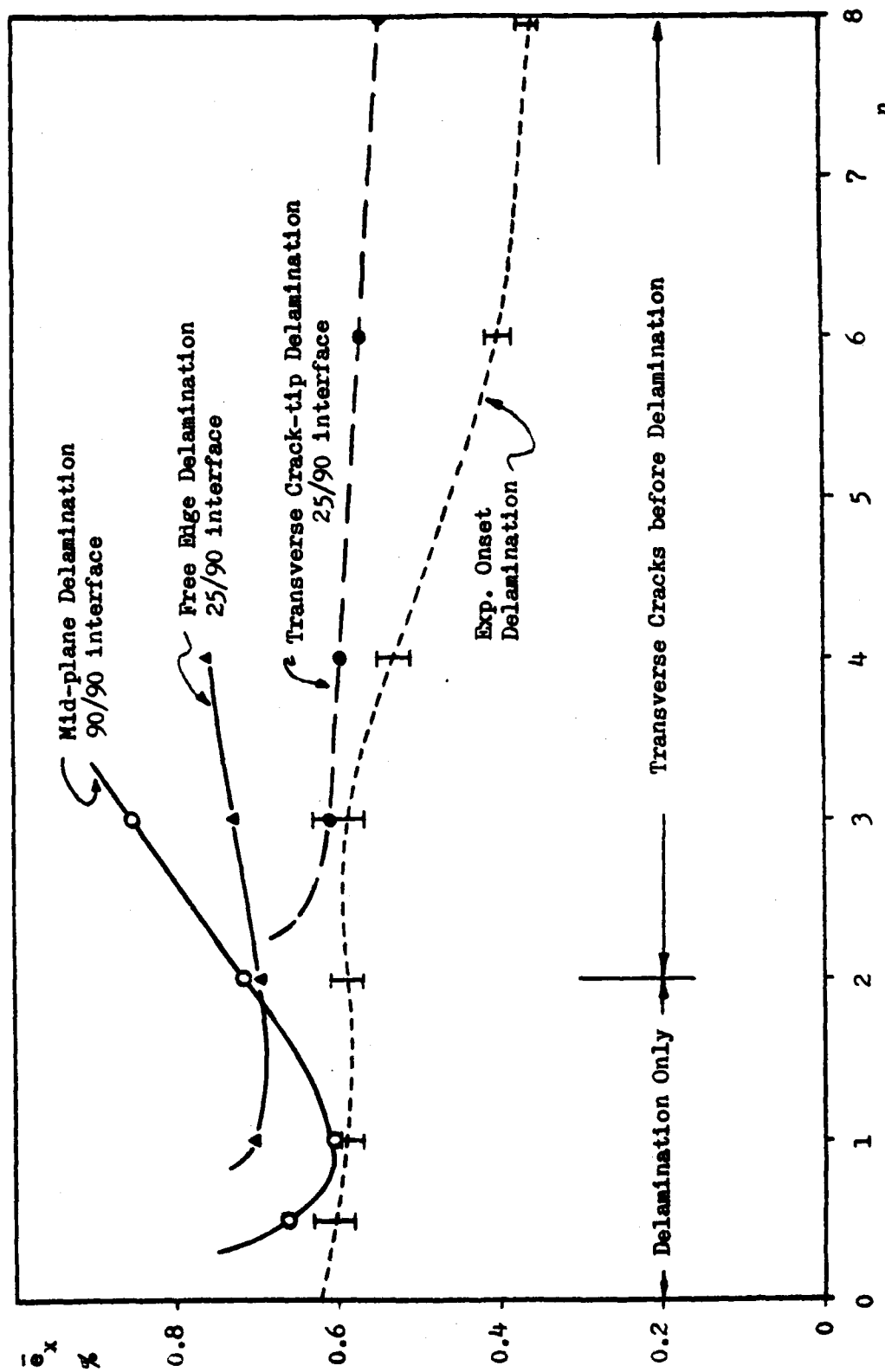
Figure 4.32 Comparison of Calculated Results with Experiment, $[\pm 25/90_n]$ Series

modes. It seems that the analysis captures the physical mechanisms quite accurately, although the quantitative prediction showed some discrepancy with the experiment, especially for n > 4. In the latter case, it is believed that the reason for the low laminate strain at onset of delamination is due to the excess strain energy released during the unstable propagation of the transverse cracks (see Fig. 2.8 and the associated discussion in Section II). This excess energy in laminates of n = 6 and 8 is very large; the associated dynamic effect is believed to cause the prematured delamination growth, which is emanating from the transverse crack tip. Indeed, if we examine the experimental data shown in Fig. 3.11, we see for example that in the laminate of n = 8, delamination along the 25/90 interface followed immediately the formation of transverse cracking, while the final laminate failure followed immediately the delamination. It seems that the sequence of events from transverse cracking to final failure is almost continuous whenever the 90°-layer is excessively thick.

4.6 Mixed-Mode Fracture in $[\theta_8]$-Family .

In this sub-section, we shall present some of the numerical details in simulating the crack growth emanating from the notch-tip, along the fiber direction for the $[\theta_8]$ family. In this case, the same finite element procedures were followed, except that the basic formulation of the finite element stiffness matrix was based on a "plane stress" approach, rather than the "generalized plane strain" approach. Thus, the mode of cracking generally consists of mode I and mode II only. The ratio between G_{II} and G_I depends on the fiber angle θ.

Fig. 4.33 shows the calculated energy release rates G_I and G_{II} as plotted against the crack growth size a (see Fig. 3.21 for the crack growth geometry). The unit of G shown in the figure is in-lb/in^2 per unit far-field applied strain.

From Fig. 4.33, it is seen that mode I action is predominant for fiber angle $\theta > 45°$; and the mode-II component of G is practically negligible. G-curves for $\theta > 45°$ are monotonically increasing with the crack size a, suggesting an unstable crack growth behavior. As the fiber angle decreases from 45°, mode-II contribution increases rapidly. In particular, when $\theta < 30°$ the energy release rate curves show a decrease as the crack grows from the notch tip. As the crack grows further, the available energy then increases slightly. Thus, a minimum value of G exists for 0.01" < a < 0.04". This behavior of the energy release rate indicates a stable crack growth for small fiber angles, say $\theta < 20°$.

Assuming that a macroscopic flaw of size about 0.01" exists near the notch tip along the fiber direction (this is the same as $a_0 \sim 2t$ as before), then, the values of G_I and G_{II} taken at a = a_0 will determine the onset of crack growth along the θ-direction. These values of G_I and G_{II} were shown earlier in Fig. 3.20; and they were used to correlate with the experimental data (Fig. 3.19). In the process, we determined the material resistance $G_{(I,II)c}$ under the varying degree of mixed-mode crack actions. As is shown in Fig. 3.22, $G_{(I,II)c}$ shows a dependence on the ratio G_{II}/G_I when it is measured at the macroscopic level.
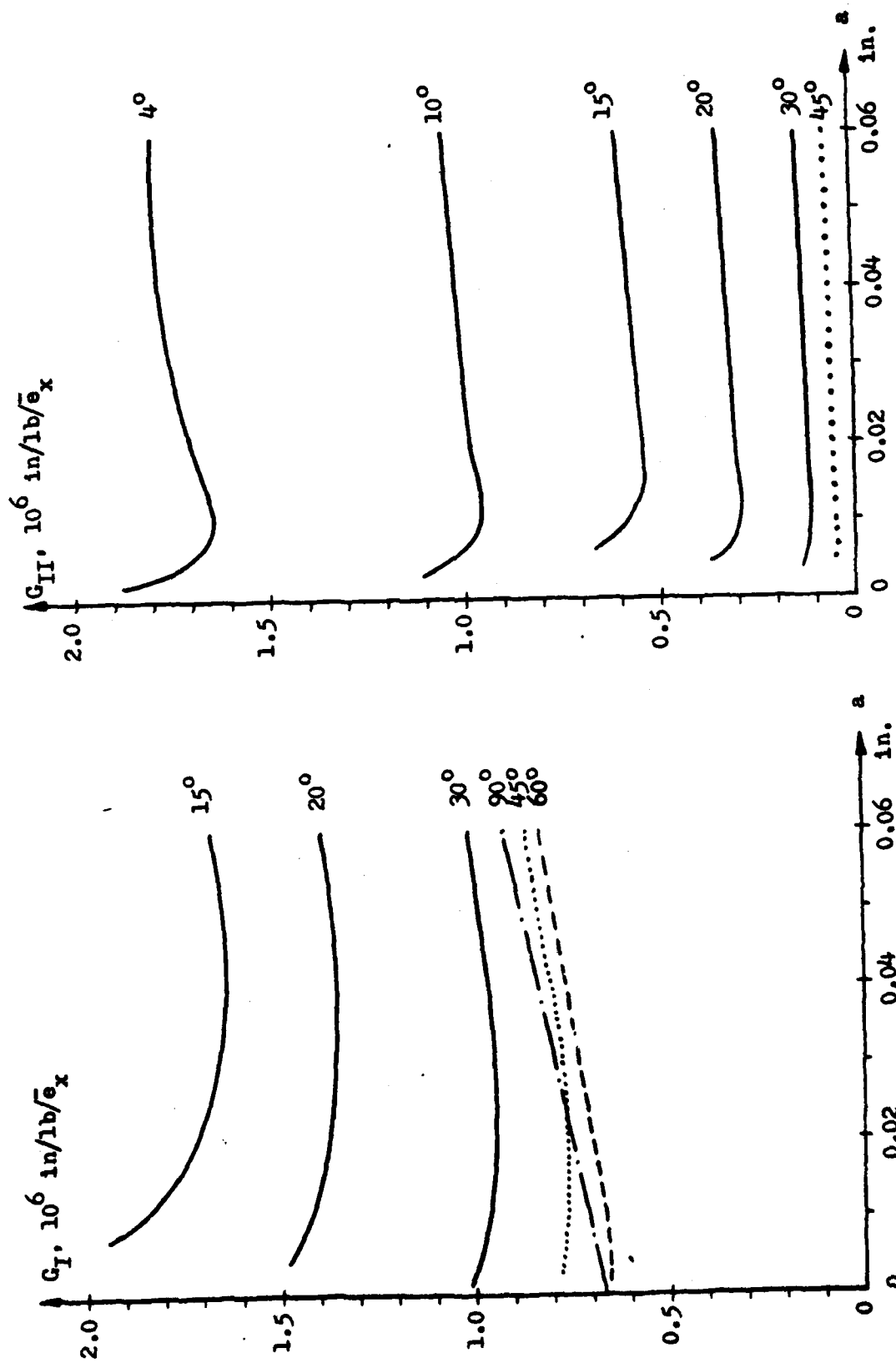
153

Figure 4.33 G_I and G_{II} Components of Double Side-Notched – $[\Theta_8]$-Family

154

V. CONCLUDING REMARKS

In this report, we have presented the research results obtained in the AFOSR sponsored program under the contract F49620-79-C-0206.

Before this report, a total of six (6) technical papers and a Ph.D. dissertation were published during the contract period from 1 September 1979 to 30, September 1981. These papers have dealt individually some of the major developments accomplished in this program, see Ref. [29-35].

At the conclusion of this report, the following observations are made. (a) Sub-laminate crack growth, such as transverse cracks and edge delamination discussed in this report, is basically a fracture failure process. It has been demonstrated that the phenomenological description, via ply elasticity and the classical fracture mechanics, can be applied successfully to model some of the often observed cracking processes.

But, it must be pointed out that, given a laminate under load, there may be a multitude of crack modes that interact with one another. The resulting complex network of crack propagation may present a formidable mathematical problem if it is also to be described by the same fracture analysis approach.

Rather, we have learned from the simpler analysis the important material and geometrical parameters which have profound influences on the sub-laminate crack growth behavior. For example, the effect of the 90°-layer thickness on the transverse cracking and delamination processes deserves due attention in practical design. Similarly, the material toughness G_c is another parameter which should be considered in composite laminate design.

(b) Sub-laminate crack growth generally lowers the strength of the laminate. The effect pertains to the growth stability of the sub-laminate cracks. In the $[\pm 25/90_n]_s$ series studied in this report, see Fig. 3.11, it is seen that the failure strain of the load-bearing ply (the $\pm 25°$-layer) decreases dramatically when $n \geq 4$. The in-situ stresses in the $\pm 25°$-plies just before failure varies profoundly with the value of $\dot{n}$, as shown in Fig. 5.1. Clearly, the failure process in the load-carrying $\pm 25°$-plies is again a fracture event. This, however, has not been analyzed in this report.

(c) The finite-element/crack-closure procedure is a useful computational simulation technique. In view of the dimensional requirement of the phenomeno-logical model, it is felt that a simple formulation (without inclusion of stress singularity, for instance) is sufficient for purpose of simulating the kinds of crack propagation such as discussed in this report.

(d) It is felt that the determination of G_c associated with sub-laminate cracks has been inadequate. In particular, the process of mixed-mode failure remains almost unexplored. Continued and future researches may provide more information soon.
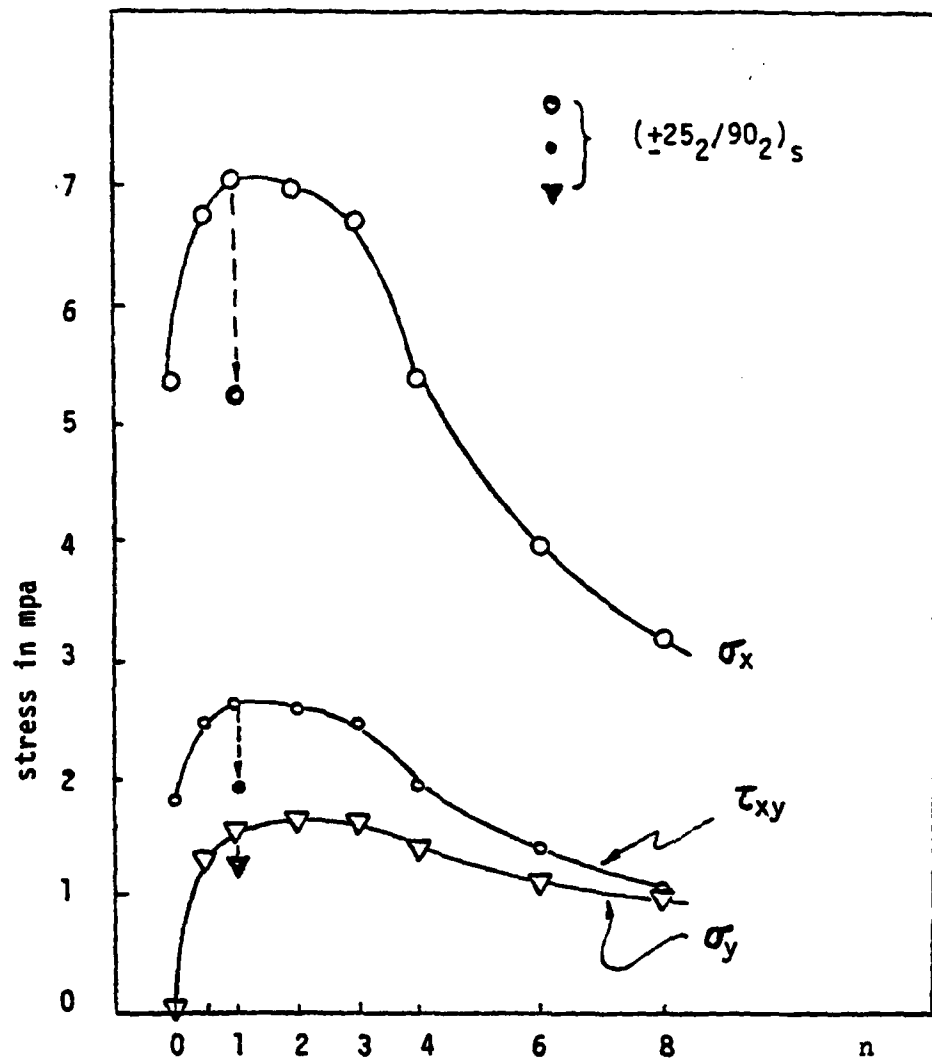
Figure 5.1 In-situ stresses in the 25°-plies at Laminate
Failure of the $[\pm 25/90_n]_s$ and $[\pm 25_2/90_2]_s$
Laminates vs. the number of 90-plies, n.

REFERENCES

[1] G. P. Cherepanov, "Mechanics of Brittle Fracture," McGraw-Hill Co. New York (1979), p. 8.

[2] M. B. Bader, J. E. Bailey, P. T. Curtis and A. Parvizi, "The Mechanisms of Initiation and Development of Damage in Multi Axial Fiber - Reinforced Plastics Laminates," Mechanical Behavior of Materials, ICM-3, Vol. 3 (1979), pp. 227-239.

[3] R. B. Pipes and N. J. Pagano, "Interlaminar Stresses in Composite Laminates under Uniform Axial Tension," J. Comp. Materials, Vol. 4, (1970), p. 538.

[4] S. Tang, "Interlaminar Stresses of Uniformly Loaded Rectangular Composite Plates," J. Comp. Materials, Vol. 10 (1976), p. 69.

[5] P. W. Hsu and C. T. Herakovich, "A Perturbation Solution for Interlaminar Stresses in Composite Laminates," Composite Materials: Test and Design, ASTM STP 617 (1977), p. 296.

[6] A.S.D. Wang and F. W. Crossman, "Some New Results on Edge Effect in Symmetric Composite Laminates," J. Comp. Materials, Vol. 11 (1977), p. 92.

[7] S. S. Wang and I. Choi, "Boundary-Layer Effects in Composite Laminates," paper #F9-0803. AIAA/ASME/ASCE/AHS 20th Structures, Structural Dynamics and Materials Conference, St. Louis (1979).

[8] N. J. Salamon, "An Assessment of the Interlaminar Stress Problem in Laminated Composites," J. Comp. Materials, Supplement, Vol. 14 (1980), p. 177.

[9] J. G. Bjeletich, F. W. Crossman and W. J. Warren, "The Influence of Stacking Sequence on Failure Modes in Quasi-Isotropic Graphite-Epoxy Laminates," Failure Modes in Composites - IV, AIME, (1978).

[10] B. T. Rodini, Jr. and J. R. Eisenmann, "An Analytical and Experimental Investigation of Edge Delamination in Composite Laminates," Proc. 4th Conf. Fibrous Composites, San Diego, Calif., (Nov. 1978).

[11] J. S. Cullen, "Mode-I Delamination of Unidirectional Graphite-Epoxy Composite under Complex Load Histories," M.S. Thesis, Texas A & M University, (1981).

[12] D. Williams, "Mode-I Transverse Cracking in an Epoxy and a Graphite Fiber Reinforced Epoxy," M.S. Thesis, Texas A & M University (1981).

[13] P. S. Vanderkley, "Mode I and Mode II Delamination Fracture Toughness of a Unidirectional Graphite-Epoxy Composite," M.S. Thesis, Texas A & M University (1981).

[14] A. A. Griffith, "The Phenomena of Rupture and Flow in Solids," Phil. Trans. Roy. Soc. Vol. A221 (1920), p. 163.

[15] G. R. Irwin, "Fracture Dynamics," in "Fracture of Metals" ASM, Cleveland (1948), p. 147.

[16] E. O. Orowan, "Fundamentals of Brittle Behavior of Metals," in "Fatigue and Fracture of Metals," W. M. Murray, Ed. Wiley, N.Y. (1950), p. 139.

[17] N. I. Murkhelishvili, "Some Basic Problems from the Mathematical Theory of Elasticity," Noordhoff, Holland (1953).

[18] I. N. Sneddon, "Integral Transform Methods," in Methods of Analysis and Solutions of Crack Problems, Noordhoff, Holland (1973), p. 315.

[19] S. G. Lekhnitsky, "Theory of Elasticity of an Anisotropic Elastic Body," Holden-Day, San Francisco (1963).

[20] G. R. Irwin, "Fracture," Handbuch der Physik, Vol. V, Springer-Verlag, (1958), p. 551.

[21] J. R. Rice, "A Path Independent Integral and Approximate Analysis of Strain Concentration by Notches and Cracks," J. Appl. Mech. Trans. ASME, (June 1968), pp. 379-386.

[22] R. J. Bucci, P. C. Paris, J. D. Landis and J. R. Rice, "J-Integral Estimation Procedures," Fracture Toughness, ASTM STP 514, ASTM, (1972), pp. 40-69.

[23] E. F. Rybicki and M. F. Kanninen, "A Finite Element Calculation of Stress Intensity Factors by a Modified Crack Closure Integral," Eng. Fract. Mech., Vol. 9, (1977), pp. 931-938.

[24] K. L. Reifsnider and J. E. Masters, "Investigation of Characteristic Damage States in Composite Laminates," ASME paper No. 78-WA/AERO-4 (1978).

[25] J. Aveston and A. Kelly, "Theory of Multiple Fracture of Fibrous Composites," J. Matl. Science, Vol. 8 (1973), p. 352.

[26] A. S. D. Wang and G. E. Law, "Interlaminar Failure in Epoxy-Based
      Composite Laminates," <u>Proc. 29th Symp. Failure Modes in Composites</u>,
      National Bureau of Standards, (1979).

[27] S. W. Tsai, "Mechanics of Composite Materials," I and II,
      AFML-TR-66-14, Air Force Materials Laboratory (1966).

[28] D. J. Wilkins, "A Comparison of the Delamination and Environmental
      Resistance of a Graphite-Epoxy and a Graphite-Bismaleimide"
      NAV-GD-0037, <u>Naval Air System Command</u> (1981).

The following papers were written during the course of the research, each of
which dealt with some of the individual aspects reported in this volume.

[29] A. S. D. Wang, G. E. Law, Jr. and W. J. Warren, "An Energy Method for
      Multiple Transverse Cracks in Graphite-Epoxy Laminates," in <u>Modern
      Developments in Composite Materials and Structures.</u> Ed. J. R. Vinson
      (1979), p. 17.

[30] A. S. D. Wang and F. W. Crossman, "Initiation and Growth of Transverse
      Cracks and Edge Delamination in Composite Laminates. Part 1, An Energy
      Method," <u>J. Comp. Materials</u>, Vol. 14, (1980), p. 71.

[31] F. W. Crossman, W. J. Warren, A.S.D. Wang and G. E. Law, Jr.,
      "Initiation and Growth of Transverse Cracks and Edge Delamination in
      Composite Laminates. Part 2. Experimental Correlation," <u>J. Comp.
      Materials</u>, Vol. 14 (1980), p. 87.

[32] A. S. D. Wang, "Growth Mechanisms of Transverse Cracks and Ply
      Delamination in Composite Laminates," in <u>Advances in Composite Materials</u>,
      Proc. ICCM-III (1980), p. 170.

[33] F. W. Crossman and A. S. D. Wang, "The Dependence of Transverse Cracks
      and Delamination on Ply Thickness in Graphite-Epoxy Laminates" in
      <u>Damage in Composite Materials: Basic Mechanisms</u>, <u>Accumulation, Tolerance
      and Characterization,</u>" ASTM STP (in press).

[34] A. S. D. Wang, N. N. Kishore and W. W. Feng, "On Mixed-Mode Fracture
      in Off-Axis Unidirectional Graphite-Epoxy Composites," <u>Proc. ICCM-IV</u>
      (1982), (in press).

[35] G. E. Law, Jr., "Fracture Analysis of $[\pm 25/90_n]_s$ Graphite-Epoxy
      <u>Composite Laminates,</u>" Ph.D. Dissertation, Drexel University (1981).